

Summer 7-13-2012

## H2O Maser Observations in W3 (OH): A comparison of Two Epochs

Steven Merriman  
DePaul University, smerriman1220@gmail.com

Follow this and additional works at: [https://via.library.depaul.edu/csh\\_etd](https://via.library.depaul.edu/csh_etd)

 Part of the [Physics Commons](#)

---

### Recommended Citation

Merriman, Steven, "H2O Maser Observations in W3 (OH): A comparison of Two Epochs" (2012). *College of Science and Health Theses and Dissertations*. 31.  
[https://via.library.depaul.edu/csh\\_etd/31](https://via.library.depaul.edu/csh_etd/31)

This Thesis is brought to you for free and open access by the College of Science and Health at Via Sapientiae. It has been accepted for inclusion in College of Science and Health Theses and Dissertations by an authorized administrator of Via Sapientiae. For more information, please contact [digitalservices@depaul.edu](mailto:digitalservices@depaul.edu).



DEPAUL UNIVERSITY

# $\text{H}_2\text{O}$ Maser Observations in $\text{W3(OH)}$ : A Comparison of Two Epochs

by

Steven Merriman

A thesis submitted in partial fulfillment for the  
degree of Master of Science

in the

Department of Physics  
College of Science and Health

July 2012

# Declaration of Authorship

I, Steven Merriman, declare that this thesis titled, 'H<sub>2</sub>O Maser Observations in W3OH: A Comparison of Two Epochs' and the work presented in it are my own.

I confirm that:

- This work was done wholly while in candidature for a masters degree at Depaul University.
- Where I have consulted the published work of others, this is always clearly attributed.
- Where I have quoted from the work of others, the source is always given. With the exception of such quotations, this thesis is entirely my own work.
- I have acknowledged all main sources of help.
- Where the thesis is based on work done by myself jointly with others, I have made clear exactly what was done by others and what I have contributed myself.

Signed:

---

Date:

---

*“Radio astronomy has profoundly changed and enlarged our understanding of our Universe, enabling new discoveries, opening new celestial windows, revealing an otherwise invisible Universe.”*

NRAO Website

DEPAUL UNIVERSITY

# *Abstract*

Department of Physics  
College of Science and Health

Master of Science

by Steven Merriman

We present high resolution observations of 22 GHz H<sub>2</sub>O masers toward the star forming region W3(OH), taken during two epochs using the Very Long Baseline Array telescope. We detected a total of 54 masers in observation BS198A, and 67 in BS198B, arranged in 3 groups. We determined that the observation BS198A took place during a period of quiescence, while BS198B was observed during a flaring period. We interpreted the maser morphology as lying on the eastern (Group 1) and western (Group 3) ends of an outflow, as well as near the outflow base (Group 2). We observed a velocity drift between the two epochs, which we interpreted as an acceleration of the outflow. We observed the Zeeman effect, and detected significant  $B_{los}$  in 15 masers. We measured an increase in the  $B_{los}$  of the most intense maser from  $-28.85$  mG in the first epoch to  $-43.49$  mG in the second epoch. Using accepted values for the density of the preshock region measured using OH thermal absorption lines, we calculated the density of the postshock region and found it to be in agreement with the theoretical values required for H<sub>2</sub>O masing. We also observed the magnetic energy density to be on the order of or up to two orders of magnitude larger than the kinetic energy density, depending on the assumed velocity dispersion. This indicates that the magnetic field is dynamically significant in the W3(OH) region.

# *Acknowledgements*

I would like to begin by thanking Dr. Anuj Sarma. As my advisor Dr. Sarma has shown an endless amount of support and patience in the process of working on this thesis. His works are referenced multiple times throughout this thesis, and without his guidance this work would not have been possible. I would also like to thank Dr. Emmanuel Momjian, my summer research advisor at NRAO where this project began. The word “we” throughout this thesis should be interpreted “I, under the watchful guidance of Dr. Sarma and Dr. Momjian”. I would also like to thank the members of my committee, Dr. Pando and Dr. Landahl, for giving so generously of their time in reviewing my work. I am grateful for Josh Modica, who as part of a summer project wrote the MATLAB code to determine the curve fit parameters of equation (2.26), as well as the program to plot the scaled derivative of the Stokes I profiles; and Wale Afolayan, who generously did the gaussian fitting of the Stokes I profiles of the detected masers. Both of these students are very talented, and have promising futures in the sciences. For putting up with a graduate student working on a thesis, I would like to thank my family and friends. This especially goes for my girlfriend, Melinda Baggett, who gave to me an endless amount of support, and without whom I would not leave this process with my sanity.

I would also like to thank the faculty of the Depaul Physics Department, my professors for the knowledge they have instilled in me, and the National Radio Astronomy Observatories for providing the resources necessary to making this work possible ...

# Contents

Declaration of Authorship	i
Abstract	iii
Acknowledgements	iv
List of Figures	vii
List of Tables	ix
Abbreviations	x
Physical Constants	xi
Symbols	xii
<b>1 Introduction</b>	<b>1</b>
1.1 High Mass Star Formation and Magnetic Fields	2
1.1.1 Observational Signatures of Star Formation	3
1.2 Masers	3
1.3 H <sub>2</sub> O Masers and the H <sub>2</sub> O Molecule	5
1.4 The Zeeman Effect	9
1.5 The Zeeman Effect and the H <sub>2</sub> O Molecule	12
1.5.1 Hyperfine-Structure	12
1.5.2 Zeeman Splitting of the 6 <sub>16</sub> → 5 <sub>23</sub> Transition	14
<b>2 Observations and Data Reduction</b>	<b>17</b>
2.1 Radio Interferometry	17
2.1.1 Interferometry in Astronomy	17
2.1.2 The VLBA Telescope	18
2.1.3 How do Interferometers Work?	19
2.2 Observational Parameters	25
2.3 Data Calibration	25

2.3.1	Calibration Assumptions . . . . .	25
2.3.2	Calibration Procedure . . . . .	26
2.3.3	Self-Calibration . . . . .	29
2.4	Data Imaging . . . . .	29
2.5	Measuring the Magnetic Field via the Zeeman Effect . . . . .	34
<b>3</b>	<b>Results</b>	<b>36</b>
3.1	Maser Distribution and Parameters . . . . .	36
3.1.1	BS198A . . . . .	36
3.1.2	BS198B . . . . .	39
3.2	Magnetic Field Values . . . . .	47
<b>4</b>	<b>Discussion</b>	<b>52</b>
4.1	W3(OH) and the Turner-Welch Object . . . . .	52
4.2	Flaring Event . . . . .	54
4.3	H <sub>2</sub> O Maser Distribution in the TW Object . . . . .	54
4.4	Magnetic Fields . . . . .	58
4.4.1	Preshock and Postshock Magnetic Fields . . . . .	58
4.4.2	Energy Considerations . . . . .	60
4.4.3	Magnetic Field Comparison . . . . .	61
<b>5</b>	<b>Conclusions</b>	<b>62</b>
<b>A</b>	<b>Gaussian Fits of Stokes I Maser Spectra from BS198A</b>	<b>65</b>
<b>B</b>	<b>Gaussian Fits of Stokes I Maser Spectra from BS198B</b>	<b>75</b>
<b>C</b>	<b>Systemic Velocity of an Astronomical Source</b>	<b>87</b>
<b>D</b>	<b>BS198A IVD Plots</b>	<b>92</b>
<b>E</b>	<b>BS198B IVD Plots</b>	<b>95</b>
	<b>Bibliography</b>	<b>107</b>

# List of Figures

1.1	Stimulated Emission . . . . .	5
1.2	Bipolar Outflows and Methanol Masers . . . . .	6
1.3	Water Molecule . . . . .	7
1.4	H <sub>2</sub> O energy level diagram . . . . .	8
1.5	Energy Level Splitting in an external magnetic field . . . . .	10
1.6	Zeeman Splitting . . . . .	11
1.7	HS Diagram for H <sub>2</sub> O . . . . .	13
1.8	Hyperfine structure relative transition intensities . . . . .	14
1.9	Diagram showing the 39 components of the F=6-7 transition of ortho-H <sub>2</sub> O due to the Zeeman effect. . . . .	16
2.1	VLBA Antennas . . . . .	18
2.2	Two element interferometer . . . . .	20
2.3	Correlator Interpretation . . . . .	22
2.4	(u,v,w) Coordinate System . . . . .	23
2.5	Image of the Dirty Beam . . . . .	31
2.6	Clean and Dirty Images of Field 2, Channel 182 . . . . .	32
3.1	Maser locations from observation BS198A . . . . .	40
3.2	Maser locations from observations BS198B . . . . .	44
3.3	Maser locations from observations BS198A and BS198B . . . . .	45
3.4	Plot showing maser locations from BS198A, BS198B, Hachisuka et al.(2006) and Weiler et al.(2009). . . . .	46
3.5	IVD Plot for Maser 1 of Observation BS198A . . . . .	49
3.6	IVD Plot for Maser 1 of Observation BS198B . . . . .	50
4.1	Location of W3(OH) in Milky Way Galaxy . . . . .	53
4.2	Continuum image of W3(OH) and Enlarged view of TW Object . . . . .	56
A.1	Gaussian plot of BS198A Maser 1 . . . . .	65
A.2	Gaussian plot of BS198A Masers 2-7 . . . . .	66
A.3	Gaussian plot of BS198A Masers 8-13 . . . . .	67
A.4	Gaussian plot of BS198A Masers 14-19 . . . . .	68
A.5	Gaussian plot of BS198A Masers 20-25 . . . . .	69
A.6	Gaussian plot of BS198A Masers 26-31 . . . . .	70
A.7	Gaussian plot of BS198A Masers 32-37 . . . . .	71
A.8	Gaussian plot of BS198A Masers 38-43 . . . . .	72

---

A.9	Gaussian plot of BS198A Masers 44-49	73
A.10	Gaussian plot of BS198A Masers 50-54	74
B.1	Gaussian plot of BS198B Maser 1	75
B.2	Gaussian plot of BS198B Masers 2-7	76
B.3	Gaussian plot of BS198B Masers 8-13	77
B.4	Gaussian plot of BS198B Masers 14-19	78
B.5	Gaussian plot of BS198B Masers 20-25	79
B.6	Gaussian plot of BS198B Masers 26-31	80
B.7	Gaussian plot of BS198B Masers 32-37	81
B.8	Gaussian plot of BS198B Masers 38-43	82
B.9	Gaussian plot of BS198B Masers 44-49	83
B.10	Gaussian plot of BS198B Masers 50-55	84
B.11	Gaussian plot of BS198B Masers 56-61	85
B.12	Gaussian plot of BS198B Masers 62-67	86
C.1	Rotational Velocities in a Differentially Rotating Galaxy	88
C.2	Geometric Relationship Among the Quantities Used in Differential Rotation Derivation	89
C.3	Geometric Location of W3(OH) Relative to the Sun and Galactic Center	90
D.1	IVD Plot for Maser 2 of Observation BS198A	93
D.2	IVD Plot for Maser 13 of Observation BS198A	94
E.1	IVD Plot for Maser 4 of Observation BS198B	96
E.2	IVD Plot for Maser 5 of Observation BS198B	97
E.3	IVD Plot for Maser 9 of Observation BS198B	98
E.4	IVD Plot for Maser 10 of Observation BS198B	99
E.5	IVD Plot for Maser 11 of Observation BS198B	100
E.6	IVD Plot for Maser 15 of Observation BS198B	101
E.7	IVD Plot for Maser 25 of Observation BS198B	102
E.8	IVD Plot for Maser 33 of Observation BS198B	103
E.9	IVD Plot for Maser 43 of Observation BS198B	104
E.10	IVD Plot for Maser 44 of Observation BS198B	105
E.11	IVD Plot for Maser 45 of Observation BS198B	106

# List of Tables

1.1	The frequencies corresponding to the 6 hyperfine transitions between the $6_{16}$ to $5_{23}$ states of the ortho- $\text{H}_2\text{O}$ molecule shown in Figure (1.7). . . . .	14
1.2	The number of transitions due to Zeeman splitting of the three strongest hyperfine lines in ortho- $\text{H}_2\text{O}$ . . . . .	15
2.1	AIPS data calibration steps for spectral line VLBA data. . . . .	27
3.1	Gaussian fit parameters from BS198A masers . . . . .	37
3.1	continued. . . . .	38
3.1	continued. . . . .	39
3.2	Gaussian fit parameters from BS198B masers . . . . .	41
3.2	continued. . . . .	42
3.2	continued. . . . .	43
3.3	Magnetic Field Parameters . . . . .	51
4.1	Intensity Comparison of Masers from Both Epochs . . . . .	55

# Abbreviations

<b>MASER</b>	<b>M</b> icrowave <b>A</b> mplification by <b>S</b> timulated <b>E</b> mission of <b>R</b> adiation
<b>NRAO</b>	<b>N</b> ational <b>R</b> adio <b>A</b> stronomy <b>O</b> bservatories
<b>VLBA</b>	<b>V</b> ery <b>L</b> ong <b>B</b> aseline <b>A</b> rray
<b>GBT</b>	<b>G</b> reen <b>B</b> ank <b>T</b> elescope
<b>AOC</b>	<b>A</b> rray <b>O</b> perations <b>C</b> enter
<b>AIPS</b>	<b>A</b> stronomical <b>I</b> mage <b>P</b> rocessing <b>S</b> ystem
<b>VLA</b>	<b>V</b> ery <b>L</b> arge <b>A</b> rray
<b>VLBI</b>	<b>V</b> ery <b>L</b> ong <b>B</b> aseline <b>I</b> nterferometry
<b>FWHM</b>	<b>F</b> ull <b>W</b> idth <b>H</b> alf <b>M</b> aximum
<b>RCP</b>	<b>R</b> ight <b>C</b> ircular <b>P</b> olarization
<b>LCP</b>	<b>L</b> eft <b>C</b> ircular <b>P</b> olarization
<b>LOS</b>	<b>L</b> ine <b>O</b> f <b>S</b> ight
<b>LSR</b>	<b>L</b> ocal <b>S</b> tandard of <b>R</b> est

# Physical Constants

Speed of Light  $c = 2.997\,924\,58 \times 10^5 \text{ km s}^{-1}$  (exact)

22 GHz H<sub>2</sub>O Zeeman Splitting Factor  $z = 2.1 \text{ Hz mG}^{-1}$

# Symbols

$I$  Intensity Jy ( $\text{W m}^{-2} \text{Hz}^{-1}$ )

$P$  power W ( $\text{J s}^{-1}$ )

$\omega$  angular frequency  $\text{rad s}^{-1}$

*For my mother and father, who taught me the value of hard work, and without whose support these past years would not have been possible . . .*

# Chapter 1

## Introduction

High mass stars play a dominant role in the evolution of the galaxies within our universe. Unlike the lifecycle of low mass stars, a deep understanding of the early stages of high mass stellar evolution is not yet within our grasp. This is because high mass stars are more difficult to observe due to a number of factors including a shorter lifespan, a low population, a tendency to form in clusters, and a tendency to be a greater distance away. As a result, observations need to be done using a high angular resolution. Of particular interest is the role played by the magnetic field in the high mass star formation process. To probe the early stages of high mass stellar evolution, 22 GHz H<sub>2</sub>O masers are a useful tool due to their compact nature and high intensity emissions. Observation of the Zeeman effect in H<sub>2</sub>O masers also give us a means to measure the magnetic field strength in these regions.

In this thesis, we present the observations of H<sub>2</sub>O masers in the star forming region W3(OH). The observations were made using the Very Long Baseline Array (VLBA) radio telescope at two epochs separated by six months. During the second epoch, the masers in W3(OH) were in a flaring state, as opposed to a quiescent state in the first epoch. In this chapter, we begin with a discussion on high mass star formation in §1.1, discuss masers in §1.2, discuss the H<sub>2</sub>O maser in greater detail in §1.3, and finish the chapter in §1.4 and §1.5 with a discussion of the Zeeman effect. In Chapter 2 we discuss the theoretical framework behind the field of radio interferometry, data calibration, and data imaging. In Chapter 3 we present our results and discuss these results in Chapter 4. Finally, in Chapter 5 we state our conclusions.

## 1.1 High Mass Star Formation and Magnetic Fields

High mass stars, defined by having a mass greater than or equal to eight times the mass of our Sun play an important role in the evolution of the Galaxy. With strong stellar winds and molecular outflows, they are responsible for introducing a vast amount of energy and momentum into the interstellar medium throughout their life cycles. They frequently end their lives in a spectacular explosion, known as a supernova, sending matter and energy into the interstellar medium which will become the materials that give birth to a new generation of stars and solar systems. High mass stars have a shorter lifespan than lower mass stars because they burn fuel at a much quicker rate. A star with 10 times the mass of the sun will have a lifespan of roughly 1000 times shorter than the sun, and thus will only live  $1 \times 10^7$  yr. Though we have a very good understanding of the life cycle of a lower mass star, our understanding of the life cycle of high mass stars is not as vast. Observations are difficult, as the regions tend to contain a lot of dust and so are heavily obscured. High mass star forming regions are also rare and therefore tend to be far from Earth, requiring observations to have high spatial resolution. They also pose theoretical difficulties, as they begin burning their nuclear fuel and radiating energy while still accreting. This radiation pressure can be large enough to exceed the acceleration due to gravity. This is problematic, as it is not understood how they sustain a sufficient accretion rate despite the radiation pressure.

Though our understanding of the process is not complete, there are two competing theories, one of which contends that the magnetic field plays a vital role in the formation process of high mass stars, the other states that high mass star formation is regulated by turbulence. In the first theory, magnetic fields play the role of supporting potential star forming structures against collapse, thus keeping them from “turning on”, and until the magnetic flux is lowered by some mechanism the gravitational collapse required for the star to form will not occur. The magnetic field offers support by directly influencing the ionized matter, and also indirectly influencing non-ionized matter that happens to be coupled to ionized matter through collisions, in a phenomenon known as flux freezing. Flux freezing, or reduction in magnetic flux, is believed to occur when the density of ions becomes small as compared to that of neutral matter in the molecular cloud that the neutral particles will no longer be coupled to ions. When flux freezing breaks down, deep in the interior core of the forming star where ionizing cosmic rays have

only a minute effect, neutral matter will begin to slip past the ions, clump in the center of the forming star, and thus initiate the collapse (Shu et al.1987). The second theory states that the turbulence responsible for providing molecular clouds support against gravitational collapse on large scales also creates inhomogeneities in density on small scales. It are these inhomogeneities that set the stage for future collapse (Padoan et al.2002). The point of this thesis is not to lend credence to either theory, but to compare magnetic field values observed between two epochs in the star forming region W3(OH). The 22 GHz H<sub>2</sub>O masers present in early stages of high mass star formation give us an excellent means to observe magnetic fields in high density regions because of their associated detectable Zeeman effect. The work in this thesis is part of a larger and long term effort to gather information on the strengths of magnetic fields in high mass star forming regions.

### 1.1.1 Observational Signatures of Star Formation

After collapse is initiated in the core of a molecular cloud, the resulting protostar is believed to accrete mass from a protostellar disk. This phase of stellar formation is also often accompanied by bipolar outflows in which a vast amount of matter and momentum is released into the interstellar medium in a direction perpendicular to the plane of the disk. These outflows are often traced by masers of certain species depending on the age of the star forming region. Figure (1.2) illustrates this, in which we can see the circumstellar disk from which the young protostar is accreting material, and perpendicular to this the bipolar outflows which carry material out into the interstellar medium. We will use these ideas to interpret the morphology of our masers in §4.3.

## 1.2 Masers

Astrophysical masers are a naturally occurring source of stimulated line emission. A maser, an acronym for Microwave Amplification by Stimulated Emission of Radiation, is much like a laboratory laser, in that it is monochromatic, with frequency corresponding to the energy difference between the quantum energy levels of the molecule being pumped. However, masers occur in the microwave region of the electromagnetic spectrum. Masing occurs when a collection of molecules of the same species are pumped into higher quantum energy states. Pumping,

or excitation of the molecules, occurs either by radiative or collisional excitation, which leads to a population inversion, a state in which a higher energy state has a larger population than a lower energy state. When a photon of frequency  $\nu$  corresponding to the energy difference between these two states

$$E_2 - E_1 = h\nu \quad (1.1)$$

is incident on one of these molecules, the molecule will transition to the lower state and emit a photon of frequency  $\nu$  (Figure 1.1). So there are now two photons of frequency  $\nu$ , and these two photons will then come into contact with two more molecules, thus producing an overall four photons. The photon number will continue to grow in such a manner depending on the population of molecules in the excited state. This emission produces photons that are all in phase, are similarly polarized and have the same frequency. As the amplification is related to the population density of the molecules, the longest path through the group of molecules appears more intense than the shorter paths. Thus astrophysical masers appear very compact and bright, and are excellent as a tool to trace the activity in an astronomical source.

Masing in astrophysics was first proposed by Perkins et al.(1966) to explain the intense OH emission that had been recently discovered in several H II regions. Moran et al.(1967) was the first to use Very Long Baseline Interferometry (VLBI) to study maser emission in the H II region W3. With these studies they were able to determine the compactness of the maser emission, which enables high resolution studies to observe and track localized phenomena with very high precision. Astrophysical maser emission has now been observed for multiple species of molecules, including but not limited to OH, H<sub>2</sub>O, NH<sub>3</sub>, CH, H<sub>2</sub>CO, etc. Each molecular species requires different conditions for masing, and thus masers are a means to determine other activity within the spatial region. As an example, both H<sub>2</sub>O and class I methanol masers are known to occur in shocked regions, and therefore can be used for studying protostellar outflows.

Masers are not only useful for observing the physical attributes of astronomical structures, but can also be used to detect magnetic fields via the Zeeman effect (see §2.5). For instance, Sarma et al.(2008) was able to use H<sub>2</sub>O masers to observe the Zeeman effect within the star forming region OH 43.8-0.1. Using this observation they were able to detect magnetic field parameters for seven masers. Knowing

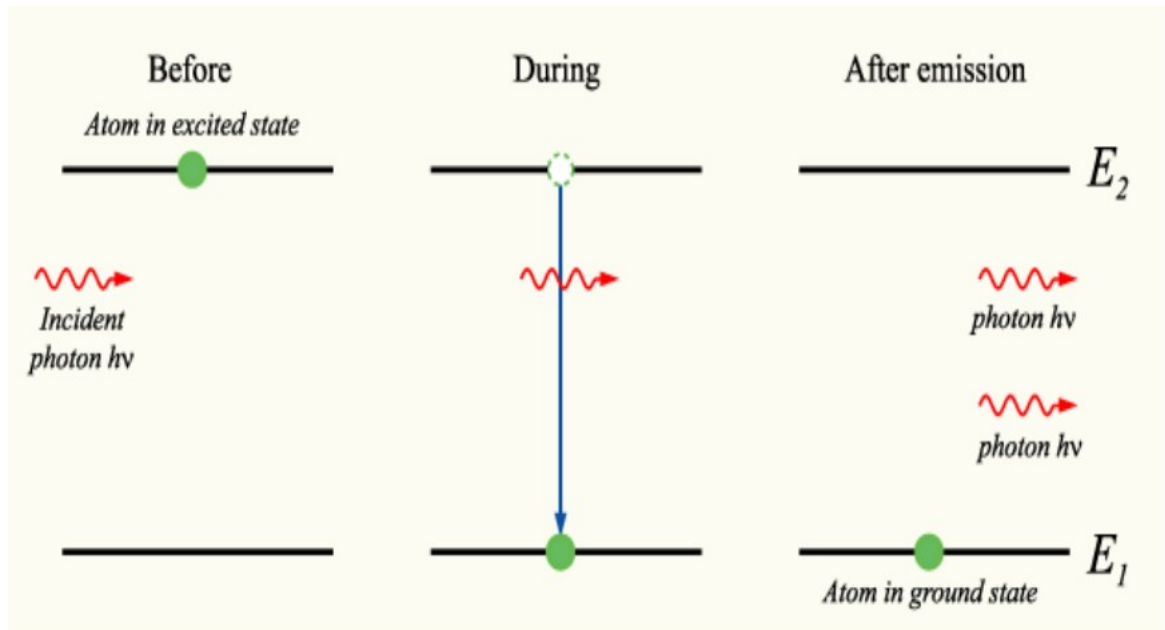


FIGURE 1.1: When an incident photon with frequency corresponding to the energy difference between the levels shown in the figure is incident on the atoms (or molecules), we get a transition between the two levels, so that the end result is two photons leaving the atom/molecule (extreme right panel). Image courtesy of the “Astrophysical Masers” lecture by Dr. Lisa Harvey-Smith, University of Sydney.

the magnetic field of a star forming region could help us better understand the stellar formation process, and thus masers can be used to gather a vast amount of information about these regions at different stages of the star formation process.

### 1.3 H<sub>2</sub>O Masers and the H<sub>2</sub>O Molecule

As the purpose of this thesis is to compare magnetic field strengths of the star forming region W3(OH) for two epochs by using observations of H<sub>2</sub>O masers and the Zeeman effect, we will use this section to discuss necessary properties of the 22 GHz rotational transition of the H<sub>2</sub>O molecule. We begin this section with a discussion on rotational transitions in molecules, then progress to a discussion of the 22 GHz rotational transition in the H<sub>2</sub>O molecule, and conclude with a discussion on the properties of H<sub>2</sub>O masers.

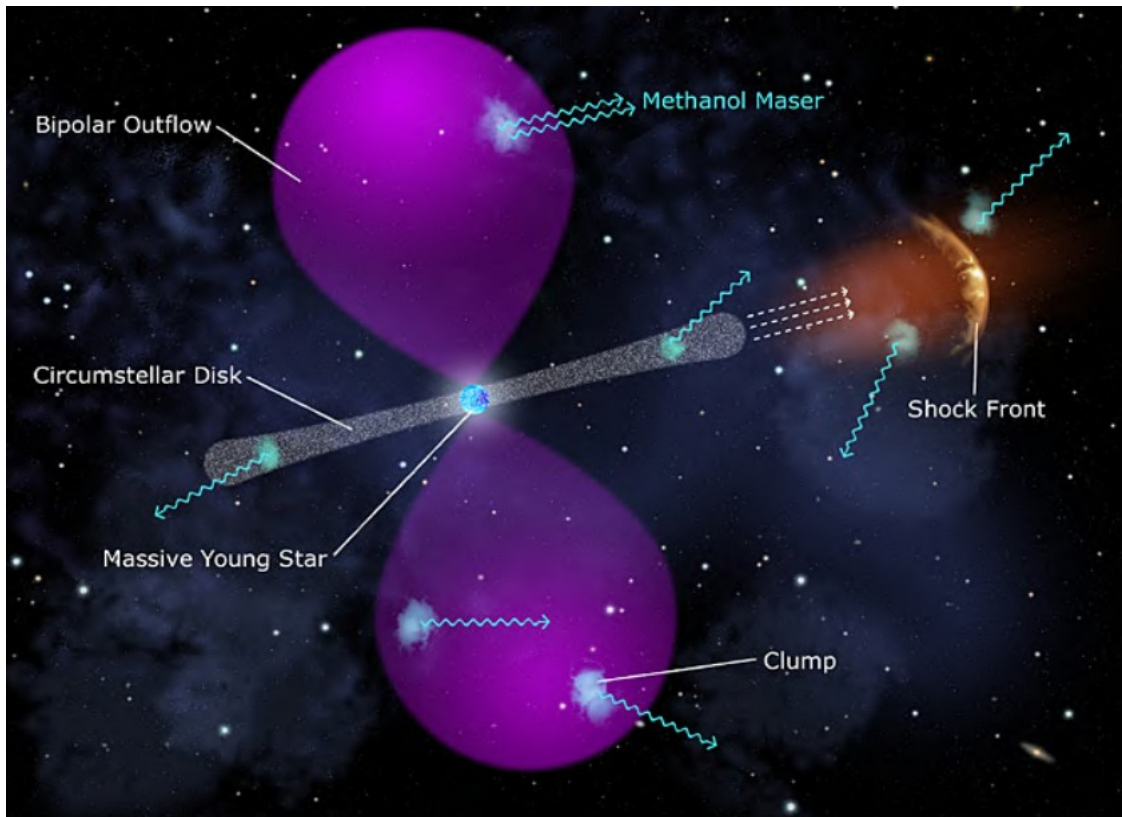


FIGURE 1.2: A depiction of a bipolar outflow of a protostellar region, as well as the methanol masers tracing the outflows and shock-fronts of the region. Image courtesy of the “Astrophysical Masers” lecture by Dr. Lisa Harvey-Smith, University of Sydney.

On top of the electron transitions in their constituent atoms, molecules also exhibit additional degrees of freedom which undergo energy transitions. These are rotational and vibrational motion. We tend to describe molecular rotation in regards to a coordinate system consisting of three principal axes with the molecular center of mass at the origin point. Principal axes are defined such that the moment of inertia is a maximum along one axis, a minimum along another, and a third axis that is perpendicular to the other two. Another way which we define the principal axes is that the angular momentum vector and the angular velocity vector are the same in direction for rotations around these axes, which is unique solely to the principal axes.

To discover the principal axes of the  $\text{H}_2\text{O}$  molecule, we begin by searching for an axis of symmetry, as this will always constitute a principal axis. This axis will bisect the angle formed by the hydrogen nuclei with the oxygen nucleus at the

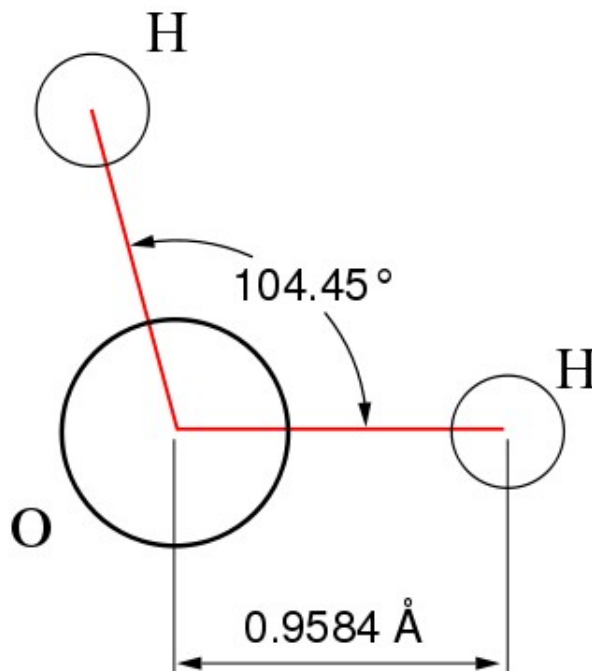


FIGURE 1.3: A diagram of the  $\text{H}_2\text{O}$  molecule. The axis of symmetry of the molecule bisects the angle between the hydrogen atoms.

vertex (see Figure 1.3). This is an axis of symmetry as a plane perpendicular to the plane of the molecule with its line of intersection at this principal axis will act as a plane of reflection, since a reflection across this plane will return the same molecule. A second principal axis can be found by taking an axis perpendicular from the plane of reflection that passes through the center of mass, and the final is to take an axis perpendicular to the first two which passes through the center of mass. A moment of inertia about one of these three principal axes is known as a principal moment of inertia of which there are three,  $I_a$ ,  $I_b$  and  $I_c$ , with  $I_a \leq I_b \leq I_c$ . The  $\text{H}_2\text{O}$  molecule is an example of a asymmetric rotator, defined by  $I_a \neq I_b \neq I_c$ . Thus, each principal axis has a different moment of inertia.

The  $\text{H}_2\text{O}$  molecule is an asymmetric rotator with a complex level structure. Figure (1.4) depicts the rotation levels of the orth- $\text{H}_2\text{O}$  molecule in which the rotation levels are labeled  $J_{K_-K_+}$ , where  $J$  is the total angular momentum and both  $K_-$  and  $K_+$  are known as the asymptotic quantum numbers, which are its projections on the inner axes of the molecule (Varshalovich et al. 2006). The term “ortho” comes as a result of the radiative selection rules for the moments of inertia of the  $\text{H}_2\text{O}$  molecule, which are:

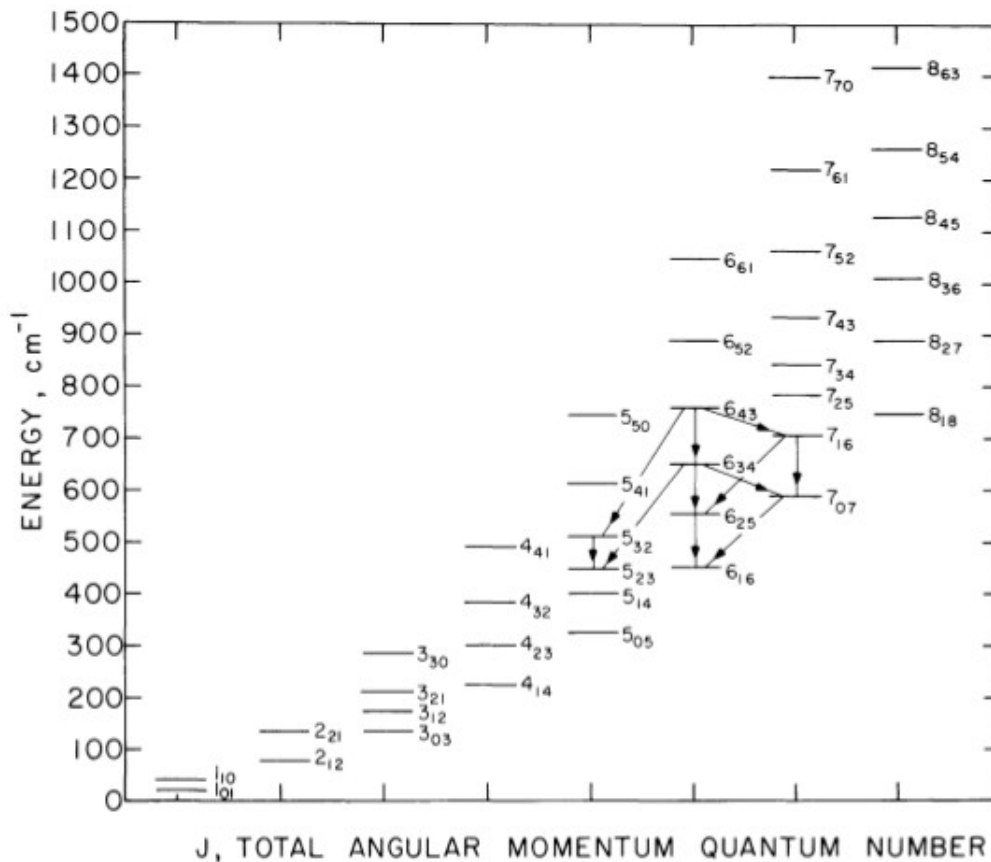


FIGURE 1.4: Energy vs. angular momentum diagram for the ground vibrational state of the H<sub>2</sub>O molecule. The energy levels are specified by the total rotational angular momentum quantum number,  $J$ , along with the two quantities  $K_-$  and  $K_+$  that are explained in §1.3. This figure courtesy of Turner (1970).

- $K_-$  and  $K_+$  must change the evenness of their value
- $\Delta J = 0, \pm 1$

This results in two distinct, radiatively uncoupled species of H<sub>2</sub>O. These are ortho-H<sub>2</sub>O with nuclear spin 1 and  $|K_-, K_+ \rangle = |\text{even}, \text{odd} \rangle$  or  $|\text{odd}, \text{even} \rangle$ , and para-H<sub>2</sub>O with nuclear spin 0 and  $|K_-, K_+ \rangle = |\text{even}, \text{even} \rangle$  or  $|\text{odd}, \text{odd} \rangle$  (Cooke et al. 1985). Note in Figure(1.4) that the ground state is not listed in the diagram, as this belongs to para, not ortho, H<sub>2</sub>O (Elitzur 1992).

The first discovery of maser emission was of the  $6_{16} \rightarrow 5_{23}$  transition in the ortho-H<sub>2</sub>O molecule with a frequency of 22 GHz (wavelength of 1.35 cm). It was first detected by Cheung et al. (1969) towards numerous star forming regions. Ever

since, masers from this transition have been discovered in multiple star forming regions, external galaxies and late-type stars. Additional H<sub>2</sub>O masers lines were later discovered at sub-millimeter wavelengths.

As it is the 6<sub>16</sub>→5<sub>23</sub> transition that will result in our maser emission, we will now discuss this transition in more detail. When pumped into higher energy levels, molecules have a tendency to step down in energy levels within the same J value, and occupy the lowest possible energy level in a certain J value. For instance, with numerous levels associated with J=6, they will tend to occupy the 6<sub>16</sub> state. The 5<sub>23</sub> state, by contrast, will decay into multiple different energy levels within the J=5 group. Under certain conditions, a population inversion can be obtained between the 6<sub>16</sub> and 5<sub>23</sub> states. As described in §1.2, this can lead to a chain of stimulated emission, developing the intense maser emission we observe for this thesis. There is nothing particularly special about the 6<sub>16</sub> →5<sub>23</sub> transition compared to other maser lines in the same molecule. At a 1.35 cm wavelength, the longest wavelength among the possible observed transitions, and with brightness temperature  $\propto \lambda^2$ , it has the highest intensity, and is therefore the easiest to observe.

Shock fronts provide a natural location to observe water masers as they are collisionally excited. The necessary energy to pump the maser is provided by the relative kinetic energies of the shocked and unshocked gas (Elitzur 1992). Studies show that shocks in dense clouds, with pre-shock number densities,  $n_o \sim 10^7 \text{cm}^{-3}$  will develop a high density plateau with  $n \sim 10^9 \text{cm}^{-3}$  and post shock temperature  $T \sim 400 \text{K}$  (Elitzur 1992). Such high temperatures in shock fronts cause chemical reactions that produce a vast amount of H<sub>2</sub>O. This plateau makes a perfect site for H<sub>2</sub>O maser pumping. Typical parameters for H<sub>2</sub>O masers are a diameter  $\sim 10^{13} \text{cm}$ , density  $\sim 10^9 \text{cm}^{-3}$ , and brightness temperature  $\sim 10^{12} \text{K}$ .

## 1.4 The Zeeman Effect

Named after Dutch physicist Pieter Zeeman, the Zeeman effect is the only direct observational method to measure astronomical magnetic field strengths. As a simple demonstration of the Zeeman effect, we will discuss the effect of an external magnetic field on the 1s and 2p atomic energy levels. The abbreviations “s” and “p” are associated with the angular momentum quantum number, l. A level with l=0 is given the designation “s”, and a level with l=1 the designation “p”. It is also

common practice to precede this designation with the integer value of the principal quantum number,  $n$ . Thus, “2p” is designated for a level that has quantum number  $n=2$  and angular momentum  $L=1$ .

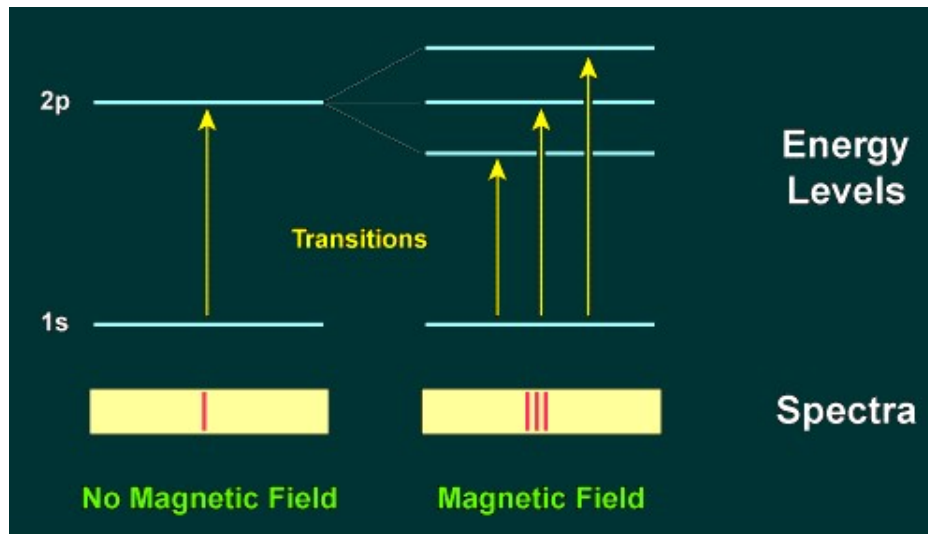


FIGURE 1.5: Figure displaying energy level transition from the  $1s \rightarrow 2p$  states. In the presence of an external magnetic field, the 2p state splits into three states. This splitting is known as the Zeeman effect. The splitting can be visually seen in the spectra as the spectral line will split into three spectral lines centered on the original.

As seen in Figure 1.5, in the presence of an external magnetic field, the energy level has a potential to “split” into multiple levels. The number of split levels associated with the angular momentum quantum number is equal to  $2L+1$ , and so the lowest considered energy level, 1s, with angular momentum quantum number  $L=0$  will show no splitting, whereas the higher level, 2p, will display a splitting of a single transition into 3 separate transitions. These splitting transitions are then designated by the magnetic spin quantum numbers,  $m_e$ , which hold values of  $\pm 1$ . Thus, as the 2p state has value  $l=1$ , the splitting transitions will have magnetic spin quantum numbers  $m_e = 0, \pm 1$ . This splitting effect can be seen in the emission spectra, as a single spectral line will split into multiple (in this case three) distinct spectral lines. The greater the external magnetic field, the greater the observed splitting will be.

The desired result of this is to measure the magnetic field by measuring the amount of splitting that is observed. However, with the exception of OH masers, the splitting will end up being much smaller than the observed line-width of the spectral

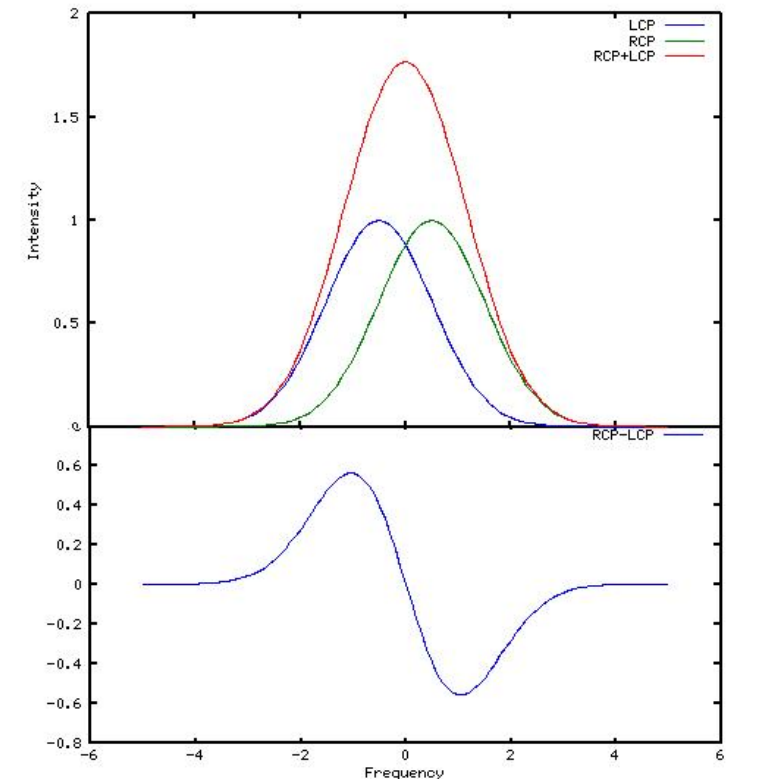


FIGURE 1.6: Upper Panel: Figure showing the frequency offset between the Right Circular Polarization (RCP) and Left Circular Polarization (LCP) of a spectral line due to the Zeeman effect in an external magnetic field, as well as the total Intensity (RCP+LCP) of the line. Lower Panel: Taking the difference of the RCP and LCP components (RCP–LCP) yields an S-curve. The vertical axis in both panels is intensity in arbitrary units, and the horizontal axis is frequency (which is usually expressed in terms of the equivalent Doppler-shifted velocity; see equation 2.17). The characteristics of this S-curve give us a means to measure the amount of splitting, and thus the strength of the external magnetic field.

line. We measure the line-width of a spectral line by plotting the intensity over the frequency (or equivalently, Doppler-shifted velocity), and then measuring the full width at half maximum (FWHM) of the line (the width in frequency between the two points corresponding to half of the intensity). We denote this quantity  $\Delta\nu_{FWHM}$ . Though this appears to be an obstacle, transitions between the 2p,  $m_e = +1$  to the 1s state and the 2p,  $m_e = -1$  to the 1s state are oppositely circularly polarized. Thus, if we measure the right (RCP) and left (LCP) circular polarization components we will observe a small frequency, and thus velocity, shift between them due to the Zeeman effect. This can be seen in Figure (1.6).

If we take the difference of the circular polarization values, RCP–LCP, we will

obtain the S-shaped profile that can be seen in the lower panel of Figure (1.6). Summing the two will give us the total intensity seen in the upper panel. These are defined as the Stokes V and I parameters, respectively. Further discussion of the Stokes parameters is put off until §2.5. Upon inspection one might notice that the Stokes V profile appears to be (and is) the derivative of the Stokes I profile. It is the small frequency shift in the RCP and LCP due to the Zeeman effect that causes the Stokes V profile to look like the derivative of the Stokes I profile, and thus, if we find the Stokes V profile from our observation, and fit the derivative of the Stokes I profile to it, we will be able to obtain the frequency splitting due to the Zeeman effect, and hence obtain a value for the strength of the magnetic field. Further discussion of this is left for §2.5.

## 1.5 The Zeeman Effect and the H<sub>2</sub>O Molecule

In this thesis, we aim to compare magnetic field strengths of the star forming region W3(OH) between two different epochs using the Zeeman effect. Thus, in §1.5, we discuss the Zeeman splitting of the  $6_{16} \rightarrow 5_{23}$  rotational transition of ortho-H<sub>2</sub>O. We begin this section with a discussion of hyperfine structure.

### 1.5.1 Hyperfine-Structure

Hyperfine structure, also known as hyperfine splitting, is a minute splitting in the observed spectral lines of an atom or molecule due to magnetic interactions between the orbiting electrons and the atomic nuclei. As we focus our studies on the  $6_{16}$  and  $5_{23}$  states and their transition which results in the 22 GHz emission, we only need concern ourselves with ortho-H<sub>2</sub>O. Ortho-H<sub>2</sub>O states display hyperfine splitting as a result of having a total nuclear spin of 1 ( $I=1$ ); para-H<sub>2</sub>O, with  $I=0$ , displays no hyperfine splitting.

The hyperfine structure observed in the ortho-H<sub>2</sub>O rotational levels results from two factors. The first is the coupling of the proton nuclear spins with the rotational angular momentum ( $\vec{I} \cdot \vec{J}$ ). The second comes as a result of the spin-spin interaction of the hydrogen nuclei ( $\vec{I} \cdot \vec{I}$ ), where  $\vec{I}$  is the total nuclear spin.  $\vec{I} = j_p + j_p$ , where  $j_p$  are the nuclear spins of the hydrogen nuclei ( $j_p = \frac{1}{2}$ ). The nuclear spin of

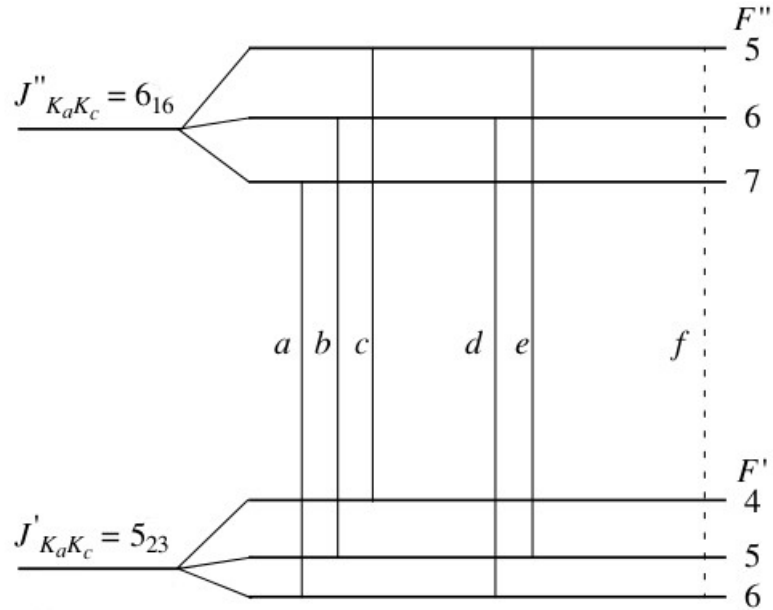


FIGURE 1.7: Diagram of the  $6_{16}$  and  $5_{23}$  rotational states for ortho- $\text{H}_2\text{O}$ , along with their corresponding hyperfine structure levels. The lines marked “a” through “f” correspond to the possible transitions between the hyperfine levels, where “a”, “b” and “c” are the 3 most intense transitions. Diagram taken from Varshalovich et al. (2006).

$^{16}\text{O}$  is equal to zero (Varshalovich et al. 2006). For ortho- $\text{H}_2\text{O}$ ,  $\vec{I}=1$  (Golubiatnikov et al. 2006).

Each of the ortho- $\text{H}_2\text{O}$  rotational levels are split into 3 hyperfine structure levels,  $F$ , with  $F=J+1, J, J-1$ , and the total angular momentum,  $\vec{F}$ , of the system is  $\vec{F} = \vec{J} + \vec{I}$ . Figure (1.7) is a diagram depicting all of the hyperfine levels associated with the  $6_{16}$  level, which are  $F=5,6,7$ , and with the  $5_{23}$  level, which are  $F=4,5,6$ . Also featured are the possible transitions between these two levels, governed by selection rule  $\Delta F=0, \pm 1$ . Figure (1.8) shows the relative intensities of these transitions, where the most intense 3 transitions correspond to those listed as “a”, “b” and “c” in Figure (1.7). The frequencies corresponding to these transitions can be seen in Table (1.1), and were taken from Varshalovich et al. (2006). Nedoluha et al. (1992) showed that the 22 GHz maser emission we have observed is composed of the three strongest hyperfine lines.

Hyperfine Transition Frequencies		
Label	Transition	Frequency (kHz)
a	F = 7-6	22235044.000
b	F = 6-5	22235077.066
c	F = 5-4	22235120.338
d	F = 6-6	22235252.794
e	F = 5-5	22235297.842
f	F = 5-6	22235473.570

TABLE 1.1: The frequencies corresponding to the 6 hyperfine transitions between the  $6_{16}$  to  $5_{23}$  states of the ortho- $\text{H}_2\text{O}$  molecule shown in Figure (1.7). These frequencies, based on experimental data, were taken from Varshalovich et al. (2006). The first column corresponds to the label given to the transition in Figure (1.7).

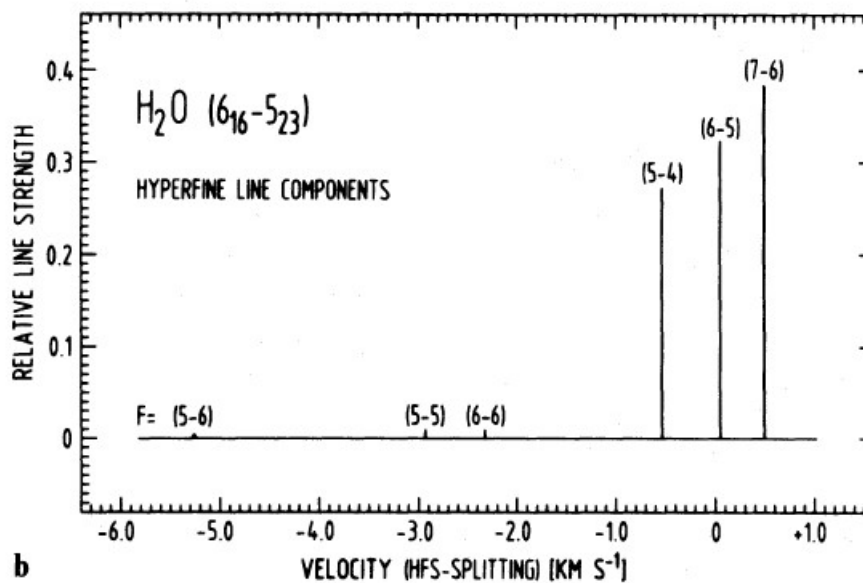


FIGURE 1.8: Figure displaying the relative intensities of the hyperfine level transitions of the  $6_{16}$  and  $5_{23}$  states of ortho- $\text{H}_2\text{O}$ . Image taken from Fiebig et al. (1989).

### 1.5.2 Zeeman Splitting of the $6_{16} \rightarrow 5_{23}$ Transition

When placed into an external magnetic field, the hyperfine levels of the ortho- $\text{H}_2\text{O}$  molecule will split into multiple levels as a result of the Zeeman effect. The number of sublevels is equal to  $(2F+1)$ , and so the  $F=7$  level will be split into 15 sublevels, the  $F=6$  level into 13 sublevels, the  $F=5$  level into 11 sublevels, and the  $F=4$  level

into 9 sublevels. The sublevels are given the label  $M_F$ , and  $M_F$  goes from  $-F$  to  $F$  in increments of 1 ( $-F, -F+1, -F+2, \dots, 0, \dots, F-2, F-1, F$ ). The sublevels follow selection rule  $\Delta M_F = 0, \pm 1$ . The number of transitions between these sublevels is given in Table (1.2).

Number of Transition Components	
Transition	Number of Transition Components
F=7-6	39
F=6-5	33
F=5-4	27

TABLE 1.2: The number of transitions due to Zeeman splitting of the three strongest hyperfine lines in ortho-H<sub>2</sub>O.

As a result of the Zeeman effect, some of the hyperfine transitions components are linearly polarized, while others are circularly polarized. For example, the transition F=7–6, which is comprised of 39 components, 13 correspond to  $\Delta M_F = 0$  which are linearly polarized, and 26 correspond to  $\Delta M_F = \pm 1$  which are circularly polarized. Figure (1.9) shows the 15 sublevels corresponding to F=7, the 13 sublevels corresponding to F=6, as well as the 39 transitions which take place between them due to the Zeeman effect. Nedoluha et al. (1992) showed that the magnetic field can be calculated due to these components, the process for which is described in detail in §2.5.

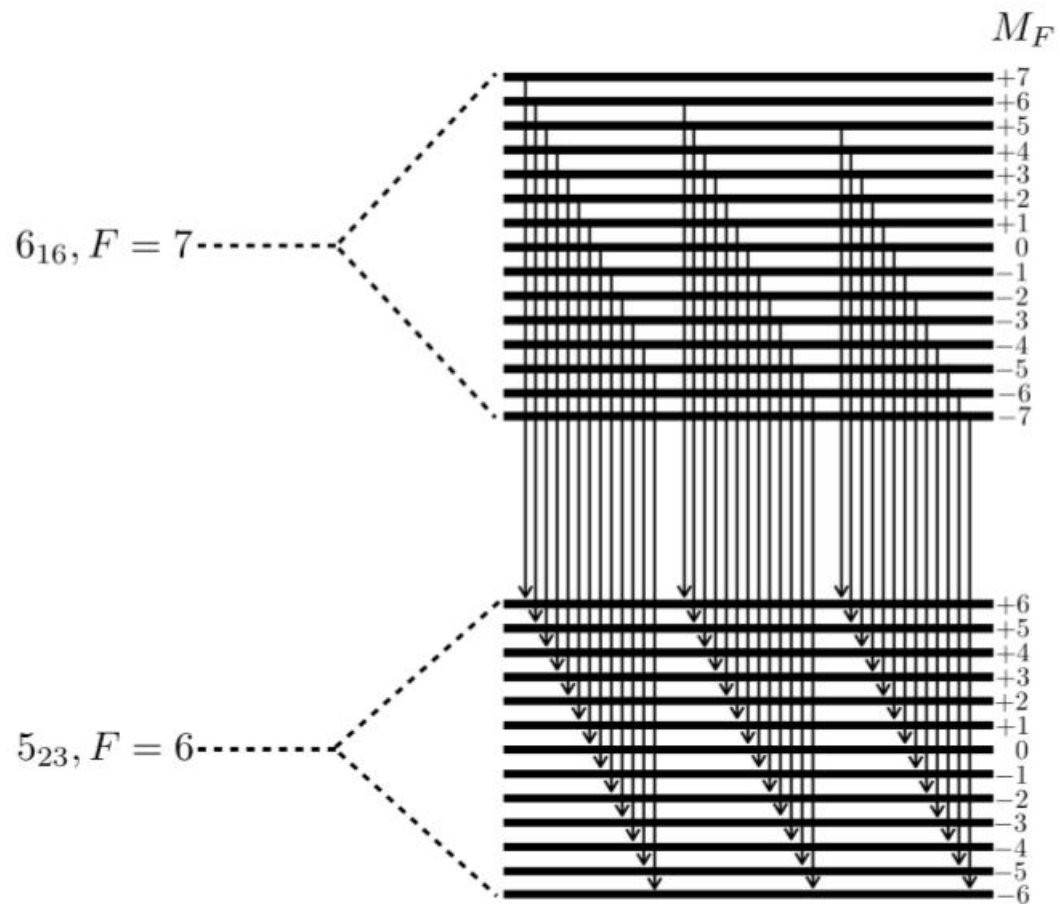


FIGURE 1.9: Diagram showing the 39 components of the  $F=6-7$  transition of ortho- $\text{H}_2\text{O}$  due to the Zeeman effect. Of the 39 components, 13 correspond to linear polarization ( $\Delta M_F=0$ ), and 26 to circular polarization ( $\Delta M_F = \pm 1$ ).

# Chapter 2

## Observations and Data Reduction

We begin this chapter with a discussion of radio interferometry in §2.1, as well as describe the Very Long Baseline Array (VLBA) Telescope which we used for our observations. In §2.2 we discuss the parameters of our observations, followed by the data calibration and imaging steps in §2.3 and §2.4, respectively. We finish with a discussion on measuring the magnetic field using the Zeeman effect in §2.5.

### 2.1 Radio Interferometry

#### 2.1.1 Interferometry in Astronomy

One of the biggest issues one faces while designing a telescope is the desire for the instrument to be able to see the small scale structure of objects located very far away. The angular resolution ( $\theta$ ) of an optical instrument is proportional to the wavelength of the light being observed ( $\lambda$ ) divided by the aperture of the instrument ( $D$ ). In a radio antenna, the aperture of the instrument is the size of the effective diameter of the instrument. As we want  $\theta$  to come out as small as possible, thus giving us the best resolution, this poses a problem for single dish telescopes. We would need a dish of tremendous size to begin seeing small scale structure at radio wavelengths. Such large dishes would create operating difficulties due to their size. For example, the world's largest single dish radio telescope is the Arecibo Observatory in Puerto Rico, which has a dish with diameter 305 m. At this size the telescope is already so difficult to move that it can only view a  $40^\circ$  cone of visibility about its zenith.

It is clear that there is a limit to the size of single dish radio telescopes. At a certain point the construction of such a dish becomes impractical, for issues with both engineering design and monetary funding. So to obtain ever greater angular resolution we rely on the principles of interferometry. Interferometry works by combining the signals from multiple single dish radio antennas. The aperture size of a radio interferometer is not based on the diameter of any single dish, but by the length of its longest baseline (the distance between two antennas). This means that a single dish with a diameter of 1 km will have the same angular resolution as two antennas spaced 1 km apart. As a result, we can build radio telescopes of ever increasing aperture size to form telescopes the size of cities, states, or even the diameter of the Earth itself.

### 2.1.2 The VLBA Telescope

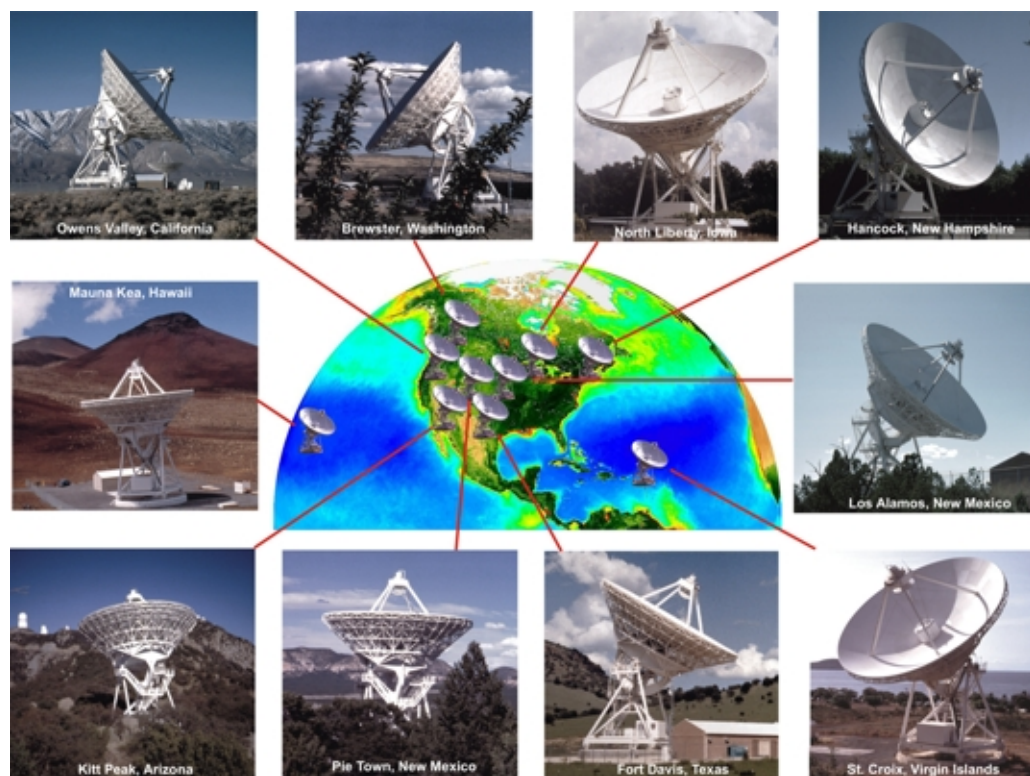


FIGURE 2.1: The locations of the ten VLBA antennas. Image courtesy of the NRAO website.

Brought online in May, 1993, the Very Long Baseline Array Telescope is a pinnacle of modern astronomy. The VLBA is comprised of ten identical radio antennas located throughout the United States, with its longest baseline stretching from

St. Crouix in the U.S. Virgin Islands to Mauna Kea, Hawaii, an impressive 8,611 kilometers. Each VLBA antenna has a 25 meter diameter dish, stands ten stories tall when pointed at the zenith, and has a weight of approximately 240 tons. Each of the ten VLBA antenna locations also houses a control station where the antenna functions are maintained and the data recorded. The data from each antenna are then sent to be correlated at the National Radio Astronomy Observatories (NRAO) Array Operations Center (AOC) in Socorro, New Mexico.

The VLBA observes at wavelengths of 28cm to 3mm (frequencies of 1.2 GHz to 96 GHz). Due to its very long baseline, the VLBA has an impressive angular resolution of  $0.001''$  at 22 GHz. To compare, the largest single dish telescope run by the NRAO is the Green Bank Telescope (GBT) with a diameter of about 100m. At 22 GHz, the GBT gives an angular resolution of only  $15''$ .

### 2.1.3 How do Interferometers Work?

Consider a two element interferometer receiving a signal from an astronomical source, a diagram of this can be seen in Figure 2.2. The voltage received by antenna 1 can be expressed as

$$V_1 = V_{1o} \cos(\omega t) \quad (2.1)$$

and the voltage received by antenna 2 can be expressed as

$$V_2 = V_{2o} \cos[\omega(t - \tau_g)] \quad (2.2)$$

where  $\tau_g$  is the time delay between the antennas receiving the signals,  $\omega$  the angular frequency, and  $V_{1o}$  and  $V_{2o}$  the initial voltages. From Figure 2.2 we can calculate the value for  $\tau_g = \vec{b} \cdot \hat{s} / c$ , where  $b$  is the length of the baseline between the receivers,  $\hat{s}$  is a unit vector in the direction of the wavefront, and  $c$  the speed of light. We then combine the signals in a process known as correlation, in which we take the product of the signals and average them

$$V_1 V_2 = V_{1o} V_{2o} \cos(\omega t) \cos[\omega(t - \tau_g)]. \quad (2.3)$$

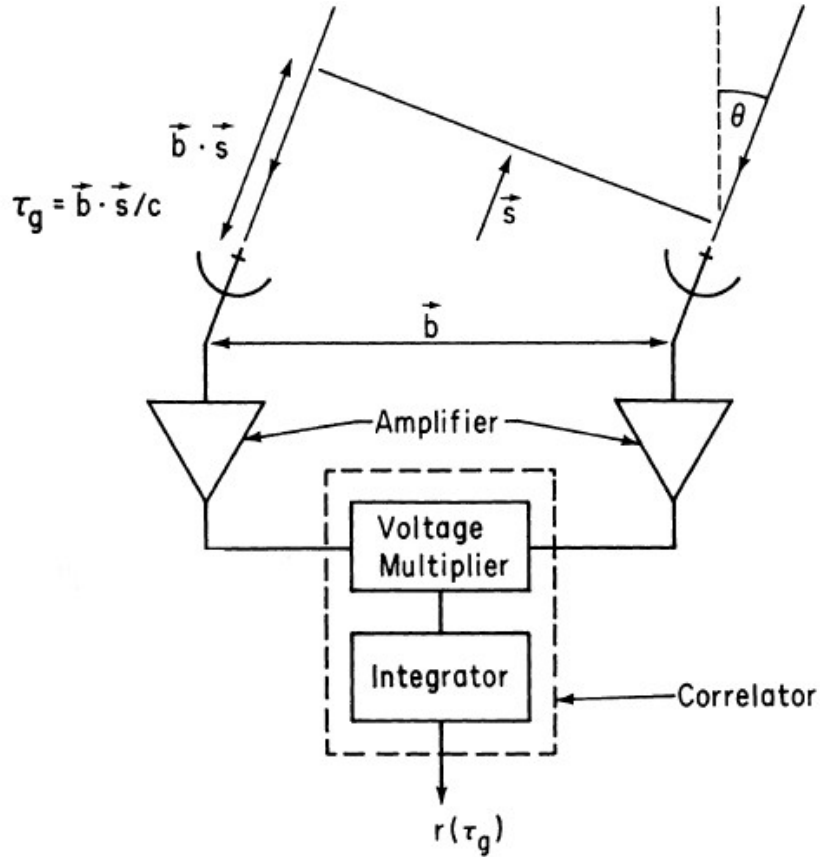


FIGURE 2.2: Diagram of a two element interferometer. The signals received by an astronomical source by these two antennas are multiplied and averaged in the correlator. The quantity  $\tau_g$  represents the geometric time delay between antennas,  $\hat{s}$  is a unit vector perpendicular to the incoming wavefront and facing the source, and  $\vec{b}$  is a vector defining the baseline between the two antennas. (Image courtesy of Rick Perley “Synthesis Imagine in Radio Astronomy” Lectures).

Using the identity  $\cos(\theta)\cos(\phi) = [\cos(\theta-\phi) + \cos(\theta+\phi)]/2$ , and defining  $V_1 V_2 / 2 = P$ , where  $P$  is the power received by the antenna, we can write equation (2.3) as

$$V_1 V_2 = P \{ \cos(\omega\tau_g) + \cos[\omega(2t - \tau_g)] \}. \quad (2.4)$$

In equation (2.4), the  $\cos(\omega\tau_g)$  term is unchanging, whereas the  $\cos[\omega(2t - \tau_g)]$  is rapidly varying. As a result, if we average equation (2.4), only the first term will remain. To complete our correlation we then average  $V_1$  and  $V_2$ , arriving at the correlator response

$$R_c = P \cos(\omega \tau_g) = P \cos \left( 2\pi \nu \frac{\vec{b} \cdot \hat{s}}{c} \right) \quad (2.5)$$

where  $\omega = 2\pi\nu$ , and  $\nu$  is the frequency of the observation. The power received by the antenna is proportional to the intensity ( $P \propto I \propto \sqrt{E}$ ), where  $E$  is the electric field of the source, and  $I$  its intensity.

Our correlator response as seen in equation (2.5) is not yet complete. The equation works very well for a point source, but the source of interest is actually going to have a finite size. To correct for this, we must integrate equation (2.5) over the solid angle subtended by the source. Equation (2.6) is correct, providing the source is spatially incoherent.

$$R_c = \iint P_\nu(s) \cos \left( 2\pi \nu \frac{\vec{b} \cdot \hat{s}}{c} \right) d\Omega \quad (2.6)$$

A means to visualize equation (2.6) was presented by R. Perley in a lecture given at the NRAO Synthesis Imaging Summer School in 2012. The correlator can be thought of as casting a sinusoidal coherence pattern onto the sky with an angular scale  $\lambda/b$ . This corresponds to an antenna spacing as seen in Figure (2.2). The correlator then multiplies the brightness of the source by this coherence pattern, and sums the result over the observed sky. A depiction of this can be seen in Figure (2.3).

The correlator response seen in equation (2.6) is still not complete, as it is only sensitive to the even part of our observed source brightness. To recover the total intensity, we have to introduce a phase shift of  $\pi$  into the signal path for one antenna, and then follow through our correlator steps (equations 2.1 - 2.5). After correlation, we reproduce the odd part of our correlator response by analogy to equation (2.6)

$$R_s = \iint P_\nu(s) \sin \left( 2\pi \nu \frac{\vec{b} \cdot \hat{s}}{c} \right) d\Omega. \quad (2.7)$$

We are now ready to define the complex visibility function from the two correlator response functions,  $R_c$  and  $R_s$ .

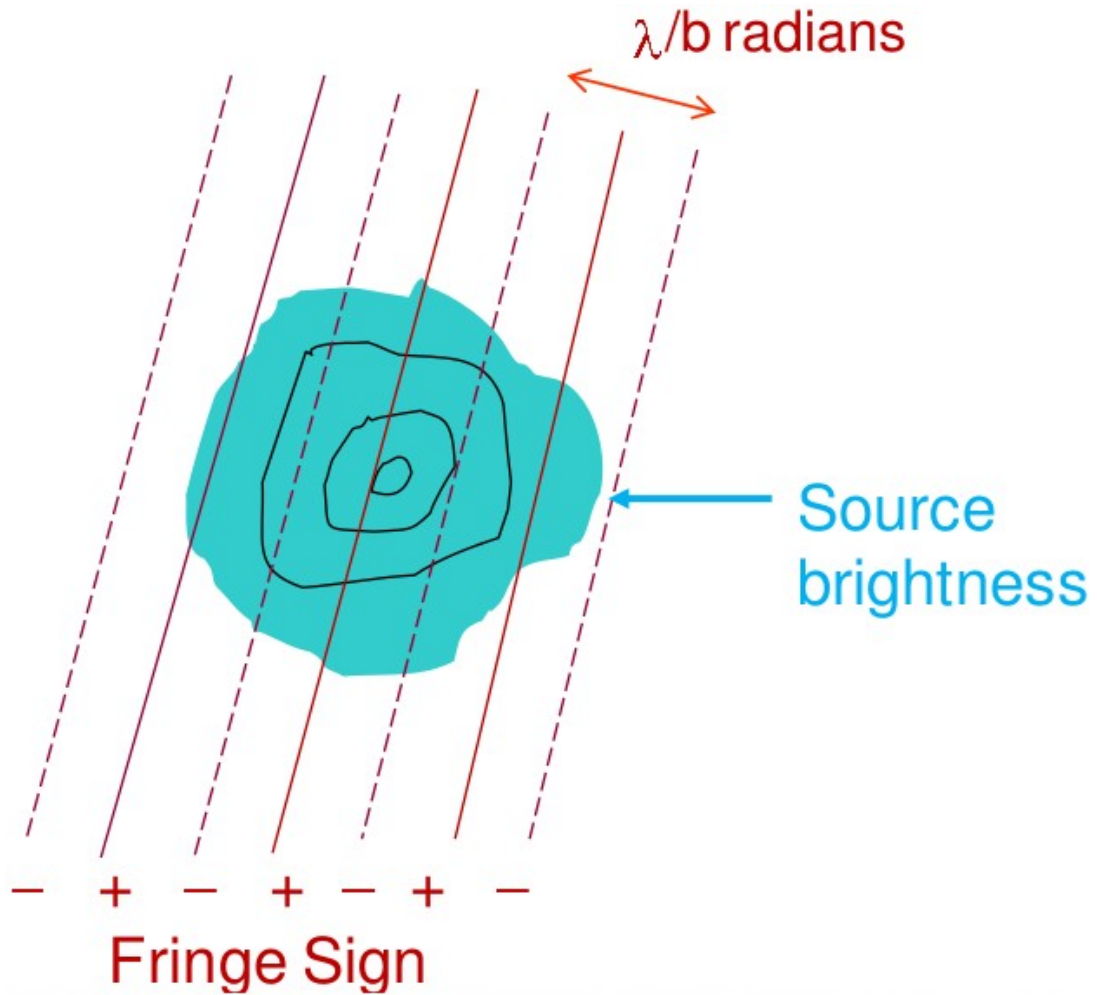


FIGURE 2.3: A way to visualize equation (2.6) taken from R.Perley’s “Synthesis Imaging 2012 Workshop” lecture. Imagine the correlator casting a sinusoidal fringe pattern on the observed region. Antenna arrangement dictates the orientation of the fringe pattern, and the fringe spacing is given by  $\lambda/b$ . The solid lines in the figure represent the peak of the sinusoidal interference pattern, and the dashed lines the trough. The image represents the source being observed, and the contours represent the source intensity. (Image courtesy of Rick Perley “Synthesis Imagine in Radio Astronomy” Lectures).

$$V_\nu(b) = R_c - iR_s = \iint P_\nu(s) \left[ \cos \left( 2\pi\nu \frac{\vec{b} \cdot \hat{s}}{c} \right) - i \sin \left( 2\pi\nu \frac{\vec{b} \cdot \hat{s}}{c} \right) \right] d\Omega \quad (2.8)$$

Equation (2.8) simplifies to

$$V_\nu(b) = \iint P_\nu(s) e^{-i(2\pi\nu \frac{\vec{b} \cdot \hat{s}}{c})} d\Omega \quad (2.9)$$

If we have two antennas, one at location  $\vec{r}_1$  and the other at location  $\vec{r}_2$  with respect to some origin, we can rewrite equation (2.9) as

$$V_\nu(\vec{r}_1, \vec{r}_2) = \iint P_\nu(s) e^{-i(2\pi\nu \frac{(\vec{r}_1 - \vec{r}_2) \cdot \hat{s}}{c})} d\Omega. \quad (2.10)$$

This is the complex visibility, the quantity that is obtained after the correlation process.

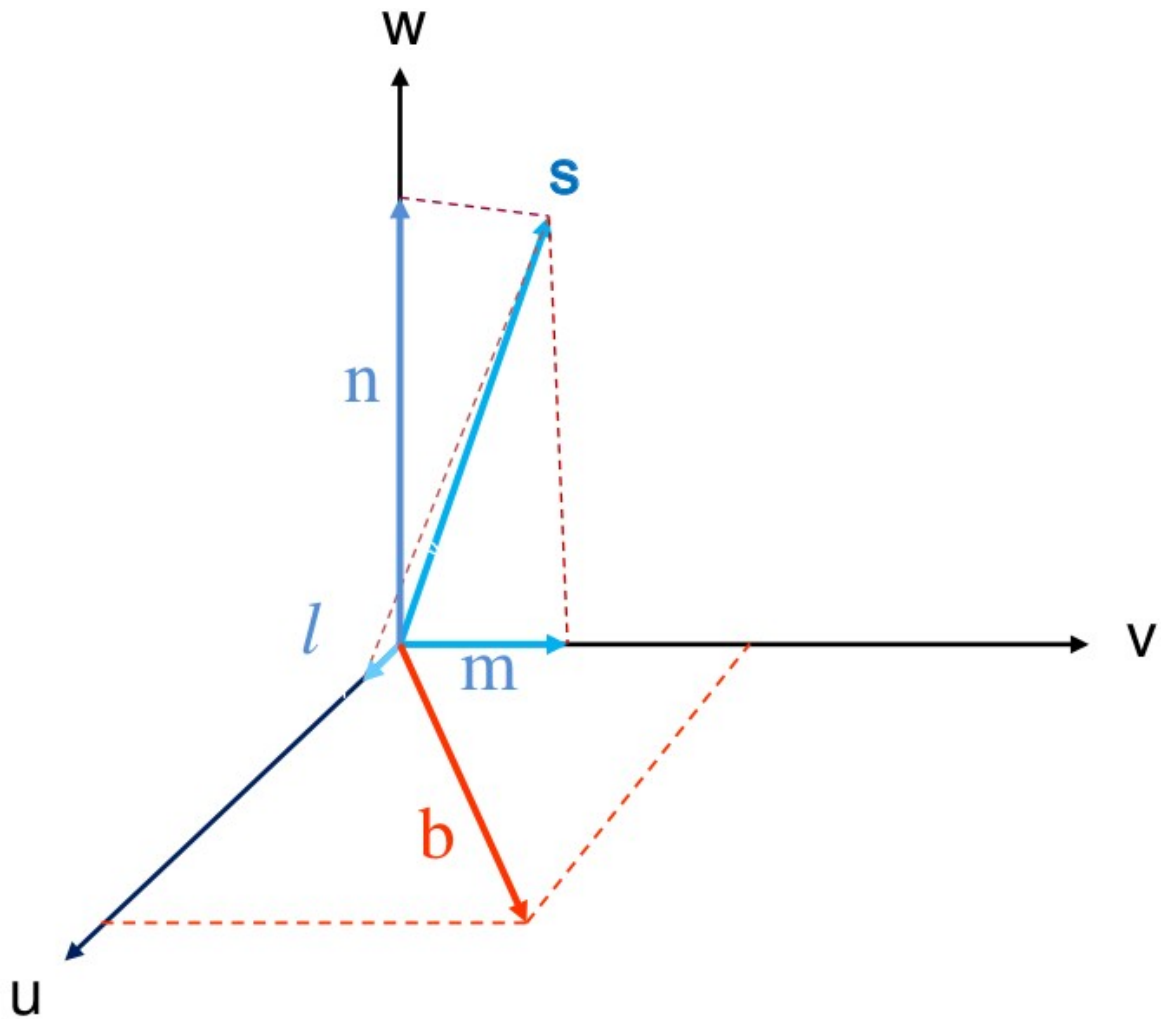


FIGURE 2.4: The  $(u,v,w)$  coordinate system along with vector  $\hat{s}$ . The projections of  $\hat{s}$  onto  $(u,v,w)$  are  $\vec{l}, \vec{m}, \vec{n}$  respectively. The vector  $\vec{b}$  represents the baseline vector.

Up to this point, everything we have derived is only viable for the case of a two antenna interferometer. As most interferometers, including the one used in this study, have more than two antennas, it is necessary to expand our derivation to account for them. To do this, it is convenient to define a coordinate system to

keep track of all the visibilities. We begin by assuming that all visibility data lie on a plane. This is a reasonable assumption for the small fields that are usually imaged by interferometers. We call this the (u,v) plane, and define a coordinate system (u,v,w) in which the w-axis is perpendicular to the (u,v) plane

$$\vec{b} = (\lambda u, \lambda v, \lambda w) = (\lambda u, \lambda v, 0) \quad (2.11)$$

where u,v and w are measured in units of wavelengths. We then take our unit vector in the direction of the source,  $\hat{s}$ , and decompose it onto our coordinate system

$$\hat{s} = (l, m, n) = l\hat{u} + m\hat{v} + n\hat{w}. \quad (2.12)$$

Putting this all together, we find that

$$\vec{b} = \vec{r}_1 - \vec{r}_2 = \lambda u\hat{u} + \lambda v\hat{v} \quad (2.13)$$

and

$$d\Omega = \frac{dldm}{\sqrt{1-l^2-m^2}} \quad (2.14)$$

where  $n = \sqrt{1-l^2-m^2}$ . Substituting equations (2.12),(2.13) and (2.14) back into equation (2.10), we arrive at

$$V_\nu(u, v) = \iint I_\nu^t(l, m) \frac{e^{-\frac{i2\pi\nu}{c}(\lambda u\hat{u} + \lambda v\hat{v}) \cdot (l\hat{u} + m\hat{v} + \sqrt{1-l^2-m^2}\hat{w})}}{\sqrt{1-l^2-m^2}} dldm \quad (2.15)$$

where we replace power for intensity, as  $P \propto I$ , and have labeled the true intensity  $I_\nu^t$ . Substituting  $\nu/c=1/\lambda$ , and defining the projected intensity  $I_\nu = I_\nu^t/\sqrt{1-l^2-m^2}$ , we can simplify equation (2.15) to

$$V_\nu(u, v) = \iint I_\nu(l, m) e^{-i2\pi(u l + v m)} dldm \quad (2.16)$$

This shows us that the visibilities  $V_\nu$  measured by an interferometer can be related to the intensity distribution  $I_\nu$  of the source via a Fourier Transform.

## 2.2 Observational Parameters

The 22 GHz H<sub>2</sub>O maser lines toward W3(OH) were observed during two different epochs on May 26, 2010 and October 30, 2010 as part of project BS198 (Principal Investigator A. Sarma). The observations each lasted 12 hours. For these observations, the field center was specified as being located at  $\alpha = 02^{\text{h}}27^{\text{m}}04^{\text{s}}.9$  and  $\delta = +61^\circ52'24''$ , where  $\alpha$  is the right ascension and  $\delta$  the declination. The frequency setup was chosen so that there would be eight baseband channels, each with a bandwidth of 4 MHz. Correlation was done with a total of 1024 spectral channels per baseband channel. As our objective is to measure the Zeeman Effect, we need both right and left circular polarizations. Each baseband is set to record one of these polarizations, and thus we have four pairs of basebands, one of each pair containing the left and right circular polarization measurements. In radio astronomy, frequency offsets are usually expressed in terms of velocity by the following equation

$$\frac{\Delta v}{c} = \frac{\nu - \nu_o}{\nu_o} \quad (2.17)$$

where  $\nu_o$  is the rest frequency of the water masers, which we set to  $\nu_o = 22.235.08$  MHz. So a 4 MHz bandwidth translates to a velocity of  $54 \text{ km s}^{-1}$ , and with 1024 channels per baseband we get a spectral resolution per channel of 3.9 kHz, which corresponds to a velocity spacing of  $0.05 \text{ km s}^{-1}$ .

## 2.3 Data Calibration

### 2.3.1 Calibration Assumptions

In § 2.1.3 we discussed how a radio interferometer measures visibilities. Actually, the observed visibilities differ from the true visibilities due to such causes as the

electronics in the signal path of the instrument and the atmosphere. We apply calibration techniques to extract the true visibilities from the observed. For this, we make the assumption that the true visibilities are linearly related to the observed visibilities for a pair of antennas through the equation

$$\tilde{V}_{ij}(t) = g_i(t)g_j^*(t)V_{ij}^t(t) + \epsilon_{ij}(t) \quad (2.18)$$

where  $\tilde{V}_{ij}$  is the observed visibilities,  $g_i$  and  $g_j^*$  are the gains of the  $i$ th and  $j$ th antennas, and  $\epsilon_{ij}$  describes the thermal noise. The antenna gains are complex numbers which represent the effects of the atmospheric conditions and the electronics. To recover the true visibilities,  $V_{ij}^t$ , a series of calibration steps must be implemented in order to calculate the appropriate gains.

### 2.3.2 Calibration Procedure

In this section, we will discuss the steps to a-priori data calibration in detail. This calibration will allow us to recover the true visibility from the observed visibility. A summary of each task can be found in Table 2.1.

After loading the data into AIPS using the task FITLD, we began the a-priori calibration, beginning with amplitude. We started by correcting errors in the amplitudes in the cross-correlation spectra using the task ACCOR. This is necessary as the VLBA correlator output is in terms of dimensionless correlation coefficients which need to be converted into the units of intensity used in radio astronomy, the Jansky (Jy). We then corrected for errors in amplitude due to environmental factors which can differ greatly at each antenna. To correct for these factors we used the task APCAL. APCAL reads information from the TY (temperature), GC (gain curve) and WX (weather) tables which contains the calibration information and generates an SN table containing this information. After each of these tasks, the task SNEDT was run to edit the SN tables they created, and then CLCAL to apply these SN tables to the highest CL table.

Next we corrected for phase errors created by the Earth rotating on its axis, and thus our antennas rotating along with it. This is known as the parallactic angle correction, and is done using AIPS task VLBPANG.

FITLD	Loads FITS files into AIPS.
APCAL	Corrects for voltage drifts, and generates SN table 1.
SNPLT	Displays data for SN table 1 for checking and flagging outliers.
CLCAL	Applies SN table 1 to CL table 1. Generates CL table 2.
APCAL	Applies calibration from TY (temperature), GC (gain curve) and WX (weather) tables. Generates SN table 2.
SNPLT	Displays data for SN table 2 for checking and flagging outliers.
CLCAL	Applies SN table 2 to CL table 2. Generates CL table 3.
VLBAPANG	Applies parallactic angle corrections to CL table 3. Generates CL table 4.
FRING	Corrects for instrumental Delay errors using the source calibrator DA193. Generates SN table 3.
SNPLT	Displays data for SN table 3 for checking and flagging outliers.
CLCAL	Applies SN table 3 to CL table 4. Generates CL table 5.
SETJY	Sets channel 257 to a velocity of $-49.1 \text{ km s}^{-1}$ .
CVEL	Compensates for the rotations of the Earth, and thus the antennas, around the Sun.
SPLIT	Applies highest CL and FG tables, splits out the data for our source of interest, W3OH, from the dataset. Creates a new dataset.
FRING	Corrects for instrumental Rate errors using our target source. Generates SN table 1 for the new dataset.
SNPLT	Displays data for SN table 1 for checking and flagging outliers.
CALIB	Used to put the peak maser source at the center of field 1. Then used in an iterative sequence along with IMAGR to self calibrate the data.

TABLE 2.1: AIPS data calibration steps for spectral line VLBA data.

Our next step was to run a process known as fringe-fitting to account for signal delay. In a radio interferometer, data from the source wavefront is combined from pairs of antennas (baselines). Since the VLBA antennas are separated by a substantial distance, the wavefront arrives at each antenna at a different time, which is known as delay. The correlator removes an estimate of this delay using a geometric model, but small errors present in the geometric model used by the VLBA correlator give residual delay errors, which are then corrected for using the task FRING using a strong calibrator source, DA193. In a radio interferometer, phase is the product of frequency and delay, and thus delay errors can be seen as the slope of the phase as a function of frequency. We used FRING to correct for this slope. This generated a new SN table, which was then edited and applied to the CL table.

We also had to account for the motion of the Earth, and thus the antennas, around the Sun. Because of this motion the center velocity of the spectrum will change with time. Because of this, we had to shift all spectra towards a given velocity. We used the task SETJY to assign the correct velocity for the source to the correct channel. This is set as the systematic velocity (see Appendix C) for the target source which is obtained from the literature; in our case, the observation was set up so that channel 257 would have velocity  $-49.1 \text{ km s}^{-1}$ . We then compensated for the observed effects of the rotation of the Earth around the Sun with the task CVEL.

Relative to the source, the antennas of the VLBA telescope all appear to be moving at different speeds. This causes the signal from each antenna to show a different Doppler shift, which shows as a drift in the phase as a function of time. As in the last step, the VLBA correlator applies a geometric model to remove an estimate of the fringe rate, but similar to the delay offsets, small errors in the model can create fringe rate offsets. To account for these we ran the task FRING a second time, this time using a specific strong channel for our target source. In our case, we used channel 339. This created a new SN table which was then edited.

As we had completed the a-priori data calibration, the next step was to use the source to run an iterative series of steps called self-calibration, which we will discuss in the next section.

### 2.3.3 Self-Calibration

Though we have completed a-priori calibration of the data, the calibration can still be improved. We did this through a process known as self-calibration. As we are dealing with strong maser sources, we can use them to improve calibration. We began self-calibration by creating a model with which to calibrate the data, such that

$$V_{ij}(t) = g_i(t)g_j^*(t)V_{ij}^{model} + \epsilon_{ij}(t) \quad (2.19)$$

where  $V_{ij}^{model}$  are the model visibilities. This model is usually an image of the peak intensity maser at its strongest channel. From here we ran an iterative process. Using the initial model, we did a least squares fit to the visibility data to find the value of the gains, and then applied these gains to the observed data. We then used this data to make a new model, and repeated the process. As this process was run, a gain in the signal to noise ratio (SNR) was observed with each iteration. The process was completed when subsequent steps no longer showed this effect, and the signal to noise ratio remained constant.

In practice, this process was done using the AIPS tasks CALIB and IMAGR. An initial run of CALIB set the strongest intensity source at the origin. We then used IMAGR to make an initial image of the strongest source at its peak channel. We ran the cleaning algorithm which is described in §2.4, and then used this cleaned image as our model in the next run of CALIB. CALIB then did a least squares fit to the model to determine the gains, applied them to the observed data, and we used this data to generate the next model in IMAGR. This process is not complete until a satisfactory model is produced (e.g., SNR becomes constant). The advantages of self-calibration on the intensity of the source data are plentiful, but they come at the cost that we sacrificed our absolute position information, and can only now discuss the positions of the masers relative to the point of the strongest maser.

## 2.4 Data Imaging

After the calibration steps described in Section 2.3 above, we have our best estimate of the true visibilities  $V_\nu$  in equation (2.16). An inverse Fourier transform

will then give the intensity distribution  $I_\nu$ . However, since we have only a finite number of baselines, the visibility function is only sampled for a limited number of points in the  $(u,v)$  plane. Therefore, the result of the inverse Fourier transform gives what is referred to in radio astronomy as a “dirty” image. That is, if we define a sampling function  $S(u,v) = 1$  for locations in the  $uv$  plane that correspond to sampled data points, and zero otherwise, then the inverse Fourier transform will produce the dirty image

$$I_\nu^D(l, m) = \iint V_\nu(u, v) S(u, v) e^{2\pi i(ul+vm)} dudv \quad (2.20)$$

This “dirty” image is the desired “clean” image convolved with a “dirty” beam. This can be seen easily if we define the “dirty” beam as

$$B(l, m) = \iint S(u, v) e^{2\pi i(ul+vm)} dudv. \quad (2.21)$$

The convolution theorem for Fourier transforms then gives

$$I_\nu^D(u, v) = I_\nu(u, v) \star B(l, m) \quad (2.22)$$

where  $\star$  denotes convolution, and  $I_\nu$  is the desired clean image. Therefore, to find the clean image we must first deconvolve the dirty beam from the dirty image.

We carried out the Fourier transform and deconvolution of the data with the AIPS task IMAGR. IMAGR employs a deconvolution procedure known as the Clark-Högbom algorithm (Högbom 1974, Clark 1980). This algorithm works by using the following steps:

- Locate the point of maximum intensity in the Fourier transformed dirty image and write it to a separate file called a point source model.
- Subtract from the image a quantity that is equal to the product of the dirty beam, the intensity at that point and the loop gain. The loop gain is a damping factor chosen by the user with range of values between 0 and 1. A larger loop gain makes for a cruder yet quicker deconvolution, whereas a lower gain value will give a slower but more thorough deconvolution. We used the standard value of 0.1.

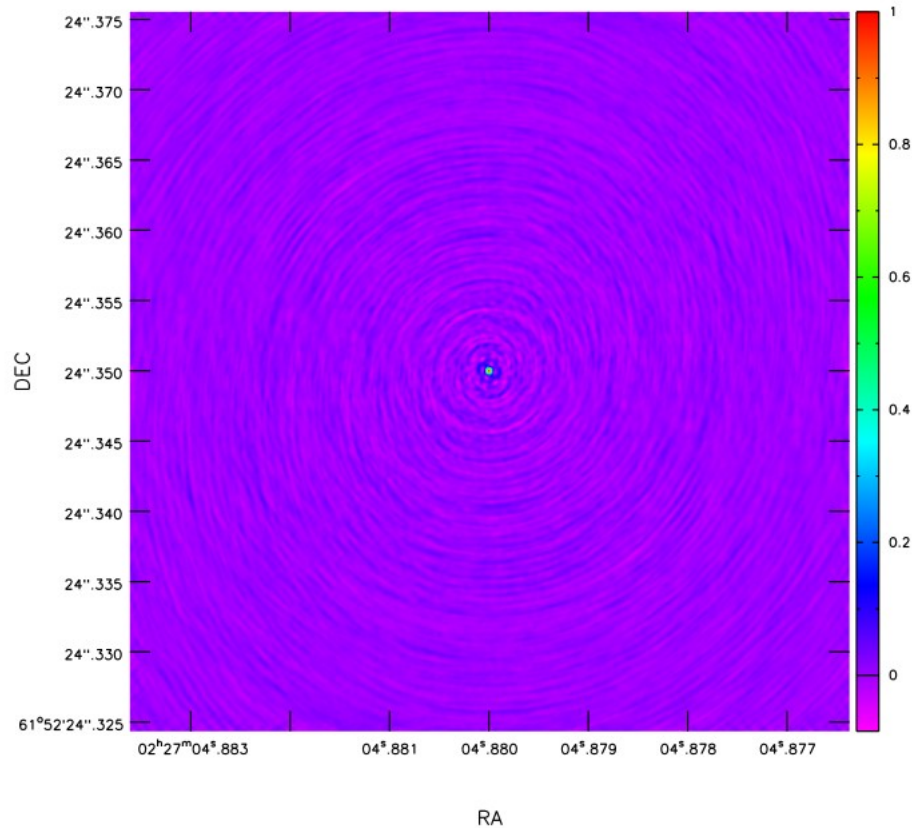


FIGURE 2.5: Plot of the dirty beam of the BS198B data. The peak intensity is normalized to 1 Jy beam<sup>-1</sup>.

- The algorithm then takes the remains of the dirty image, picks out the next highest intensity, and begins the process over again. This will continue until the algorithm has reached a user defined limit which is set to 3 times the rms of the noise limit in the data.
- Convolve the clean image with an idealized clean “synthesized” beam, which is found by fitting an elliptical Gaussian to the central lobe of the dirty beam.

This gives a basic description of the Clark-Högbom algorithm. The algorithm also has the ability to use major and minor cycles to speed up or refine the processes which will not be discussed here (e.g., see Clark 1980). In practice, IMAGR is run by bringing up the channels in a data cube one by one, putting CLEAN boxes around points of interest (masers), and manually continuing to iterate until only the dirty beam remains in the residual dirty image. This is done by taking the sources selected with the CLEAN boxes and convolving them with the synthesized

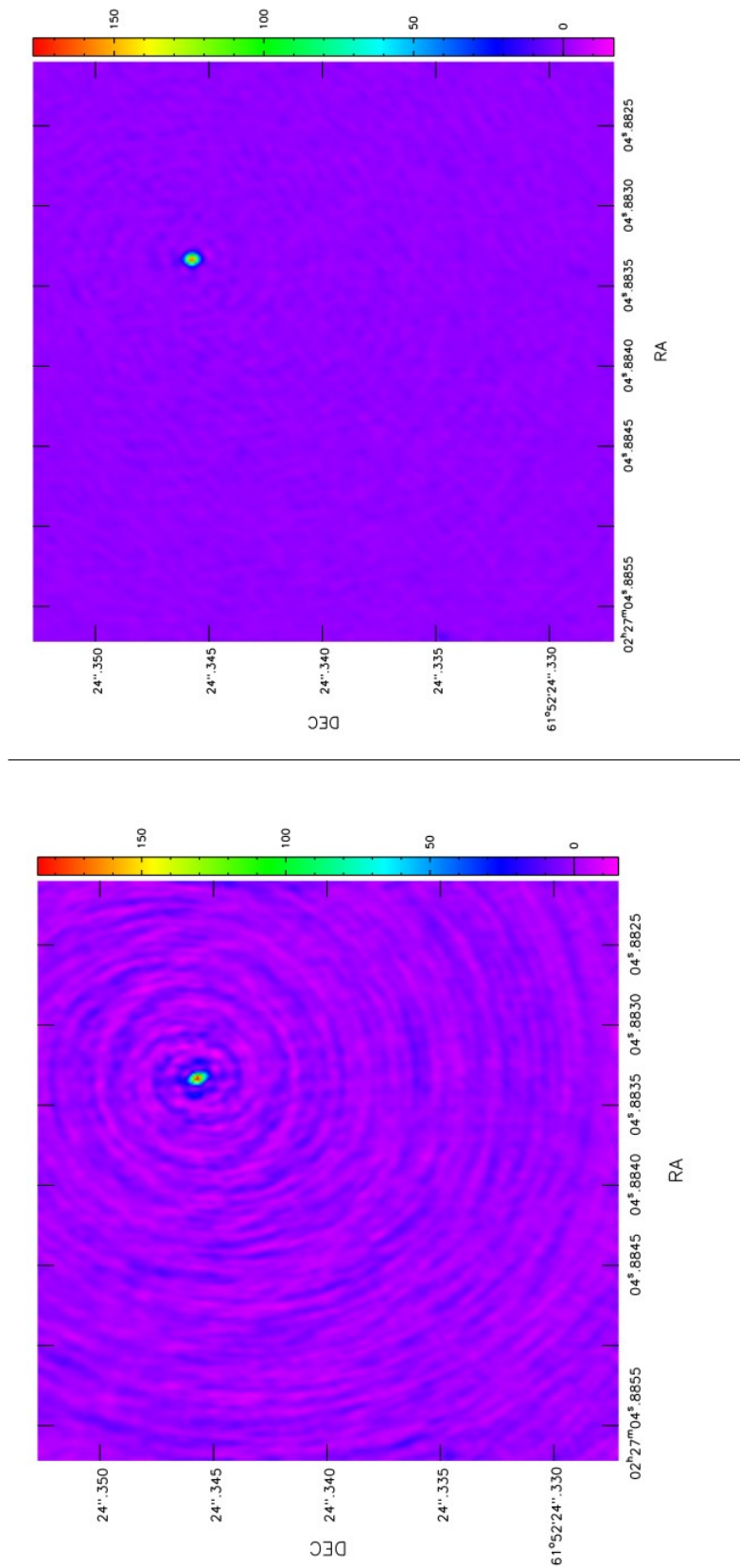


FIGURE 2.6: Representations of an example “dirty” image (left panel) and “clean” image (right panel). The images were taken from Field 2, channel 182 of BS198B. The circles around the maser in the dirty image are more prominent than those around the clean image.

“clean” beam. The synthesized beam is recorded with the beam FWHM, or full width half maximum, that corresponds to the two dimensional Gaussian measured at half the peak intensity, which also is the resolution of the interferometer obtained during the observations. In our case, we have a FWHM of  $0.39 \text{ mas} \times 0.36 \text{ mas}$ , where mas stands for milli-arcseconds, with a position angle of  $9.36^\circ$ . A sample clean and dirty image can be seen in Figure (2.6).

We used the IMAGR task to search for maser emission in a total of 66 fields, each of size  $25.6 \text{ mas} \times 25.6 \text{ mas}$ . We began by designating the search for the Stokes parameter I (see §2.5 for a discussion on the Stokes parameters used), the total intensity. Note that although Stokes I is conventionally defined as  $I = RCP + LCP$ , IMAGR expresses it as

$$I = \frac{RCP + LCP}{2} \quad (2.23)$$

where RCP and LCP are the right and left circular polarizations, and I denotes the Stokes I parameter. After completing the Stokes I imaging, we moved on to the Stokes V, which IMAGR expresses as

$$V = \frac{RCP - LCP}{2} \quad (2.24)$$

where  $V$  is the Stokes V parameter. Upon completing imaging for both data sets, we were ready to begin searching for the magnetic field strengths.

Masers were discovered by loading clean image fields into software by the name of Aipsview. Recall that we used 66  $25.6 \text{ mas} \times 25.6 \text{ mas}$  fields to image and clean the data set, and that this created image cubes  $25.6 \text{ mas} \times 25.6 \text{ mas} \times 1024$  channels in frequency, or the equivalent velocity. These image cubes were loaded into aipsview, and each cube was hunted channel by channel in search of bright points of intensity. One of the powers of Aipsview is the ability to click on a pixel and view a plot of the intensity of that pixel across all the channels in the image cube. For masers, this will appear as a near Gaussian profile like those that appear in Appendix A.

## 2.5 Measuring the Magnetic Field via the Zeeman Effect

When the correlator combines the data from each antenna, the result is a matrix of possible correlations

$$\begin{pmatrix} RR^* & RL^* \\ LR^* & LL^* \end{pmatrix}$$

This matrix is related to the Stokes parameters via

$$\begin{pmatrix} I + V & Q + iU \\ Q - iU & I - V \end{pmatrix}$$

where  $I$  is the total intensity,  $V$  is related to circular polarization, and  $Q$  and  $U$  are related to linear polarization. As our goal is to measure the Zeeman effect, we only concern ourselves with the Stokes  $I$  and Stokes  $V$  parameters in this thesis.

As discussed in §1.4, the Zeeman effect can be measured by taking the derivative of the Stokes  $I$  profile and fitting it to the Stokes  $V$  profile.

$$V = \frac{b}{2} \frac{dI}{d\nu} \tag{2.25}$$

Due to the leakage interaction between the RCP and LCP receivers and electronics into one another, the observed Stokes  $V$  profile may contain some residual of the Stokes  $I$  profile. In order to account for this, we fit  $V$  not only to the derivative of the  $I$  profile, but to the  $I$  profile itself as well. We do this fitting using a least squares method that is described by Troland & Heiles (1982)

$$V = aI + \frac{b}{2} \frac{dI}{d\nu} \tag{2.26}$$

where  $a$  and  $b$  are the parameters being fitted. As we expect the leakage to be small, the parameter  $a$  is expected to be small. We concern ourselves more with the  $b$  parameter, as it is this we use to extract our magnetic field values

$$b = zB\cos(\theta) = zB_{los} \quad (2.27)$$

where  $z$  is the Zeeman splitting factor,  $B$  the magnetic field,  $\theta$  the angle of the magnetic field to the line of sight, and  $B_{los}$  the line of sight magnetic field value. In §1.5 we discussed that the 22 GHz H<sub>2</sub>O maser line in the presence of a magnetic field is composed of 99 components. All 99 components were explicitly solved for by Nedoluha & Watson (1992), and they determined that the value of the Zeeman splitting factor to be 2.1 Hz mG<sup>-1</sup>, which is the value we will be using to extract  $B_{los}$  from our fitting parameter  $b$ .

# Chapter 3

## Results

In this chapter, we present the results of our observations for the Zeeman effect in H<sub>2</sub>O masers in W3(OH). In §3.1 we list our maser position data, the parameters obtained from Gaussian fits of the Stokes I profile, as well as map out our maser distributions. In §3.2 we present the magnetic field results obtained for each observation associated with these maser distributions.

### 3.1 Maser Distribution and Parameters

#### 3.1.1 BS198A

Observation BS198A detected 54 masers in the star forming region W3(OH). Our detection threshold for masers was set at 1 Jy, meaning that we only considered masers with intensity  $\geq 1$  Jy. This is a personally imposed limit, as the rms noise level in a line-free channel of a Stokes I image is only 7 mJy beam<sup>-1</sup>, and in principle we should be able to detect masers  $\geq 3\text{-}\sigma$  (21 mJy beam<sup>-1</sup>). We set the higher limit because dynamic range effects in channels featuring a particularly strong maser ( $>100$  Jy) would still show effects in nearby fields even after the deconvolution process. Since the Zeeman effect would not be detectable in masers with intensities  $< 1$  Jy anyway, the detection threshold we have set frees us up from differentiating between true masers lower than 1 Jy and residuals from the deconvolution of high intensity masers. In other words, our choice of setting our threshold at 1 Jy in no way interferes with the purpose of the study. This also

does not mean there are no masers with an intensity lower than the threshold, we will just make no claim to their detection.

Figure (3.1) shows the 3000 mas x 300 mas region where H<sub>2</sub>O masers were discovered in W3(OH) during observation BS198A. The (0,0) position in this figure is the location of the most intense maser, with an intensity of  $949.2 \pm 5.46$  Jy, and  $v_{LSR} = -48.45 \pm 0.01$  km s<sup>-1</sup>. A list of the masers detected in the BS198A observation can be seen in Table (3.1). The masers are listed in order of intensity ( $I_o$ ), from highest to lowest. Also given are the maser positions, in offsets ( $\Delta\alpha$  and  $\Delta\delta$ ), in mas, from the strongest intensity maser, the center velocity of the maser ( $v_{LSR}$ ) and the velocity width of the maser ( $\Delta v_{FWHM}$ ), along with their errors. The parameters  $v_{LSR}$ ,  $\Delta v_{FWHM}$ ,  $I_o$  were obtained by fitting gaussian profiles to the spectral line profiles of the masers using MATLAB. The spectral line profile is a plot of the intensity at the position of the maser as a function of velocity.

TABLE 3.1: Position and fitted parameters of the masers from observation BS198A. In the table,  $\Delta\alpha$  is the right ascension offset in milliarcseconds (mas) designated from the position (0,0) of the most intense maser and  $\Delta\delta$  the declination offset in mas designated from the position (0,0) of the most intense maser. The center velocity of the line  $v_{LSR}$ , velocity line width  $\Delta v_{FWHM}$ , and intensity  $I_o$  were obtained by Gaussian fits to the spectral line profiles of the masers, and are discussed in §3.1.1.

Group	Maser	$\Delta\alpha$ (mas)	$\Delta\delta$ (mas)	$v_{LSR}$ (km s <sup>-1</sup> )	$\Delta v_{FWHM}$ (km s <sup>-1</sup> )	Intensity $I_o$ (Jy)
Group 1	1	0	0	-48.45±0.01	1.21±0.01	949.50±5.46
	2	44.60	-107.6	-47.30±0.01	1.42±0.01	244.71±0.70
	3	-28.01	51.5	-48.51±0.01	0.67±0.01	105.43±0.57
	4	25.29	-4.3	-49.74±0.01	0.76±0.01	103.95±0.13
	5	24.94	-27.9	-48.05±0.01	0.98±0.01	49.42±0.11
	6	22.22	-28.0	-48.08±0.01	1.02±0.01	48.44±0.09
	7	41.42	-19.2	-51.59±0.01	1.18±0.01	47.79±0.23
	8	38.35	-80.8	-47.78±0.01	1.30±0.01	40.84±0.11
	9	-0.23	16.9	-48.19±0.01	0.77±0.01	37.62±0.08
	10	-0.05	-99.9	-50.26±0.01	1.22±0.01	35.65±0.22
	11	-0.06	16.2	-48.69±0.01	0.82±0.01	30.27±0.06
	12	41.19	-18.6	-50.52±0.01	1.19±0.01	25.91±0.06
	13	29.88	-38.6	-47.70±0.01	1.08±0.01	24.18±0.07
	14	51.12	-57.1	-48.07±0.01	1.01±0.01	22.38±0.12

TABLE 3.1: continued.

Group	Maser	$\Delta\alpha$ (mas)	$\Delta\delta$ (mas)	$v_{LSR}$ (km s <sup>-1</sup> )	$\Delta v_{FWHM}$ (km s <sup>-1</sup> )	Intensity $I_o$ (Jy)
	15	41.36	-28.8	-47.60±0.01	0.89±0.01	15.13±0.08
	16	39.75	-14.9	-50.93±0.01	1.73±0.01	15.12±0.05
	17	34.31	-14.8	-50.87±0.01	1.73±0.01	14.65±0.06
	18	40.04	-15.5	-50.45±0.01	1.81±0.03	11.65±0.14
	19	-209.66	-174.6	-45.72±0.01	0.95±0.01	11.56±0.08
	20	-39.21	77.6	-49.20±0.01	0.63±0.01	11.47±0.16
	21	15.74	-23.1	-48.22±0.01	0.91±0.01	11.25±0.05
	22	34.54	-15.5	-50.48±0.01	1.94±0.01	11.03±0.06
	23	21.19	-23.1	-48.20±0.01	0.87±0.01	10.61±0.03
	24	34.96	-92.2	-49.46±0.01	0.96±0.01	9.77±0.08
	25	-216.56	-189.6	-64.83±0.01	1.16±0.01	9.77±0.06
	26	30.29	-39.5	-47.92±0.01	0.88±0.01	8.43±0.08
	27	-203.82	-174.3	-46.34±0.01	1.14±0.01	7.61±0.07
	28	-209.20	-174.3	-46.32±0.01	1.21±0.02	7.26±0.12
	29	-217.13	-189.1	-64.32±0.01	1.15±0.01	6.47±0.06
	30	-200.02	-171.5	-51.36±0.01	1.36±0.01	5.71±0.05
	31	-215.98	-189.3	-62.33±0.01	1.19±0.02	4.42±0.05
	32	-217.42	-189.4	-66.07±0.01	0.96±0.02	2.42±0.03
	33	-223.04	-189.2	-66.36±0.02	1.13±0.06	1.26±0.05
Group 2	34	-637.25	63.1	-52.57±0.01	0.79±0.01	147.66±0.21
	35	-993.24	54.0	-52.55±0.01	0.92±0.01	99.28±0.15
	36	-995.70	50.8	-51.35±0.01	1.52±0.01	77.28±0.30
	37	-1004.24	54.0	-52.47±0.01	0.94±0.01	66.08±0.13
	38	-994.09	49.1	-50.31±0.01	1.22±0.01	59.11±0.22
	39	-1005.12	57.7	-55.60±0.01	1.12±0.01	32.70±0.20
	40	-993.05	48.0	-49.38±0.01	0.71±0.01	19.84±0.10
	41	-984.62	-53.3	-54.28±0.01	1.08±0.01	11.96±0.03
	42	-982.72	44.2	-48.97±0.01	0.98±0.01	11.81±0.12
	43	-636.50	62.9	-51.44±0.01	0.98±0.01	9.98±0.08
	44	-1007.98	55.0	-50.67±0.01	1.50±0.01	7.86±0.05
	45	-1007.12	54.9	-57.34±0.01	0.91±0.02	7.34±0.14
	46	-992.15	52.3	-56.10±0.01	1.34±0.01	5.16±0.07
	47	-996.20	-53.6	-55.09±0.01	0.97±0.03	5.02±0.12

TABLE 3.1: continued.

Group	Maser	$\Delta\alpha$ (mas)	$\Delta\delta$ (mas)	$v_{LSR}$ (km s <sup>-1</sup> )	$\Delta v_{FWHM}$ (km s <sup>-1</sup> )	Intensity $I_o$ (Jy)
	48	-990.66	-53.4	-55.24±0.01	1.04±0.01	4.89±0.06
	49	-987.49	-54.3	-55.19±0.01	0.82±0.01	4.39±0.07
	50	-636.33	64.5	-49.92±0.01	0.77±0.02	4.34±0.12
	51	-1005.16	53.0	-51.21±0.01	1.41±0.03	3.95±0.07
	52	-985.19	-53.5	-55.01±0.01	1.30±0.03	3.25±0.06
	53	-1009.82	56.8	-53.51±0.01	1.39±0.04	3.18±0.08
Group 3	54	-2053.53	-130.1	-45.53±0.01	0.61±0.01	15.26±0.10

The maser intensities span three orders of magnitude, ranging from a low of 1.26 Jy to a high of 949.50 Jy. We have found 22 masers in the 1-10 Jy range, 27 masers in the 11-100 Jy range, and 5 masers in the 101-1000 Jy range. The center velocities range from  $-45.72$  km s<sup>-1</sup> to  $-66.36$  km s<sup>-1</sup>, with an average value of  $-51.73$  km s<sup>-1</sup>. The FWHM line widths range from  $0.61$  km s<sup>-1</sup> to  $1.94$  km s<sup>-1</sup> with an average value of  $1.10$  km s<sup>-1</sup>.

### 3.1.2 BS198B

Observation BS198B detected 67 masers in the star forming region W3(OH). Figure (3.2) shows the 3000 mas x 500 mas region where H<sub>2</sub>O masers were discovered in W3(OH) during observation BS198B. The (0,0) position in this figure is the location of our most intense maser in this observation, with an intensity of  $1001.80 \pm 3.67$  Jy, and  $v_{LSR} = -53.87 \pm 0.01$  km s<sup>-1</sup>. A list of the masers discovered from the BS198B observation can be seen in Table (3.2). The masers are listed in order of intensity, from highest to lowest. Also given are the maser positions, given in the offsets,  $\Delta\alpha$  and  $\Delta\delta$  (in mas), from the strongest intensity maser, the center velocity of the maser ( $v_{LSR}$ ) and the velocity width of the maser ( $\Delta v_{FWHM}$ ), along with their errors given by the fit. The maser intensities span three orders of magnitude, ranging from a low of 1.44 Jy to a high of 1001.80 Jy. We found 17 masers in the 1-10 Jy range, 40 masers in the 11-100 Jy range, and

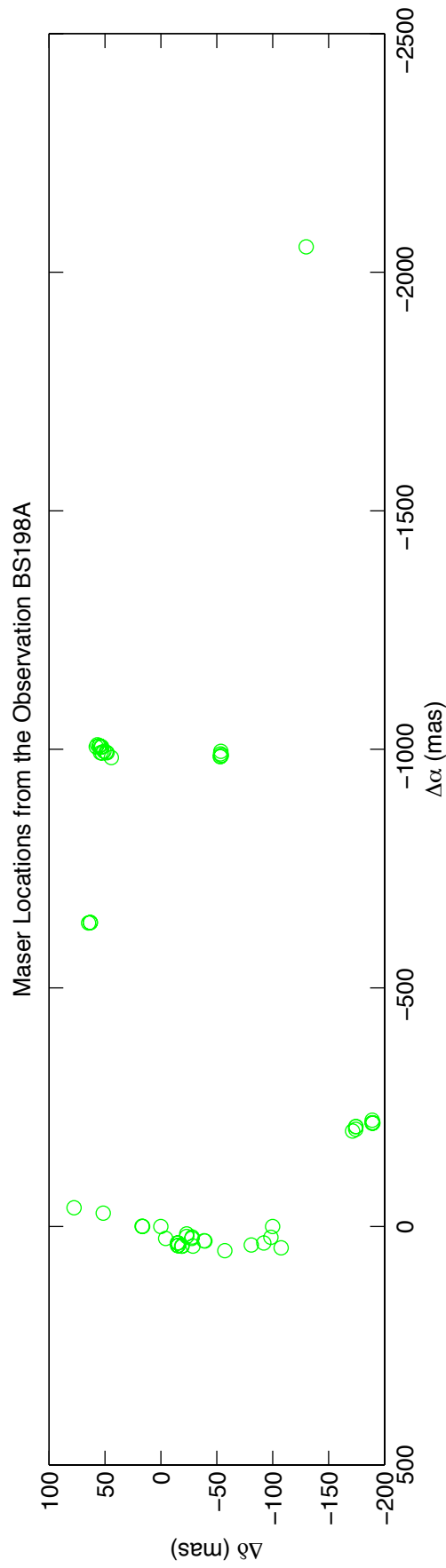


FIGURE 3.1: Image of the 3000 mas x 300 mas region in W3(OH) where all of the masers detected in observation BS198A were located. Maser locations are depicted as circles. The (0,0) position in the figure is the location of the highest intensity maser (Table 3.1 and § 2.4).  $\Delta\alpha$  gives offsets in Right Ascension and  $\Delta\delta$  gives offsets in Declination (both are in milliarcseconds, or mas) from this (0,0) position.

9 masers with an intensity greater than 100 Jy. The central velocities range from  $-48.57 \text{ km s}^{-1}$  to  $-70.43 \text{ km s}^{-1}$ , with an average value of  $-56.46 \text{ km s}^{-1}$ . The FWHM line widths range from  $0.65 \text{ km s}^{-1}$  to  $2.01 \text{ km s}^{-1}$  with an average value of  $1.09 \text{ km s}^{-1}$ .

TABLE 3.2: Position and fitted parameters of the masers from observation BS198B. In the table,  $\Delta\alpha$  is the right ascension offset in milliarcseconds (mas) designated from the position (0,0) of the most intense maser,  $\Delta\delta$  the declination offset in mas designated from the position (0,0) of the most intense maser, and  $v_{LSR}, \Delta v_{FWHM}$ , and  $I_o$  are explained in the caption to Table 3.1.

Group	Maser	$\Delta\alpha$ (mas)	$\Delta\delta$ (mas)	$v_{LSR}$ ( $\text{km s}^{-1}$ )	$\Delta v_{FWHM}$ ( $\text{km s}^{-1}$ )	Intensity $I_o$ (Jy)
Group 1	1	0	0	$-53.87 \pm 0.01$	$1.12 \pm 0.01$	$1001.80 \pm 3.67$
	2	22.39	-28.5	$-53.54 \pm 0.01$	$1.07 \pm 0.01$	$412.74 \pm 1.21$
	3	-24.45	51.6	$-53.85 \pm 0.01$	$0.84 \pm 0.01$	$262.13 \pm 0.52$
	4	25.40	-4.2	$-54.99 \pm 0.01$	$0.90 \pm 0.01$	$177.57 \pm 0.53$
	5	41.65	-18.9	$-56.99 \pm 0.01$	$1.02 \pm 0.01$	$140.00 \pm 0.10$
	6	-0.22	17.3	$-53.44 \pm 0.01$	$0.68 \pm 0.01$	$109.97 \pm 0.61$
	7	-0.17	16.7	$-53.75 \pm 0.01$	$0.89 \pm 0.01$	$97.42 \pm 0.13$
	8	44.77	-108.0	$-53.01 \pm 0.01$	$1.65 \pm 0.01$	$47.78 \pm 0.52$
	9	35.54	-83.5	$-53.87 \pm 0.01$	$1.07 \pm 0.01$	$47.41 \pm 0.19$
	10	42.73	-54.3	$-53.85 \pm 0.01$	$0.81 \pm 0.01$	$46.23 \pm 0.12$
	11	30.29	-6.4	$-53.95 \pm 0.01$	$1.24 \pm 0.01$	$43.36 \pm 0.10$
	12	15.73	-12.7	$-53.66 \pm 0.01$	$0.76 \pm 0.01$	$36.95 \pm 0.15$
	13	-199.33	-173.6	$-58.30 \pm 0.01$	$1.47 \pm 0.01$	$31.65 \pm 0.09$
	14	41.24	-17.8	$-55.56 \pm 0.01$	$1.60 \pm 0.02$	$28.16 \pm 0.27$
	15	30.23	-38.9	$-53.52 \pm 0.01$	$1.11 \pm 0.01$	$26.23 \pm 0.08$
	16	0.40	24.2	$-55.00 \pm 0.01$	$0.92 \pm 0.01$	$24.73 \pm 0.17$
	17	40.90	-16.6	$-55.13 \pm 0.01$	$1.81 \pm 0.01$	$23.24 \pm 0.14$
	18	44.52	-27.8	$-57.64 \pm 0.01$	$1.27 \pm 0.01$	$21.82 \pm 0.14$
	19	39.98	-14.4	$-56.54 \pm 0.01$	$1.64 \pm 0.01$	$20.49 \pm 0.09$
	20	30.75	-40.5	$-53.60 \pm 0.01$	$1.12 \pm 0.01$	$20.18 \pm 0.11$
	21	27.03	-98.4	$-53.19 \pm 0.01$	$1.33 \pm 0.01$	$20.12 \pm 0.09$
	22	21.59	-98.4	$-53.20 \pm 0.01$	$1.40 \pm 0.01$	$19.84 \pm 0.08$
	23	-11.59	45.7	$-53.41 \pm 0.01$	$0.70 \pm 0.01$	$18.45 \pm 0.10$
	24	40.44	-15.3	$-55.30 \pm 0.01$	$1.35 \pm 0.01$	$16.51 \pm 0.16$
	25	-34.49	64.3	$-53.93 \pm 0.01$	$1.02 \pm 0.01$	$15.78 \pm 0.06$

TABLE 3.2: continued.

Group	Maser	$\Delta\alpha$ (mas)	$\Delta\delta$ (mas)	$v_{LSR}$ (km s <sup>-1</sup> )	$\Delta v_{FWHM}$ (km s <sup>-1</sup> )	Intensity $I_o$ (Jy)
	26	-40.01	47.5	-53.88±0.01	1.13±0.01	15.09±0.09
	27	14.76	-29.1	-53.89±0.01	0.87±0.01	14.22±0.10
	28	30.75	-29.1	-54.00±0.01	0.99±0.01	14.17±0.06
	29	-31.91	54.0	-53.88±0.01	0.90±0.01	13.83±0.06
	30	-0.06	-100.5	-55.44±0.01	1.13±0.01	13.73±0.11
	31	-37.37	46.1	-53.98±0.01	1.00±0.01	12.83±0.07
	32	-222.00	-190.3	-70.43±0.01	1.11±0.01	12.32±0.09
	33	-35.07	52.8	-53.89±0.01	1.05±0.01	11.57±0.09
	34	-220.91	-190.2	-67.97±0.01	0.97±0.01	11.37±0.06
	35	-5.11	99.4	-53.85±0.01	1.01±0.01	10.24±0.04
	36	-221.43	-190.5	-69.45±0.01	1.45±0.02	10.10±0.10
	37	21.30	-55.9	-54.98±0.01	0.92±0.01	8.69±0.07
	38	36.97	-92.7	-53.04±0.01	1.10±0.02	8.55±0.10
	39	-199.05	-172.5	-56.51±0.01	1.81±0.02	7.38±0.08
	40	-198.82	-173.6	-57.41±0.02	2.01±0.05	4.71±0.11
	41	-226.43	-190.8	-67.27±0.02	1.00±0.06	2.35±0.13
	42	-229.30	-190.5	-66.46±0.03	1.23±0.09	1.78±0.11
Group 2	43	-1004.47	54.3	-57.68±0.01	0.84±0.01	283.77±0.19
	44	-980.37	34.2	-57.83±0.01	0.88±0.01	145.06±0.12
	45	-991.66	-54.3	-60.99±0.01	0.85±0.01	49.40±0.09
	46	-993.92	49.8	-57.84±0.01	0.88±0.01	49.22±0.11
	47	-980.71	34.9	-57.68±0.01	1.30±0.01	36.87±0.08
	48	-985.48	-57.6	-60.14±0.01	0.95±0.01	32.80±0.15
	49	-1004.53	62.7	-57.82±0.01	0.89±0.01	22.94±0.04
	50	-1009.93	57.9	-58.98±0.01	1.17±0.01	20.13±0.10
	51	-636.62	64.0	-57.31±0.01	1.06±0.01	17.26±0.05
	52	-1007.81	56.3	-62.51±0.01	1.17±0.01	16.69±0.17
	53	-1002.42	56.2	-62.62±0.01	1.18±0.02	16.32±0.19
	54	-1054.42	-38.7	-56.05±0.01	1.46±0.01	12.45±0.06
	55	-981.86	44.7	-55.10±0.01	1.25±0.01	11.21±0.09
	56	-869.08	0.0	-48.57±0.01	0.96±0.01	11.15±0.04
	57	-1002.77	56.2	-56.33±0.01	1.08±0.02	8.44±0.14
	58	-1001.85	54.3	-55.18±0.01	0.80±0.01	7.58±0.06

TABLE 3.2: continued.

Group	Maser	$\Delta\alpha$ (mas)	$\Delta\delta$ (mas)	$v_{LSR}$ (km s <sup>-1</sup> )	$\Delta v_{FWHM}$ (km s <sup>-1</sup> )	Intensity $I_o$ (Jy)
	59	-997.59	49.7	-55.45±0.01	0.76±0.01	6.43±0.08
	60	-631.62	64.0	-56.10±0.01	0.80±0.01	5.71±0.06
	61	-874.08	0.0	-52.39±0.01	0.76±0.02	3.41±0.07
	62	-991.36	-53.5	-60.68±0.01	1.05±0.01	2.89±0.03
	63	-877.69	0.0	-52.91±0.01	0.85±0.02	2.58±0.04
	64	-635.53	64.0	-55.84±0.01	0.79±0.02	2.18±0.06
Group 3	65	-2054.11	-130.1	-50.95±0.01	0.65±0.01	10.82±0.03
	66	-2048.21	-315.2	-54.32±0.01	1.38±0.01	7.01±0.03
	67	-2088.80	-321.1	-51.76±0.01	0.90±0.03	2.11±0.05

Figure (3.3) is a map of the 3000 mas x 500 mas region in W3(OH) where H<sub>2</sub>O masers have been detected in our two observations.. The masers span over 2000 mas east to west and about 500 mas north to south. The origin (0,0) position is marked with the most intense maser discovered in BS198A and BS198B, with intensities  $I_A = 949.50$  Jy and  $I_B = 1001.80$  Jy, and  $v_{lsrA} = -48.45$  km s<sup>-1</sup> and  $v_{lsrB} = -53.87$  km s<sup>-1</sup>, where the subscripts A and B denote the observation. We determined these to be the same maser through visual inspection by comparing the position of masers in other fields between the two observations and finding many to fall in the same position relative to this one. A discussion of the change in center velocity can be seen in §4.4.

In all studies the masers appear to be positioned in 3 separate groups based on location. Group 1 contains the 33 masers discovered around the strongest maser in BS198A, and the 42 masers discovered around the strongest maser in BS198B. This group contains most of the strong masers observed, as well as the strongest source. Most of the masers in this group are arranged along a north-south line, with little variation in position from east to west. Group 2 is comprised of the 20 masers in BS198A and 22 masers in BS198B which are centered at 750 mas to the west of the origin position (west is to the right in an astronomical image). This group contains a larger east to west variance while being a bit more clumped together in respect to north and south. Group 3 is a group of masers centered around 2100

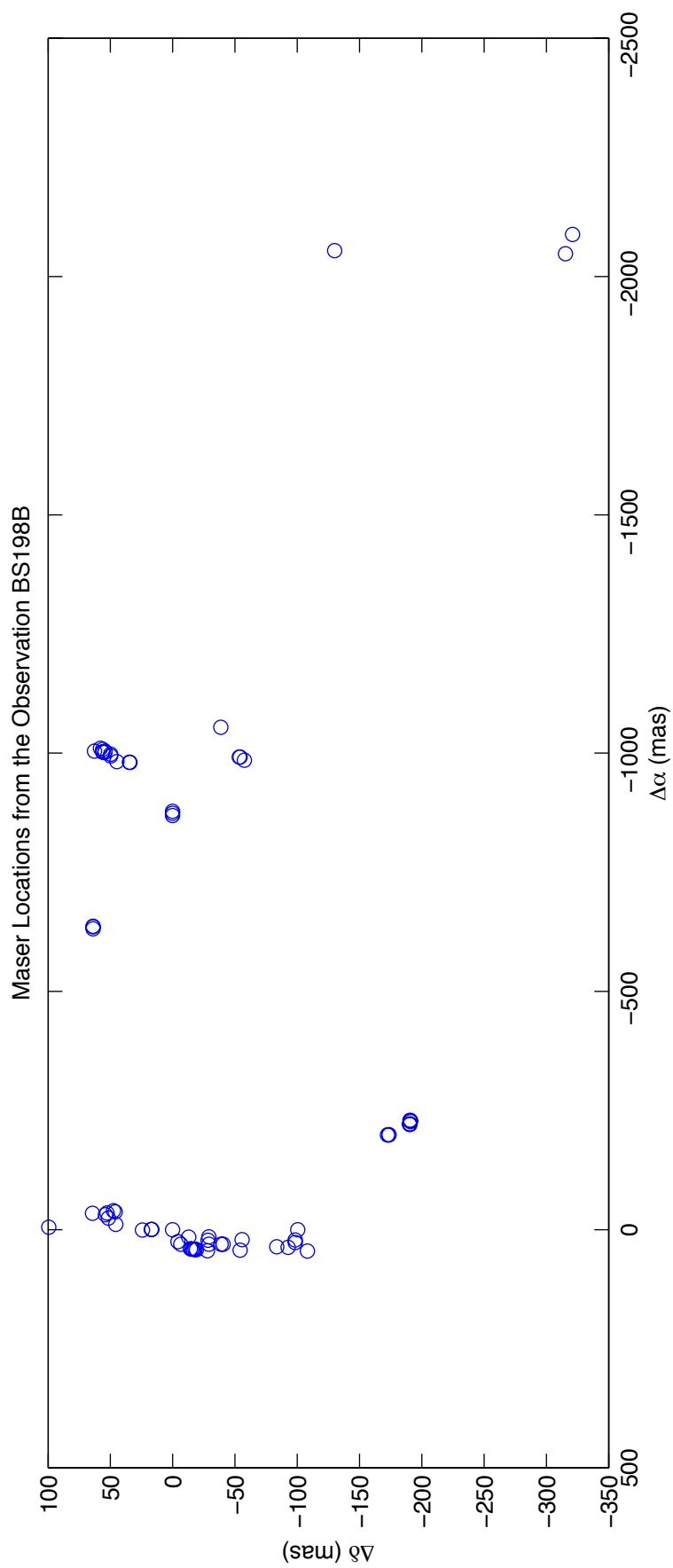


FIGURE 3.2: Image of the 3000 mas x 500 mas region in W3(OH) where all of the masers detected in observation BS198B were located. Maser locations are depicted as circles. The symbols  $\Delta\alpha$  and  $\Delta\delta$  as well as the origin position are explained in the caption to Figure 3.1

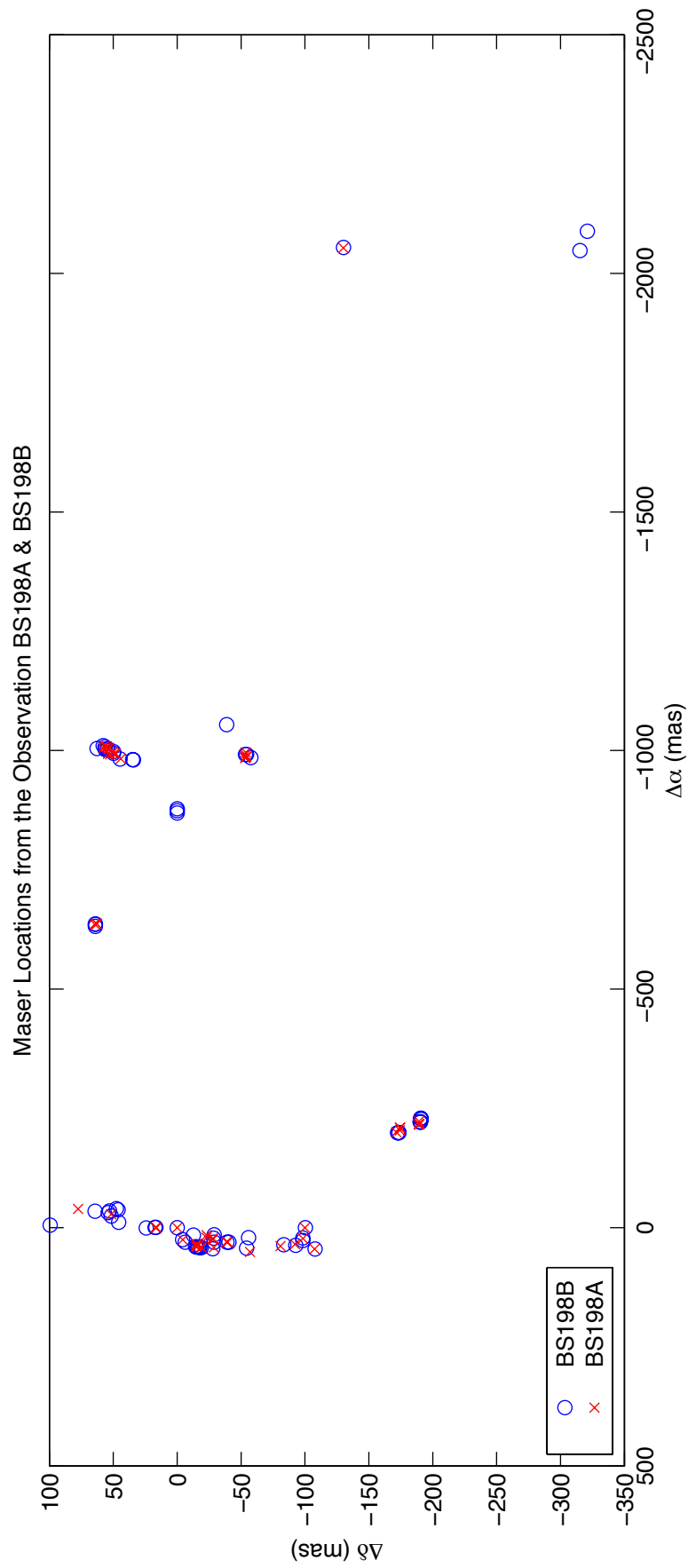


FIGURE 3.3: Image of the 3000 mas x 500 mas region in W3(OH) where all of the masers detected in observation BS198A and BS198B were located, marked with red and blue, respectively. The symbols  $\Delta\alpha$  and  $\Delta\delta$  as well as the origin position are explained in the caption to Figure 3.1

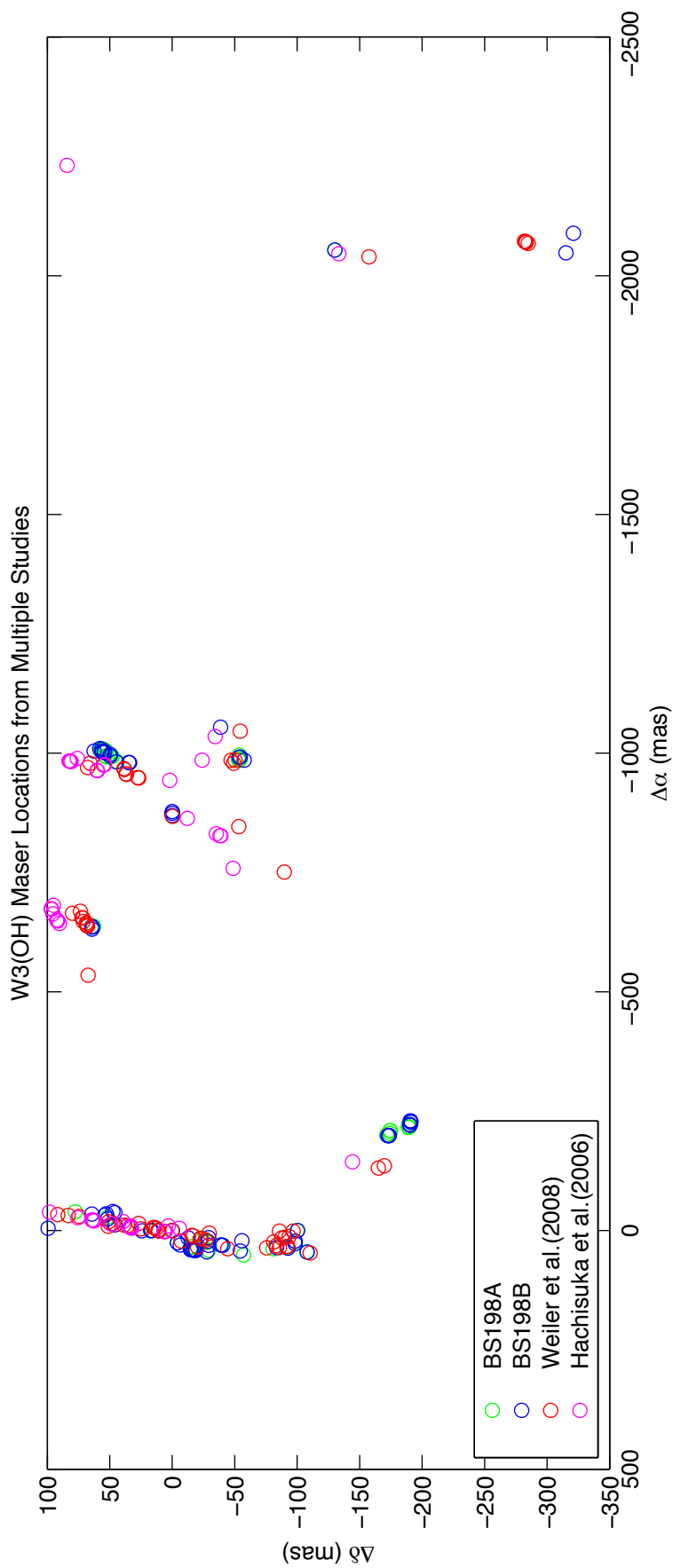


FIGURE 3.4: Image of the 3000 mas x 500 mas region in W3(OH) where all of the masers detected in observation BS198A (green circles) & BS198B (blue circles) were located, along with the masers discovered by Hachisuka et al. (2006) (cyan circles) and Weiler et al. (2009) (red circles).

mas west of the origin position, containing a single maser from BS198A and 3 masers from BS198B. In Figure (3.4), we see the 3 groups coincide well with the observations of Weiler et al. (2009) and Hachisuka et al. (2006), with our masers lining up very well with the previous observations. A close look at the masers in Group 1 in Figure (3.4) will show that many of our masers line up slightly to the left of those discovered in previous observations. This is in agreement with the direction in which these masers are moving in the plane of the sky, and will be discussed in greater detail in section (4.3).

## 3.2 Magnetic Field Values

As discussed in §2.5, we measure the Zeeman effect using a least squares fitting method to fit the derivative of the Stokes I profile to the Stokes V profile, as well as the Stokes I profile itself. We did this fit using equation (2.26), which we will repeat here.

$$V = aI + \frac{b}{2} \frac{dI}{d\nu} \quad (3.1)$$

The least squares fitting routine allowed us to solve for the values  $a$  and  $b$ . Recall that the parameter  $a$  is due to the leakage between the RCP and LCP and is predicted to be a small effect. In all cases, the value of  $a$  was  $\sim 10^{-4}$  or smaller. The fit parameter  $b$  lets us determine the line of sight magnetic field strength ( $B_{los}$ ) using  $b = zB_{los}$ , where the Zeeman splitting parameter  $z=2.1$  Hz mG $^{-1}$  (Nedoluha et al. 1992). To be considered a significant detection of magnetic field strengths, the ratio of the field to the error in the fitted field ( $b/\sigma_b$ ) must be greater than or equal to three. Three masers from BS198A and twelve masers from BS198B satisfied this criterion. The values of  $b$  and  $B_{los}$  for these 15 masers are presented in Table (3.3). A second test for a significant detection is to verify by visual inspection that the Stokes  $V$  profile looks like the derivative of the Stokes  $I$  profile. While this is largely true for all the masers listed in Table 3.3, residual sidelobes from strong masers in both observations introduce significant noise into or near one or both ends of the Stokes  $V$  profile. To the most conservative eye, only the  $V$  profiles of the strongest maser in each epoch are not affected by this problem. Therefore, we will consider these two detections (in the strongest maser in each epoch) to be fully satisfactory; plots of the Stokes  $I$  and  $V$  profiles, together

---

with the scaled derivative of  $I$ , are shown in Figures 3.5 and 3.6. The other 13 detections may be considered tentative pending sophisticated attempts to improve the calibration to scale down noise residuals from strong masers; their Stokes  $I$ ,  $V$ , and scaled derivative profiles are shown in Appendix D (for BS198A) and E (for BS198B) respectively. The magnetic field strength for our most intense maser in BS198A yields a value of  $-28.85$  mG, and for BS198B a value of  $-43.39$  mG. Other masers yield values with magnitudes ranging between 26.73 mG and 239.57 mG for BS198A, and 6.56 mG and 406.70 for BS198B. These results are discussed further in §4.4.

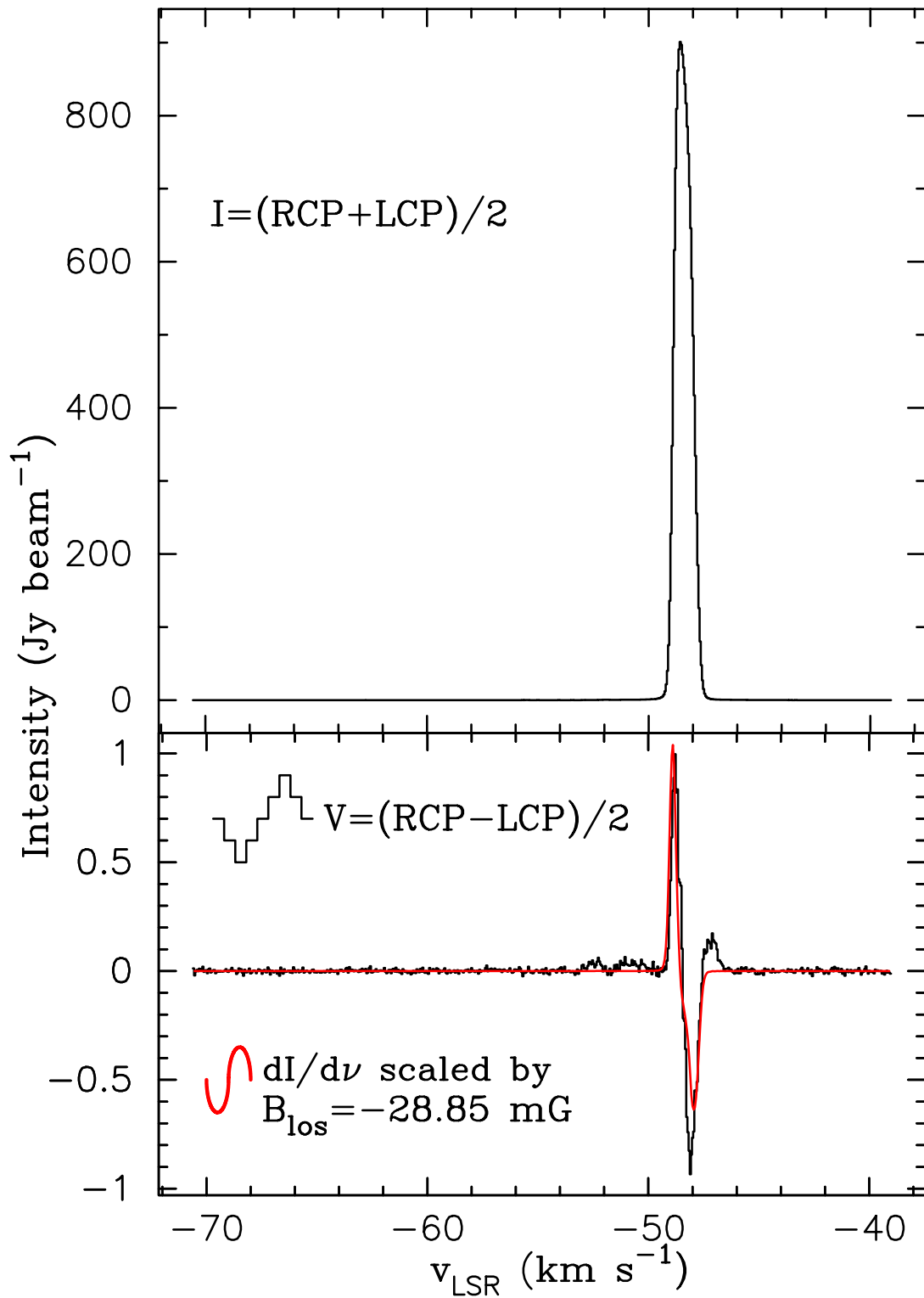


FIGURE 3.5: Stokes I (top) and V (bottom) profiles of maser 1 from observation BS198A (as numbered in Table 3.1). The curve superposed on V in the lower frame is the derivative of I scaled by the fitted value of  $B_{\text{los}} = -28.85$  mG.

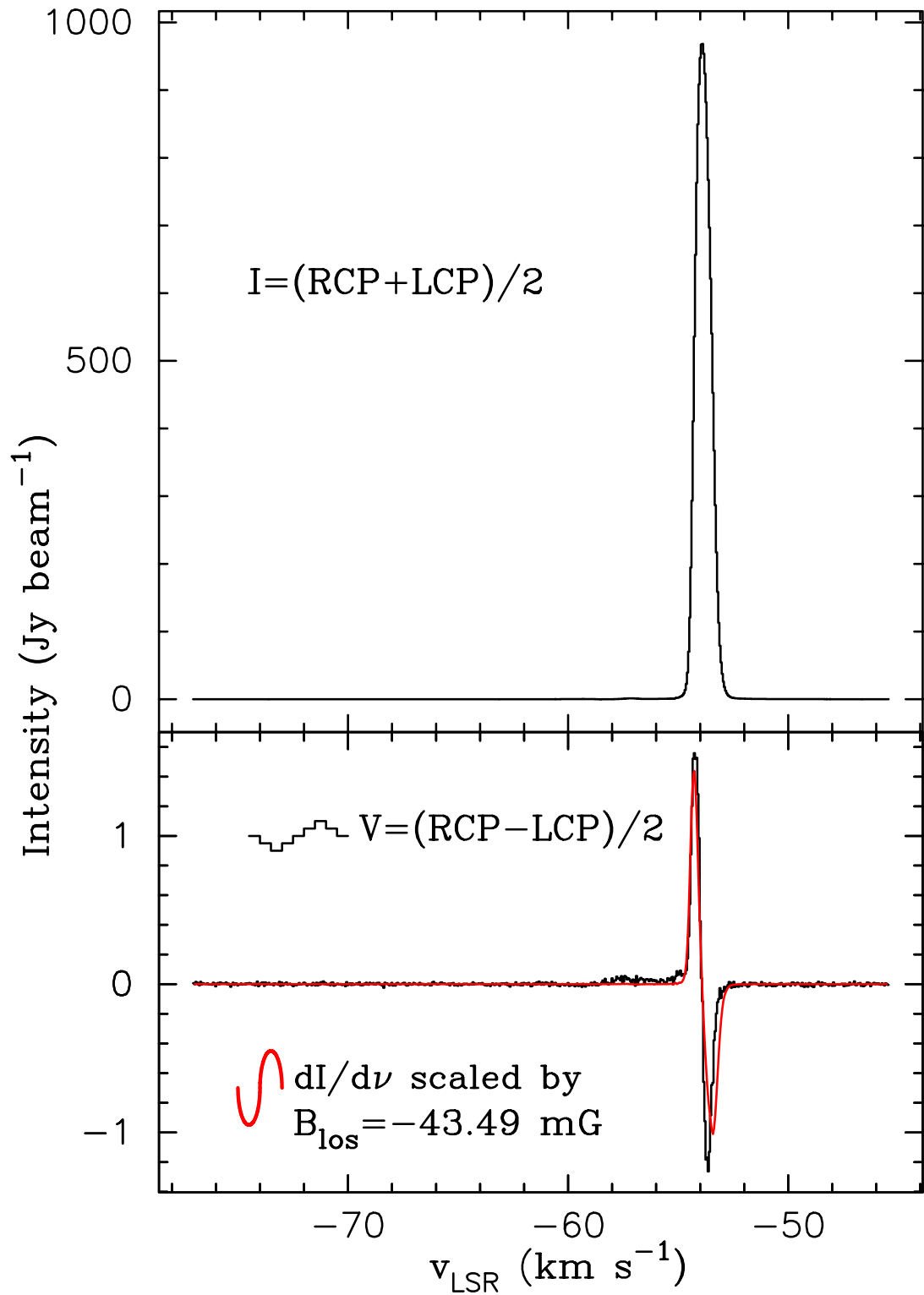


FIGURE 3.6: Stokes I (top) and V (bottom) profiles of maser 1 from observation BS198B (as numbered in Table 3.2). The curve superposed on V in the lower frame is the derivative of I scaled by the fitted value of  $B_{\text{los}} = -43.49 \text{ mG}$ .

Magnetic Field Parameters						
Maser	$\Delta\alpha$ (mas)	$\Delta\delta$ (mas)	Intensity $I_o$ (Jy)	Fit Parameter b (Hz)	$B_{los}$ (mG)	SNR <sup>1</sup>
BS198A						
1	0	0	949.50±5.46	-60.59±3.78	-28.85±1.80	16
2	44.60	-107.6	244.71±0.70	-56.14±3.62	-26.73±1.72	15
13	29.88	-38.6	24.18±0.07	-503.10±35.28	-239.57±16.80	14
BS198B						
1	0	0	1001.80±3.67	-91.33±5.53	-43.49±2.63	16
4	25.4	-4.2	177.57±0.53	46.14±4.57	21.97±2.18	10
5	41.65	-18.9	140.00±0.17	99.79±6.86	47.52±3.27	14
9	35.54	-83.5	47.41±0.19	35.13±8.54	16.73±4.07	4
10	42.73	-54.3	46.23±0.12	86.62±8.08	41.25±3.85	10
11	30.29	-6.4	43.36±0.10	-464.74±30.26	-221.30±14.41	15
15	30.23	-38.9	26.23±0.08	472.66±33.57	225.08±15.98	14
25	-34.49	64.3	15.78±0.06	-854.06±57.13	-406.70±27.20	14
33	-37.05	52.8	11.57±0.09	-237.44±29.71	-113.07±14.15	7
43	-1004.47	54.3	283.77±0.19	13.78±1.39	6.56±0.66	9
44	-980.37	34.2	145.06±0.12	95.84±7.21	45.64±3.43	13
45	-991.66	-130.31	49.40±0.09	-130.31±14.89	-62.05±7.09	8

TABLE 3.3: Table showing the magnetic field fit parameters from observation BS198A and BS198B. Maser 1 in both observations show satisfactory detection as per our criteria. All other masers are obstructed by noise from strong masers affecting the V profile, and must await confirmation from more careful calibration. <sup>1</sup>SNR is the “signal-to-noise” ratio, found by taking the ratio of  $B_{los}$  with the error found from our formal fit. IVD diagrams for maser 1 in both observations can be seen in Figures (3.5) and (3.6), respectively. IVD diagrams for all others can be viewed in Appendices D and E.

# Chapter 4

## Discussion

In this chapter, we begin with a discussion of the source of our observation in §4.1. We then move on to discuss flaring in §4.2, followed by the morphology of the observed masers in §4.3. Finally, we will conclude with a discussion of our magnetic field values, and give a comparison of the magnetic field strengths between the two epochs in §4.4.

### 4.1 W3(OH) and the Turner-Welch Object

W3 is an enormous region containing interstellar gas, dust and stars. It is often referred to as a “star formation factory” due to the number of young stellar objects that can be observed within. The W3 region is a molecular cloud located in the Perseus arm of the Milky Way Galaxy, at a distance of 2.04 kpc (Hachisuka et al. 2006). Its location has a Galactic latitude of  $b = 1^\circ.2$  and a Galactic longitude of  $l = 133^\circ.7$ , where Galactic Latitude ( $b$ ) is defined from our location with  $b = 0$  being the mid-plane of the Galactic disk, and Galactic Longitude is defined by  $l = 0$  pointing toward the center of the Milky Way Galaxy, while  $l = 180^\circ$  points to the “Galactic anti-center”, the direction opposite that of the Galactic center. The location of the Sun and the W3 region in the Milky Way Galaxy are shown in Figure (4.1).

The W3 region has multiple prominent sites of ongoing stellar formation, two of which are W3 Main and W3(OH). The W3(OH) region is located about  $15'$  south-east of the region W3 Main, a continuum image of which can be seen in the upper

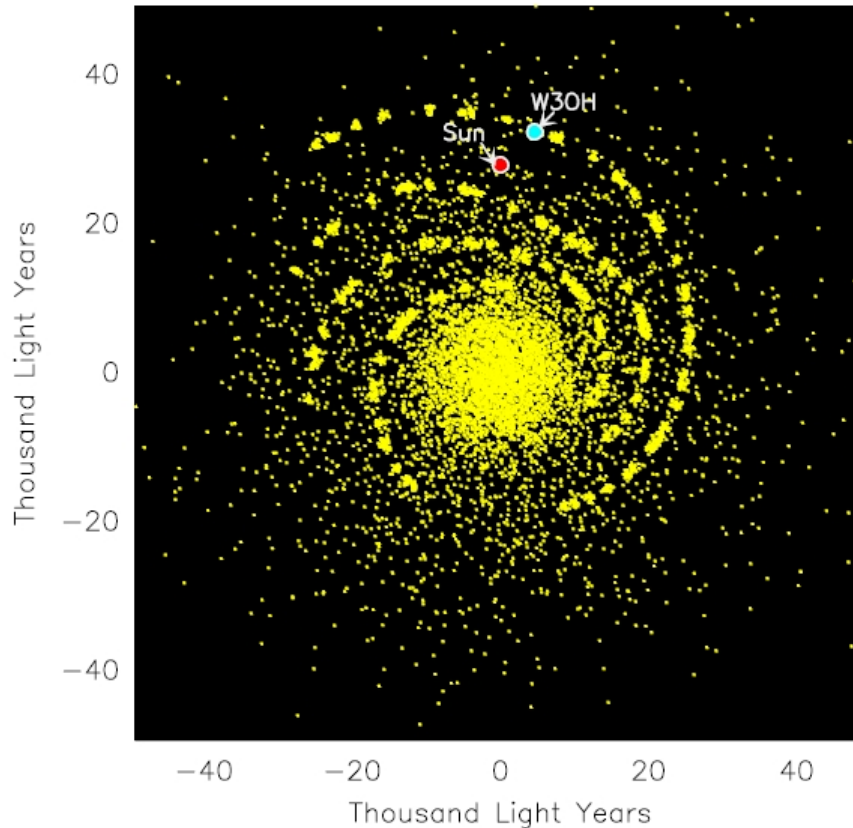


FIGURE 4.1: Image showing the location of the Sun and the W3 region in the Milky Way Galaxy. This image is courtesy of the Max Planck Society.

panel of Figure (4.2). W3(OH) is an ultra compact (UC) HII region (Dreher et al. 1981), a structure usually found around young high mass forming stars (see §1.1). An HII region is one which contains an abundance of ionized Hydrogen. This can be seen in the lower right of the image. The name W3(OH) comes from the OH masers associated with this HII region (Fish et al. 2006).

Located  $6''$  to the east (in an astronomical image, east is to the left) of W3(OH) is the Turner-Welch, or “TW”, Object (Turner et al. 1984). Helmich et al. (1997) found that the TW Object is a warm clump of gas with temperature  $\sim 200$  K by observing transitions between several levels of a single species of molecule, as well as the emission lines of several molecules (this is standard procedure as a means to discover the parameters of an astronomical source). Through observations of continuum emission at 112 GHz and 225 GHz, Wyrowski et al. (1997) saw prominent detection of the TW Object at 225 GHz, indicating the presence of hot dust. Stecklum et al. (2002) observed this region at mid-infrared and were unable to detect anything from the TW Object, indicating very high extinction rates due to

dust toward the source. These observations show evidence that the TW Object is a region of star formation in very early stages of stellar evolution, an earlier stage than the HII region to the west. It is toward the TW Object that the H<sub>2</sub>O masers we have observed are located. Though the TW Object is frequently referred to as W3(H<sub>2</sub>O) in the literature, we will continue to call it W3(OH) to avoid confusion with another prominent source of H<sub>2</sub>O maser emission toward W3 Main (Sarma et al. 2001).

## 4.2 Flaring Event

Throughout this thesis we have made reference to one of our epochs as a flaring event. Flaring events occur in the masers of star forming regions, and are defined by an increase in intensity to many of the masers in the region, along with the creation of more masers. There are several possible reasons given in the literature as a possible cause of a flaring event, the one most accepted for collisionally excited masers is that of two interacting masing clouds. In this model, photons from the initial masing cloud come into contact with another cloud along the line of sight, effectively increasing the path length, and thus adding to the intensity (Boboltz et al. 1998). We believe that we observed a flaring event in observation BS198B as it meets the two criteria discussed above. We observed increases in the intensities of masers and 13 additional masers in this observation, indicating increased activity. Table (4.1) shows a comparison of maser intensity between the two observations for masers which are spatially coincident (with the exception of small shifts due to their motion along the plane of the sky).

## 4.3 H<sub>2</sub>O Maser Distribution in the TW Object

In §1.3 we discussed the pumping of H<sub>2</sub>O masers through collisional excitation of the molecules. Appropriate conditions for this collisional excitation can be found in outflows from young forming stellar regions. These outflows propagate shock fronts through the ambient material along their paths, setting the stage for collisional excitation of the H<sub>2</sub>O molecules which results in masing transitions, discussed in §1.3-1.5. A result of this is that H<sub>2</sub>O masers are useful in tracking these outflows. Observations of these outflows would depend on their orientation

BS198A — BS198B									
Maser	$\Delta\alpha$ (mas)	$\Delta\delta$ (mas)	$I_a$ (Jy)	Maser	$\Delta\alpha$ (mas)	$\Delta\delta$ (mas)	$I_b$ (Jy)		
Group 1									
1	0	0	949.50±5.46	1	0	0	1001.80±3.67		
2	44.60	-107.6	244.71±0.70	8	44.77	-108.0	47.78±0.52		
3	-28.01	51.5	105.43±0.57	3	-24.45	51.6	262.13±0.52		
4	25.29	-4.3	103.95±0.13	4	25.40	-4.2	177.57±0.53		
6	22.22	-28.0	48.44±0.09	2	22.39	-28.5	412.74±1.21		
7	41.42	-19.2	47.79±0.23	5	41.65	-18.9	140.00±0.10		
9	-0.23	16.9	37.62±0.08	6	-0.22	17.3	109.97±0.61		
10	-0.05	-99.9	35.65±0.22	30	-0.06	-100.5	13.73±0.11		
11	-0.06	16.2	30.27±0.06	7	-0.17	16.7	97.42±0.13		
12	41.19	-18.6	25.91±0.06	14	41.24	-17.8	28.16±0.27		
13	29.88	-38.6	24.18±0.07	15	30.23	-38.9	26.23±0.08		
15	41.36	-28.8	15.13±0.08	18	44.52	-27.8	21.82±0.14		
16	39.75	-14.9	15.12±0.05	19	39.98	-14.4	20.49±0.09		
18	40.04	-15.5	11.65±0.14	24	40.44	-15.3	16.51±0.16		
24	34.96	-92.2	9.77±0.08	38	36.97	-92.7	8.55±0.01		
25	-216.56	-189.6	9.77±0.06	34	-220.91	-190.2	11.37±0.06		
26	30.29	-39.5	8.43±0.08	20	30.75	-40.5	20.18±0.11		
30	-200.02	-171.5	5.71±0.05	39	-199.05	-172.5	7.38±0.08		
Group 2									
37	-1004.24	54.0	66.08±0.13	44	-1004.47	54.3	283.77±0.19		
40	-993.05	48.0	19.84±0.10	46	-993.92	49.8	49.22±0.11		
42	-982.72	44.2	11.81±0.12	55	-981.86	44.7	11.21±0.09		
43	-636.50	62.9	9.98±0.08	51	-636.62	64.0	17.26±0.05		
48	-990.66	-53.4	4.89±0.06	62	-991.36	-53.5	2.89±0.03		
50	-636.33	64.5	4.34±0.12	64	-635.53	64.0	2.18±0.06		
53	-1009.82	56.8	3.18±0.08	50	-1009.93	57.9	20.13±0.10		
Group 3									
54	-2053.53	-130.1	15.26±0.10	65	-2054.11	-130.1	10.82±0.03		

TABLE 4.1: Table showing position and intensity comparison between the masers observed in observations BS198A and BS198B.

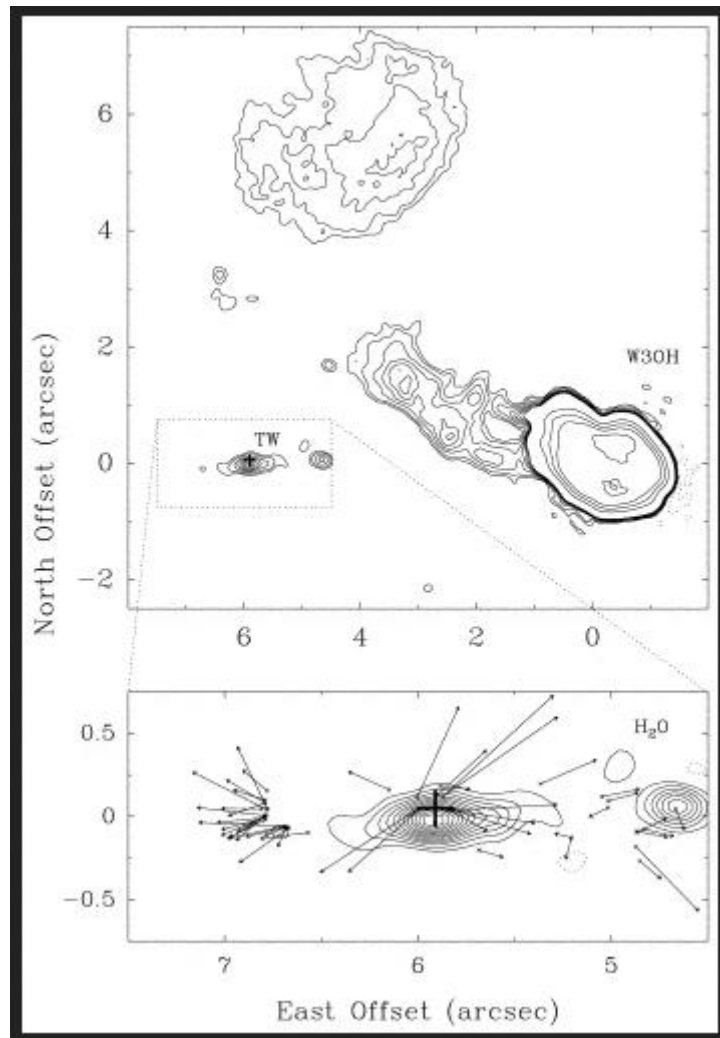


FIGURE 4.2: **Upper:** Continuum image of W3(OH) at 8.44 GHz using the VLA telescope. The lowest contour levels are at 30 and 60  $\mu$  Jy beam<sup>-1</sup>, which then progressively increase by 60-360  $\mu$  Jy beam<sup>-1</sup>, with four highest levels at 5, 10, 15 and 20 mJy beam<sup>-1</sup>. Important structures within the image are explained in §4.2. **Lower:** Image of the TW Object featuring H<sub>2</sub>O maser locations found by Alcolea et al. (1992), along with their proper motions (motion in the plane of the sky). The cross indicates the calculated center of expansion of the H<sub>2</sub>O masers. This image courtesy of Wilner et al. (1999).

from the line of sight. If the orientation is along the plane of the sky, we would expect to observe masers along the east and west of the outflow with velocities close to that of the systematic velocity of the source (see Appendix C) as the shock fronts will propagate perpendicular to the line of sight. If an outflow is observed along the line of sight, we would expect to see a central group of masers of which the velocities would greatly differ from that of the source because of the propagation along the line of sight. We can conclude that the latter case does

not resemble our own, as observation BS198A yields centroid velocities between  $-45.72 \text{ km s}^{-1}$  and  $-66.36 \text{ km s}^{-1}$ , which means all values are within  $\pm 17 \text{ km s}^{-1}$  of the systematic velocity of the source,  $-49.1 \text{ km s}^{-1}$ . Observation BS198B shows similar results, with centroid velocities ranging from  $-48.57 \text{ km s}^{-1}$  to  $-70.43 \text{ km s}^{-1}$ , and are thus within  $\pm 21 \text{ km s}^{-1}$  of the systematic velocity of the source. Velocity differences of this magnitude seem to be in agreement with those expected of a bipolar outflow in the plane of the sky (Moran et al. 1992).

We interpret Groups 1 and 3 to lie at the opposite ends of a bipolar outflow, with Group 2 located closer to the outflow center. This interpretation is consistent with that of Alcolea et al. (1992) who measured the proper motions of the  $\text{H}_2\text{O}$  masers in W3(OH) with VLBI and concluded that the masers were moving outward from a common center along the east-west axis. The lower frame of Figure (4.2) depicts a map of the proper maser motions superposed on a large continuum image of the TW Object. Alcolea et al. (1992) interpreted this east-west motion as a bipolar outflow centered on the TW Object. A comparison map of maser distributions can be seen in Figure (3.4). Our Group 1 masers from both observations appear to coincide with the eastern end of the outflow described by Alcolea et al. (1992), while our masers in Group 3 coincide with the western end of the outflow. A careful examination of the masers in Group 1 shows that our masers are located slightly to the east (left in an astronomical image) of those discovered by Weiler et al. (2009) and Hachisuka et al. (2006), displaying the motion of the masers to the east in accordance with Alcolea et al. (1992).

Also of importance is the greater number of masers observed in Group 1 as opposed to Group 3. The likely cause of this is the orientation of the outflow with respect to the Earth. If the outflow were perfectly in the plane of the sky, we would observe a roughly equal number of masers in both groups. Instead, we have observed 42 masers in Group 1 and 3 in Group 3 for observation BS198B, and similar for BS198A. We interpret this as evidence that the outflow is oriented at some angle to the plane of the sky. This angle must be rather small, as the maser velocities in Groups 1 and 3 are not too different from the systematic velocity of our source.

The maser distribution in Group 2 can be interpreted as lying at the base of the outflow that has the masers of Group 1 and Group 3 at its ends. For observation BS198A we observed 20 masers with velocities between  $-48.97 \text{ km s}^{-1}$   $-56.10 \text{ km s}^{-1}$  yielding an average of  $-52.91 \text{ km s}^{-1}$ , and 22 masers with a velocity range of  $-48.57 \text{ km s}^{-1}$  to  $-62.62 \text{ km s}^{-1}$  with an average of  $-57.09 \text{ km s}^{-1}$  for BS198B.

Alcolea et al. (1992) studied the proper motions of the masers in Group 2 and concluded that they had significantly larger proper motion vectors than did the masers in Groups 1 and 3. The combination of these two findings shows that the velocity vectors for the masers in Group 2 are high, which is consistent with their location at the base of an outflow.

Finally, we will discuss the difference in velocities between BS198A and BS198B. BS198A yielded an average velocity of  $-51.73 \text{ km s}^{-1}$  while BS198B yielded an average value of  $-56.64 \text{ km s}^{-1}$ . Moreover, the most intense maser in each observation, though sharing the same location in space, show a difference in central velocity between the two observations of  $5.02 \text{ km s}^{-1}$ . This drift in maser velocity between the two observations is interpreted as an acceleration of the outflow (Lekht et al. 2006). Lekht et al. (2006) studied multiple  $\text{H}_2\text{O}$  masers through multiple observations spanning years and found that such drifts in velocity were fairly common and often came about with changes in maser intensity.

## 4.4 Magnetic Fields

As mentioned in §3.2, we observed significant Zeeman detection in our most intense maser source in both observations. The  $B_{los}$  in the most intense maser in both epochs changes from  $-28.85 \text{ mG}$  to  $-43.39 \text{ mG}$  with an intensity difference of  $52.3 \text{ Jy}$ . These values are reasonable and of the order with previous observations of line of sight magnetic fields (Sarma et al. 2002, Sarma et al. 2008), usually of the order of tens of mG. We have also detected  $B_{los}$  in other masers, even though errors in the Stokes V profile due to residual sidelobes caused by the peak maser have introduced a significant amount of noise into one or both ends of the Stokes V profile. For the time being, we consider these as suggestive magnetic fields, and must work to see if the calibration can be improved to reduce the sidelobe contamination.

### 4.4.1 Preshock and Postshock Magnetic Fields

As  $\text{H}_2\text{O}$  masers undergo collisional excitation due to shock fronts, we next define two regions, preshock and postshock. The preshock region displays the characteristics of the local region before it was impacted by the shock front, while the

material of the postshock region is influenced by the shock front. We seek to determine whether or not the magnetic fields obtained by our observations are consistent with the other observed quantities in preshock and postshock regions of previous studies. To do this, we follow the analysis given in Sarma et al. (2008). In the following derivations, the subscript “0” is used to represent the preshock region, while the subscript “1” represents the postshock region.

We define the magnetic energy density as  $B_1^2/8\pi$ , where  $B_1$  is the magnetic field of the postshock region. We can determine  $B_1$  from our observed magnetic fields in §3.2. As discussed in equation (2.27), we determine the line of sight magnetic fields as  $B_{los}=B_1\cos\theta$ , and assuming  $B_1$  can be oriented at any angle to the line of sight, then values of  $\theta$  range from 0 to  $\frac{\pi}{2}$ , and we get:

$$B_{los} = \int_0^{\frac{\pi}{2}} B_1 \cos\theta \sin\theta d\theta = - \int_0^{\frac{\pi}{2}} B_1 \cos\theta d(\cos\theta)$$

Putting  $\cos\theta = z$ :

$$B_{los} = - \int_0^1 B_1 z dz = B_1 \left[ \frac{z^2}{2} \right]_0^1$$

$$B_{los} = \frac{B_1}{2} \tag{4.1}$$

By squaring  $B_{los}=B_1\cos\theta$  and integrating, we get:

$$B_{los}^2 = \int_0^{\frac{\pi}{2}} B_1^2 \cos^2\theta \sin\theta d\theta = \int_0^{\frac{\pi}{2}} B_1^2 \cos^2\theta d(\cos\theta)$$

$$B_{los}^2 = \frac{B_1^2}{3} \tag{4.2}$$

This method is taken from Crutcher (1999), and shows that on statistical grounds we can show that  $B_1=2B_{los}$  and  $B_1^2=3B_{los}^2$ . Guesten et al. (1994) derived the number density in the preshock region of W3(OH) to be of the order of  $n_o = 10^7 \text{ cm}^{-3}$ , corresponding to a preshock density of  $\rho_o = 4.7 \times 10^{-17} \text{ g cm}^{-3}$ . We can relate the preshock density to the postshock density as:

$$\frac{B_o}{\rho_o} = \frac{B_1}{\rho_1} \quad (4.3)$$

Where the preshock magnetic field can be calculated by:

$$B_o = \beta \rho_o^{\frac{1}{2}} \quad (4.4)$$

where  $\beta$  is the intrinsic proportionality constant, and was evaluated by Sarma et al. (2002) to be  $\beta \approx 5.8 \times 10^5$ . Using our  $B_{los}$  values of  $-28.85$  mG from BS198A and  $-43.49$  mG for BS198B, we calculate the postshock density to be  $\rho_1 = 6.8 \times 10^{-16}$  g cm $^{-3}$ , corresponding to a postshock number density of  $n_1 = 1.5 \times 10^8$  cm $^{-3}$ , for BS198A and  $\rho_1 = 1.0 \times 10^{-15}$  g cm $^{-3}$ , corresponding to a postshock number density of  $n_1 = 2.2 \times 10^8$  cm $^{-3}$  for BS198B. Collisional excitation of the H $_2$ O maser was studied by Elitzur et al. (1989) and determined that number densities on the order of  $10^8$ - $10^9$  cm $^{-3}$  will allow for efficient collisional pumping. Our derived number densities for both epochs are in agreement with this theoretical limit.

#### 4.4.2 Energy Considerations

As discussed at the top of this section, the magnetic energy density is equal to  $B_1^2/8\pi$ . Using the relation  $B_1^2 = 3B_{los}^2$ , we calculate a magnetic energy density for BS198A of  $9.8 \times 10^{-5}$  erg cm $^{-3}$  and for BS198B of  $2.3 \times 10^{-4}$  erg cm $^{-3}$ . This value can be compared to the kinetic energy density, given by  $\frac{3}{2}mn\sigma^2$ , where  $n$  is the particle density,  $m$  is the mean mass per particle, and  $\sigma$  is the velocity dispersion and is equal to  $\Delta v/(8\ln 2)^{\frac{1}{2}}$ , with  $\Delta v$  is the FWHM velocity of the maser which measured the  $B_{los}$ . Since we are observing a region of molecular Hydrogen,  $m=2.33m_p$ , where the 10% He mixed in the H is taken into account. Using these parameters, we have calculated a kinetic energy density of  $2.2 \times 10^{-6}$  erg cm $^{-3}$  for BS198A and  $2.9 \times 10^{-6}$  erg cm $^{-3}$ .

Comparing the magnetic and kinetic energy densities, we see that the magnetic energy density is greater by 2 orders of magnitude, and therefore dominant in the region. It is possible that the  $\Delta v$  value obtained from the maser lines are too narrow, as masers are amplified along the path of greatest velocity coherence, causing the line center to be amplified much more than line sides in a process known as line narrowing. This indicates that the maser linewidth may not be

typical of the dispersion in the masing region. A more typical value,  $\Delta v=4 \text{ km s}^{-1}$  obtained from non-maser lines, yield a kinetic energy density of  $2.5 \times 10^{-5} \text{ erg cm}^{-3}$  for BS198A and  $3.7 \times 10^{-5} \text{ erg cm}^{-3}$  for BS198B. These values would suggest a magnetic energy density somewhere in the range of an order of magnitude greater or on the order of the kinetic energy density. In either case, it is evident that the magnetic field plays a significant role in the dynamics of W3(OH).

### 4.4.3 Magnetic Field Comparison

A comparison of the magnetic field measured in maser 1 from BS198A and BS198B shows a change in the magnetic field of  $\Delta B_{los} = -14.54 mG$ . This can be interpreted as being due to a higher velocity shock front. In this scenario, a higher velocity shock front will compress the masing cloud more than the lower velocity shock front. This compression drives the molecules closer together, thus increasing the magnetic force between them. This increase in magnetic force will also be seen as an increase in the magnitude of the measured magnetic field. We can relate shock front velocity to the postshock magnetic field and shock ram pressure through

$$\frac{B_1^2}{8\pi} = \rho_o u_s^2 \quad (4.5)$$

where  $u_s$  is the shock front velocity. Using a preshock density of  $\rho_o = 4.7 \times 10^{-17} \text{ g cm}^{-3}$  from §4.4.1, we calculate a shock front velocity of  $u_s=14.4 \text{ km s}^{-1}$  for BS198A and  $u_s=22.1 \text{ km s}^{-1}$  for BS198B. It is this increase in shock front velocity that we consider responsible for the increase in the magnetic field measurement.

# Chapter 5

## Conclusions

In this thesis, we presented VLBA observation results for H<sub>2</sub>O masers in the star forming region W3(OH).

- We have detected a total of 54 masers in observation BS198A and 67 masers in observation BS198B.
- We concluded that observation BS198B showed features consistent with a flaring event due to an increased number of masers along with higher maser intensities.
- We arranged the masers from both epochs into 3 groups; with the most intense maser in both epochs (occupying the same point spatially) in the easternmost group, which we designated Group 1. The westernmost group was designated to be Group 3, and Group 2 fell in between. For BS198A, we detected a total of 33 masers in Group 1, 20 masers in Group 2, and a single maser in Group 3. The most intense maser has an intensity of  $949.50 \pm 5.46$ , with maser intensities spanning 3 orders of magnitude. Central velocities ranged from  $-45.72 \text{ km s}^{-1}$  to  $-66.36 \text{ km s}^{-1}$ , with an average of  $-51.73 \text{ km s}^{-1}$ . The FWHM line widths range from  $0.61 \text{ km s}^{-1}$  to  $1.94 \text{ km s}^{-1}$  with an average of  $1.10 \text{ km s}^{-1}$ . For BS198B, we detected a total of 42 masers in Group 1, 22 masers in Group 2, and 3 masers in Group 3. The most intense maser has an intensity of  $1001.80 \pm 3.67$ , with maser intensities spanning 3 orders of magnitude. Central velocities ranged from  $-48.57 \text{ km s}^{-1}$  to  $-70.43 \text{ km s}^{-1}$ , with an average of  $-56.46 \text{ km s}^{-1}$ . The FWHM line

widths range from  $0.65 \text{ km s}^{-1}$  to  $2.01 \text{ km s}^{-1}$  with an average of  $1.09 \text{ km s}^{-1}$ .

- We interpreted the morphology of the masers as indicative of tracing a bipolar outflow, with the masers in Group 1 tracing the eastern edge, Group 3 tracing the western edge, and the masers of Group 2 at the outflow base. Our interpretation is in agreement with the outflow direction presented by Alcolea et al. (1992). A close look at our masers from Group 1 shows that many of our masers lie to the east of those of previous observations, in agreement with the proper motion of the masers measured by Hachisuka et al. (2006). We see evidence to support the direction of the outflow is at a slight angle to the plane of the sky, as the eastern side of the outflow (Group 1) has more masers than the western side (Group 3).
- We detected a drift in the line of sight velocities between BS198A and BS198B, and have interpreted this as an acceleration of the outflow. Such drifts are fairly common with changes in maser intensity, and are discussed by Lekht et al. (2006).
- We detected significant  $B_{los}$  for three masers in BS198A and 12 masers in BS198B. The observed magnetic field strengths in the most intense maser for each epoch were  $-28.85 \text{ mG}$  for BS198A and  $-43.49 \text{ mG}$  for BS198B. All detections are consistent with magnetic fields in similar regions (e.g., Sarma et al. 2008).
- Using the accepted preshock density of the region ( $\rho_o = 4.7 \times 10^{-17} \text{ g cm}^{-3}$ ), we calculated a postshock density of  $\rho_1 = 6.8 \times 10^{-16} \text{ g cm}^{-3}$ , corresponding to a postshock number density of  $n_1 = 1.5 \times 10^8 \text{ cm}^{-3}$ , for BS198A and  $\rho_1 = 1.0 \times 10^{-15} \text{ g cm}^{-3}$ , corresponding to a postshock number density of  $n_1 = 2.2 \times 10^8 \text{ cm}^{-3}$  for BS198B. These values are in agreement with theoretical number densities needed for collisional pumping of  $\text{H}_2\text{O}$  masers in postshock regions (Elitzur et al. 1989).
- Finally, we calculated a magnetic energy density for BS198A of  $9.8 \times 10^{-4} \text{ erg cm}^{-3}$  and for BS198B of  $2.3 \times 10^{-4} \text{ erg cm}^{-3}$ . We also calculated a kinetic energy density of  $2.2 \times 10^{-6} \text{ erg cm}^{-3}$  for BS198A and  $2.9 \times 10^{-6} \text{ erg cm}^{-3}$  for BS198B, or  $2.5 \times 10^{-5} \text{ erg cm}^{-3}$  for BS198A and  $3.7 \times 10^{-5} \text{ erg cm}^{-3}$  for BS198B, assuming two different values for  $\Delta v_{FWHM}$  (either the

maser linewidth or more typical value of dispersion in the region). A comparison of the magnetic energy density to either case of the kinetic energy density reveals that a significant amount of the total energy in the region is contributed by the magnetic field, indicating that the magnetic field is dynamically significant to the star forming region.

The purpose of this thesis was to compare the results obtained through VLBA observations of H<sub>2</sub>O masers in W3(OH) taken between two epochs, compare their morphology, and compare their magnetic fields. We interpreted the observation BS198A as a period of quiescence, while the observation BS198B is a period of flaring. The morphology of the detected masers of both epochs are in agreement with those of past observations. We also observed a drift in the central line velocities of the masers between the two epochs and interpreted it as an acceleration of the outflow. The calculated postshock densities for both epochs are in agreement with the values required for H<sub>2</sub>O masing in these regions. Finally, the magnetic energy density is calculated to be in the range of between the order of the kinetic energy density, or up to two orders of magnitude larger, indicating that the magnetic field is significant in the region.

# Appendix A

## Gaussian Fits of Stokes I Maser Spectra from BS198A

The following pages of this appendix display the Gaussian fit plots of our Stokes I profiles for the masers discovered from observation BS198A, from which we obtained many of our parameters.

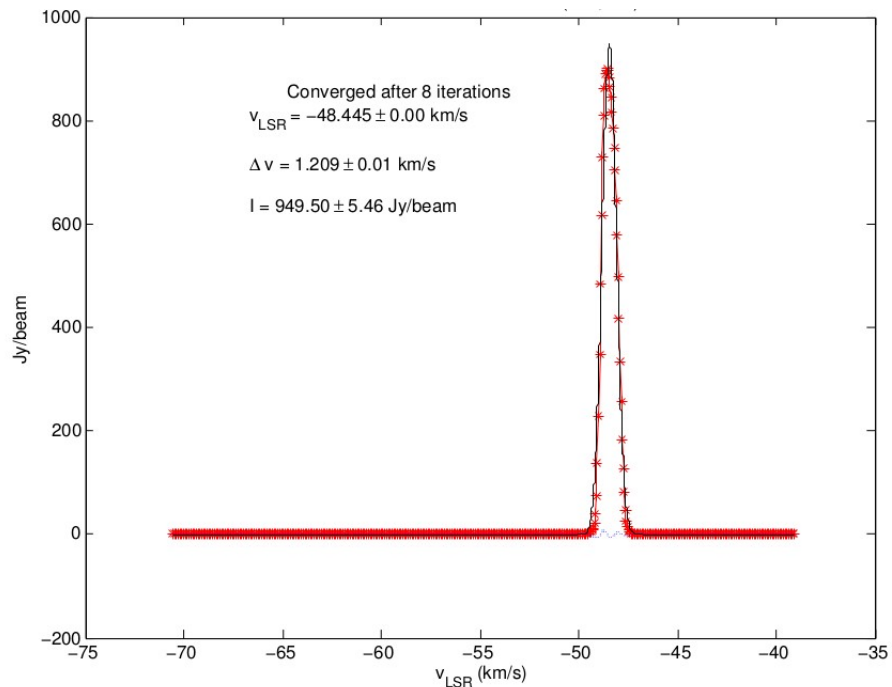


FIGURE A.1: Gaussian fit plot of the Stokes I profile of maser 1 from observation BS198A. We used a least squares fit program in Matlab for all Gaussian fits. The parameters obtained are also displayed in the figure.

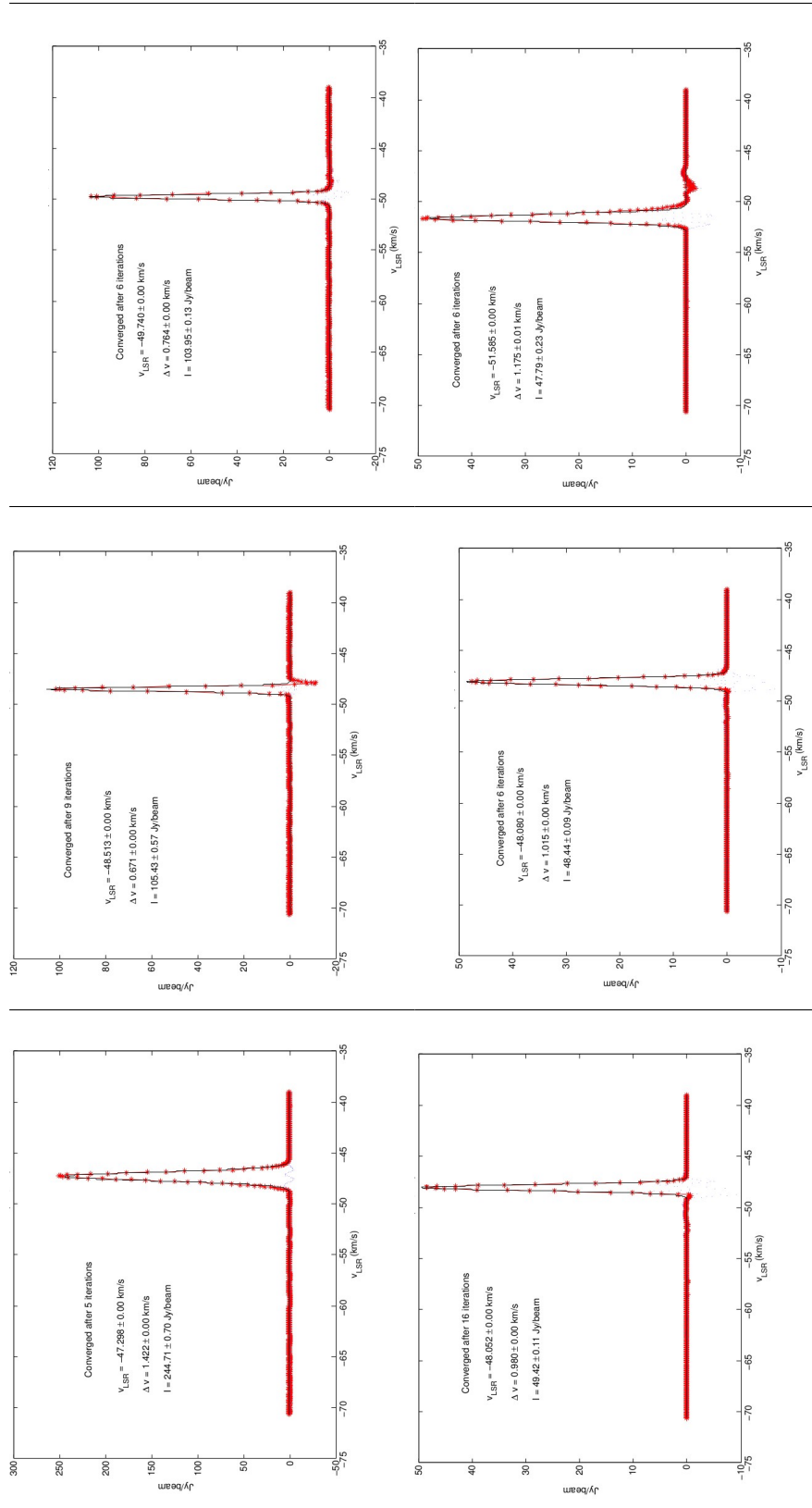


FIGURE A.2: Gaussian fit plot of the Stokes I profile of masers 2-7 from observation BS198A. Top Row: (left) Maser 2, (center) Maser 3, (right) Maser 4. Bottom Row: (left) Maser 5, (center) Maser 6, (right) Maser 7

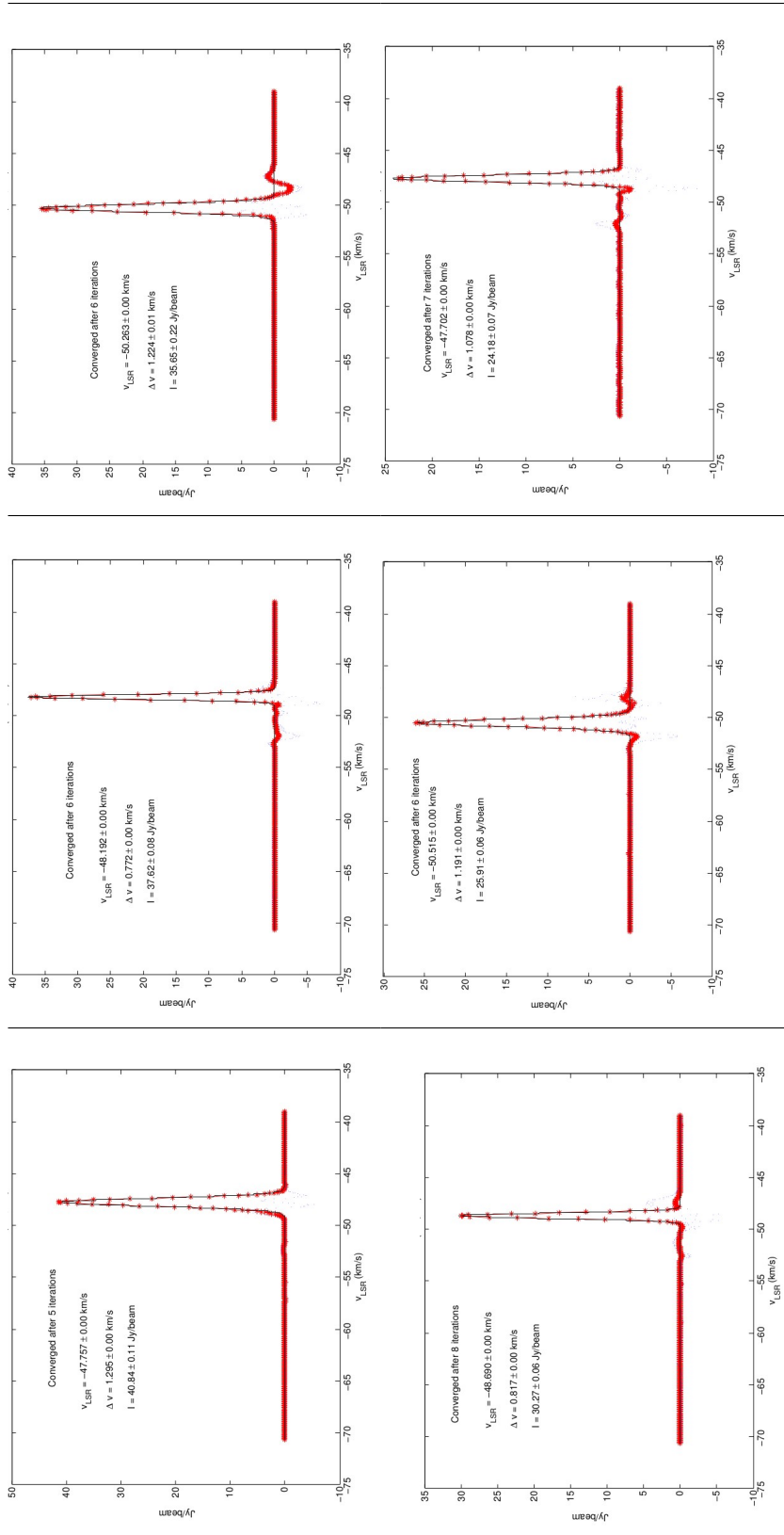


FIGURE A.3: Gaussian fit plot of the Stokes I profile of masers 8-13 from observation BS198A. Top Row: (left) Maser 8, (center) Maser 9, (right) Maser 10. Bottom Row: (left) Maser 11, (center) Maser 12, (right) Maser 13

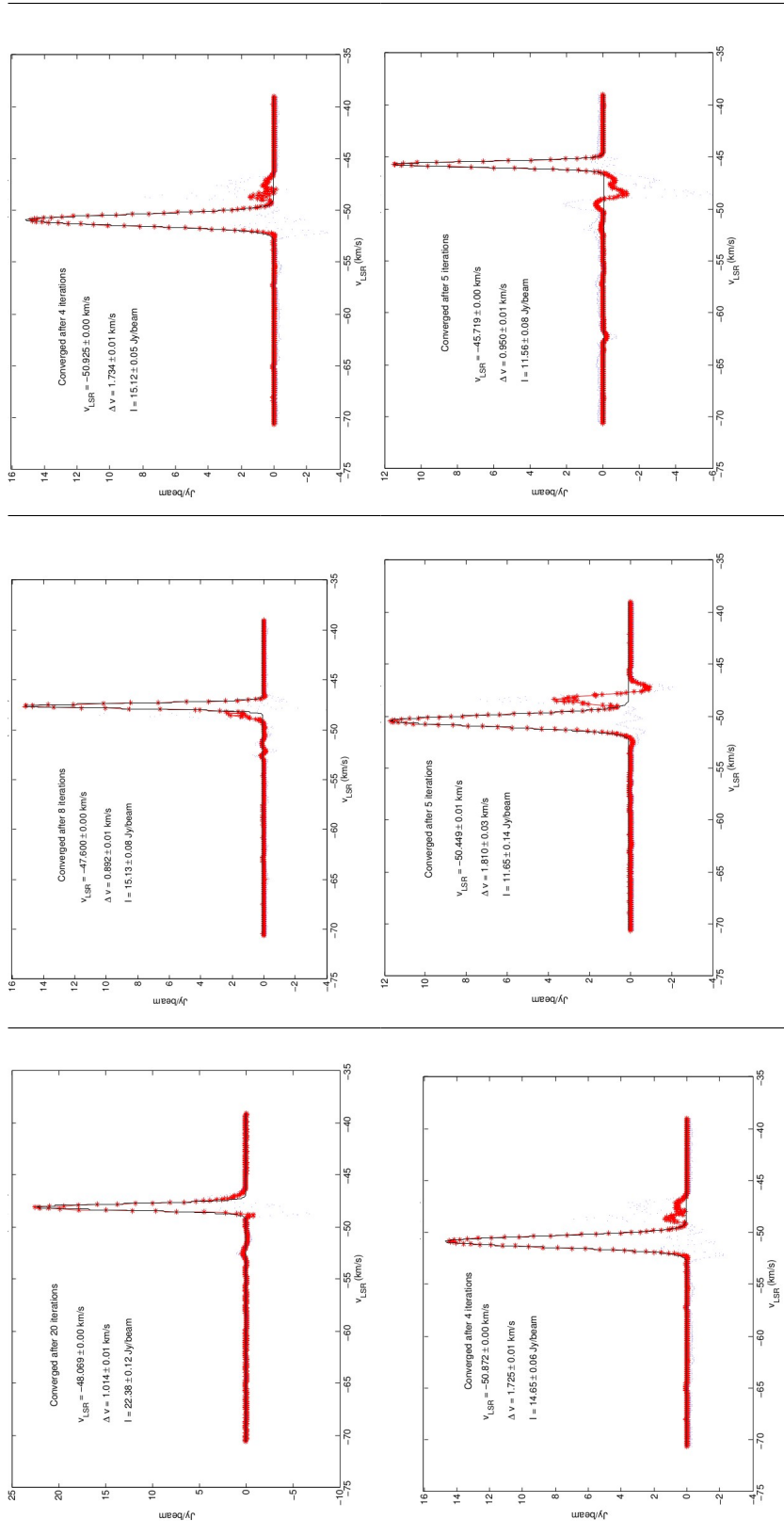


FIGURE A.4: Gaussian fit plot of the Stokes I profile of masers 14-19 from observation BS198A. Top Row: (left) Maser 14, (center) Maser 15, (right) Maser 16. Bottom Row: (left) Maser 17, (center) Maser 18, (right) Maser 19

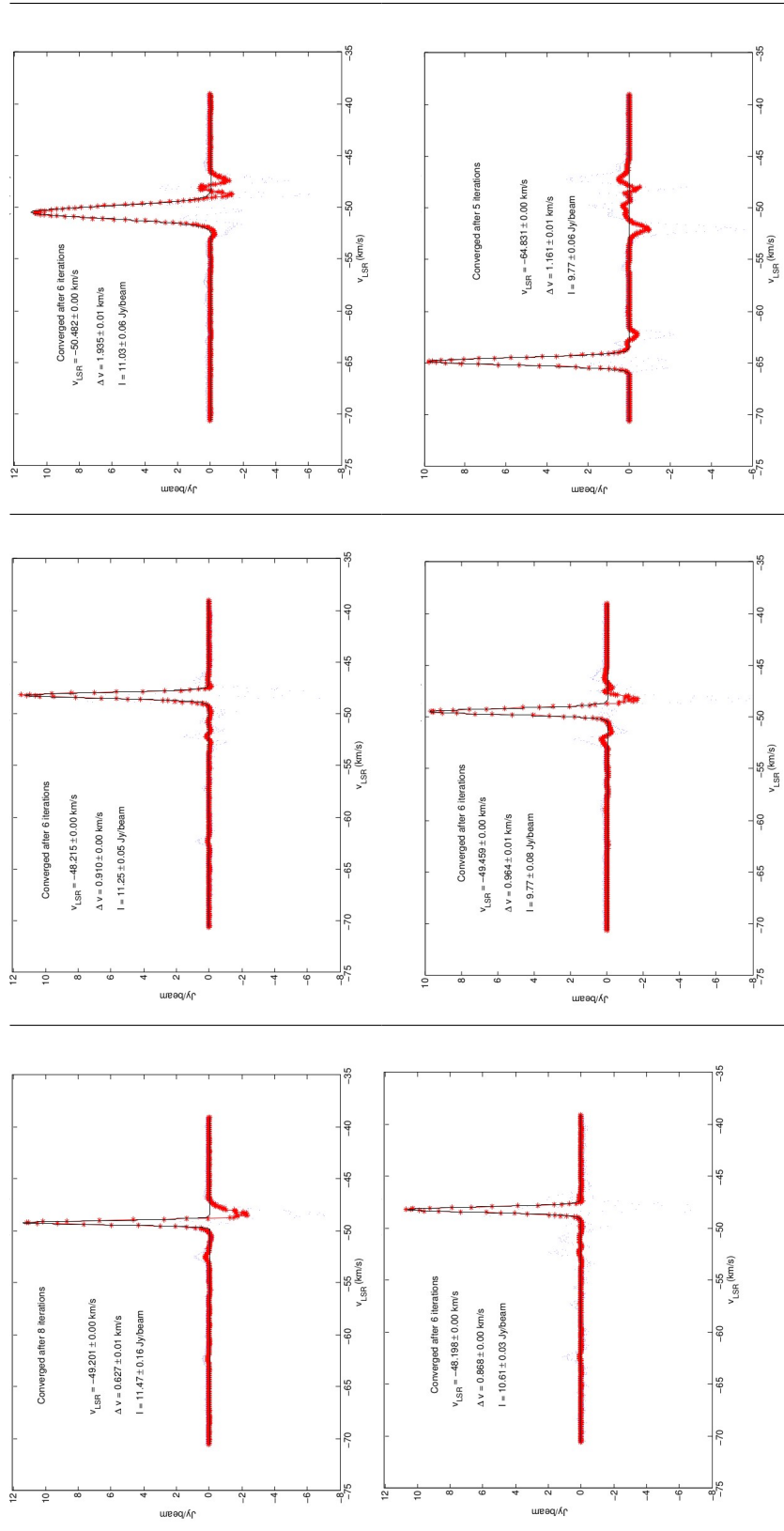


FIGURE A.5: Gaussian fit plot of the Stokes I profile of masers 20-25 from observation BS198A. Top Row: (left) Maser 20, (center) Maser 21, (right) Maser 22. Bottom Row: (left) Maser 23, (center) Maser 24, (right) Maser 25

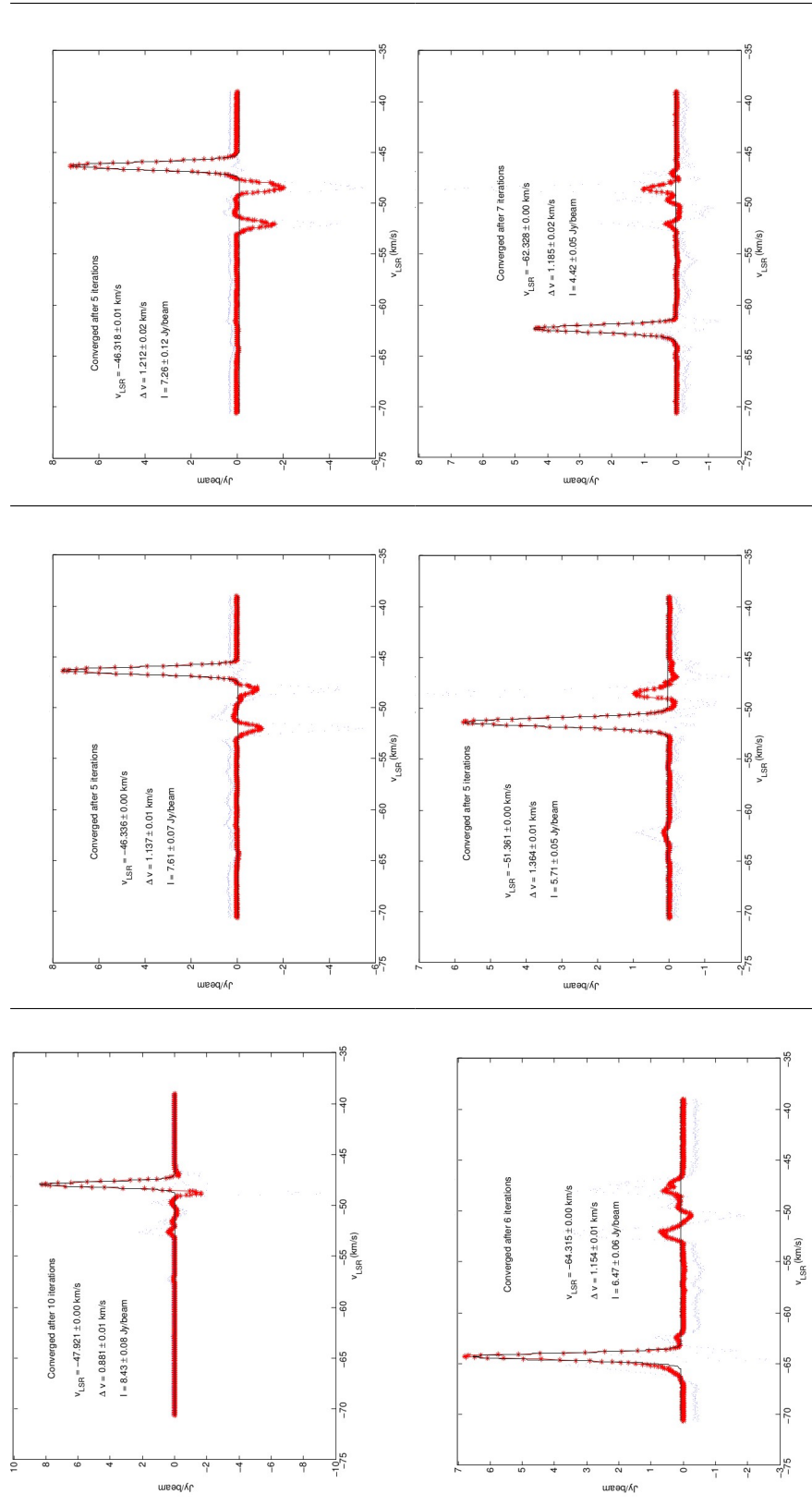


FIGURE A.6: Gaussian fit plot of the Stokes I profile of masers 26-31 from observation BS198A. Top Row: (left) Maser 26, (center) Maser 27, (right) Maser 28. Bottom Row: (left) Maser 29, (center) Maser 30, (right) Maser 31

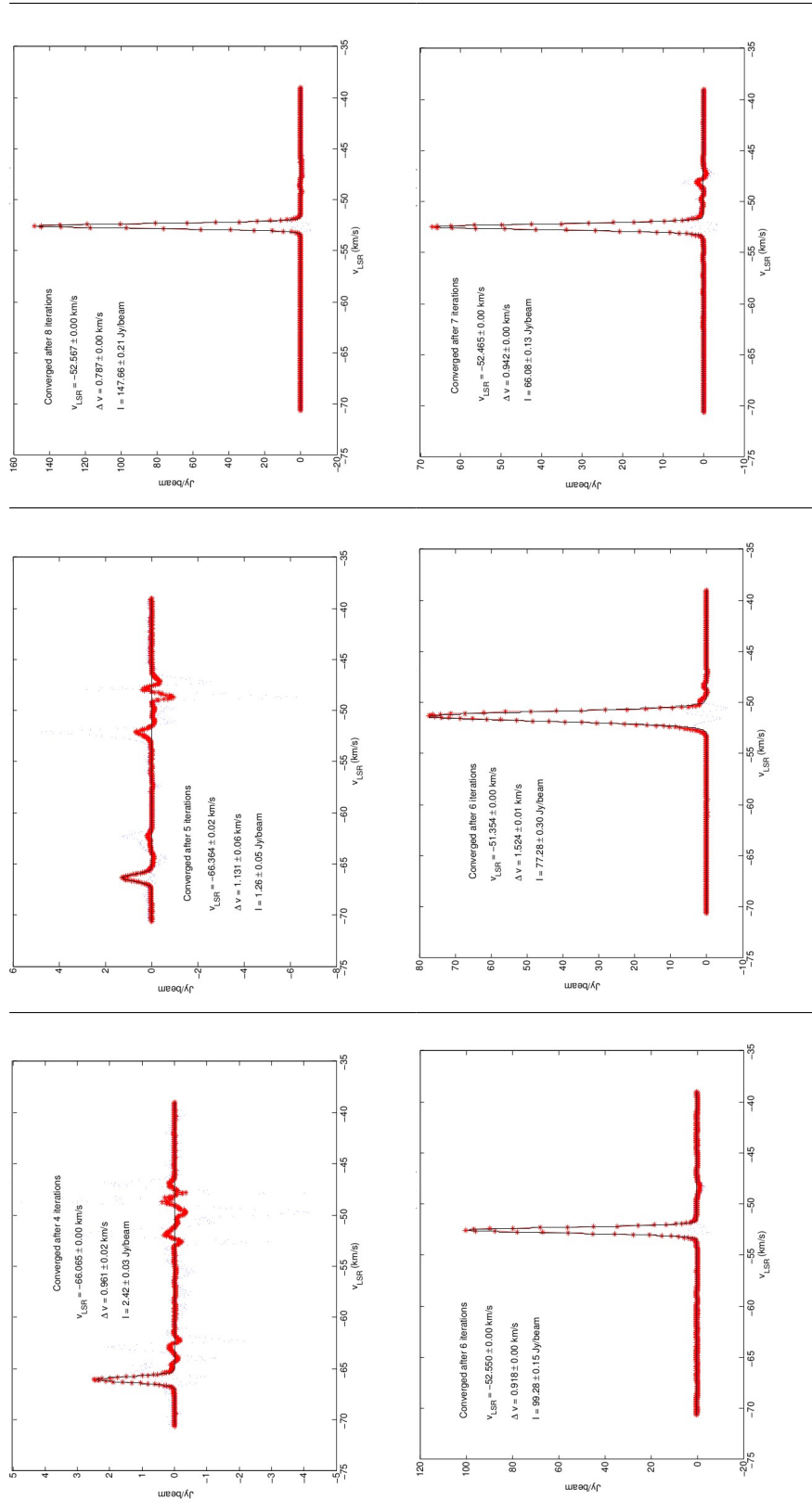


FIGURE A.7: Gaussian fit plot of the Stokes I profile of masers 32-37 from observation BS198A. Top Row: (left) Maser 32, (center) Maser 33, (right) Maser 34. Bottom Row: (left) Maser 35, (center) Maser 36, (right) Maser 37

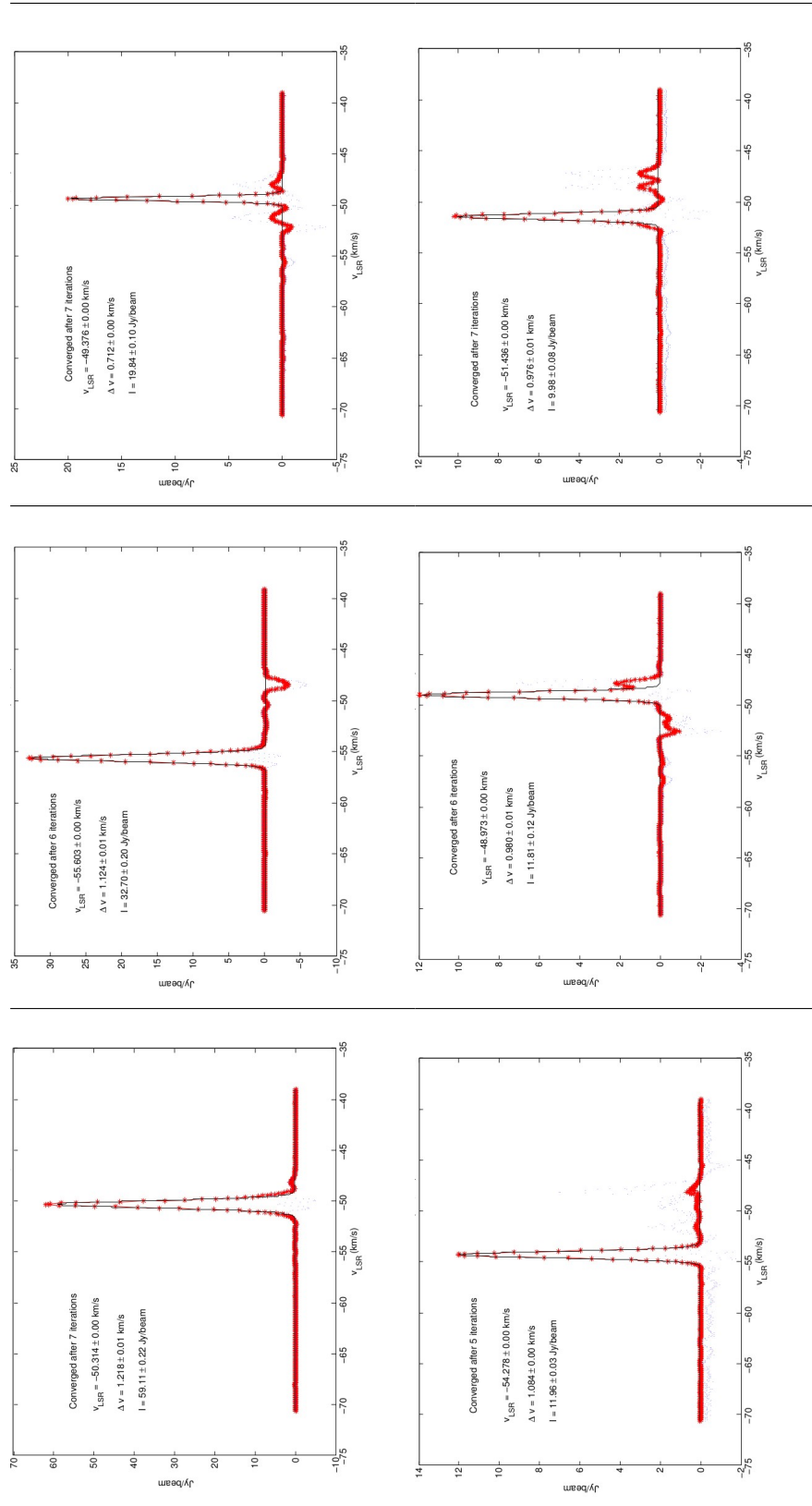


FIGURE A.8: Gaussian fit plot of the Stokes I profile of masers 38-43 from observation BS198A. Top Row: (left) Maser 38, (center) Maser 39, (right) Maser 40. Bottom Row: (left) Maser 41, (center) Maser 42, (right) Maser 43

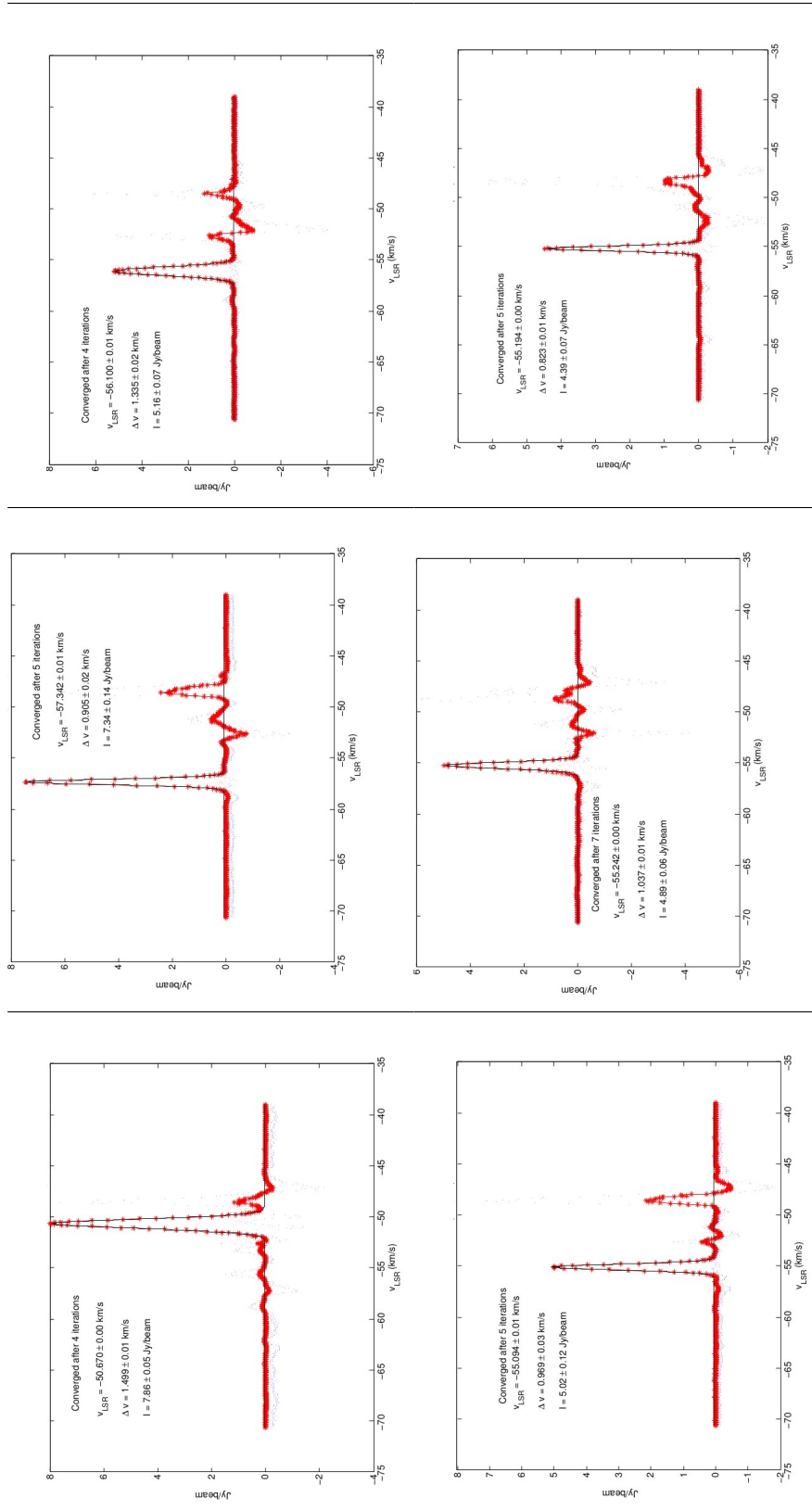


FIGURE A.9: Gaussian fit plot of the Stokes I profile of masers 44-49 from observation BS198A. Top Row: (left) Maser 44, (center) Maser 45, (right) Maser 46. Bottom Row: (left) Maser 47, (center) Maser 48, (right) Maser 49

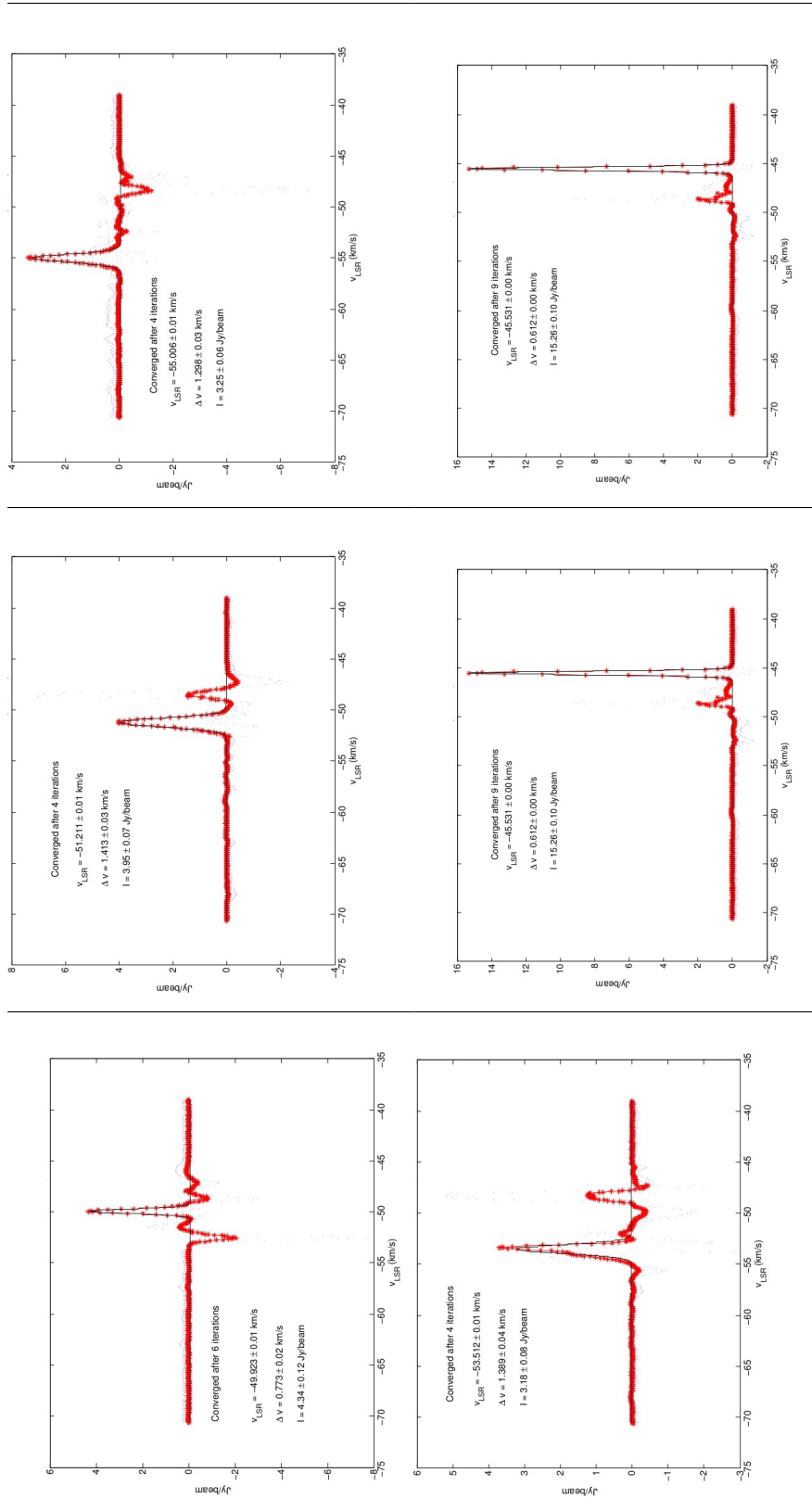


FIGURE A.10: Gaussian fit plot of the Stokes I profile of masers 50-54 from observation BS198A. Top Row: (left) Maser 50, (center) Maser 51, (right) Maser 52. Bottom Row: (left) Maser 53, (center) Maser 54

# Appendix B

## Gaussian Fits of Stokes I Maser Spectra from BS198B

The following pages of this appendix display the Gaussian fit plots of our Stokes I profiles for the masers discovered from observation BS198B, from which we obtained many of our parameters.

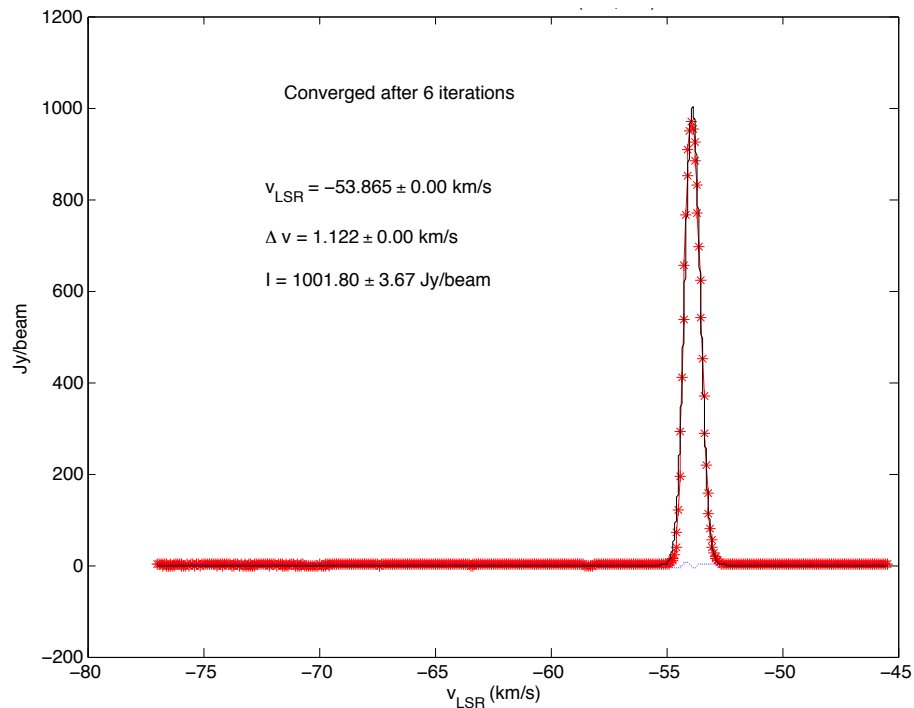


FIGURE B.1: Gaussian fit plot of the Stokes I profile of maser 1 from observation BS198B. We used a least squares fit program in Matlab for all Gaussian fits. The parameters obtained are also displayed in the figure.

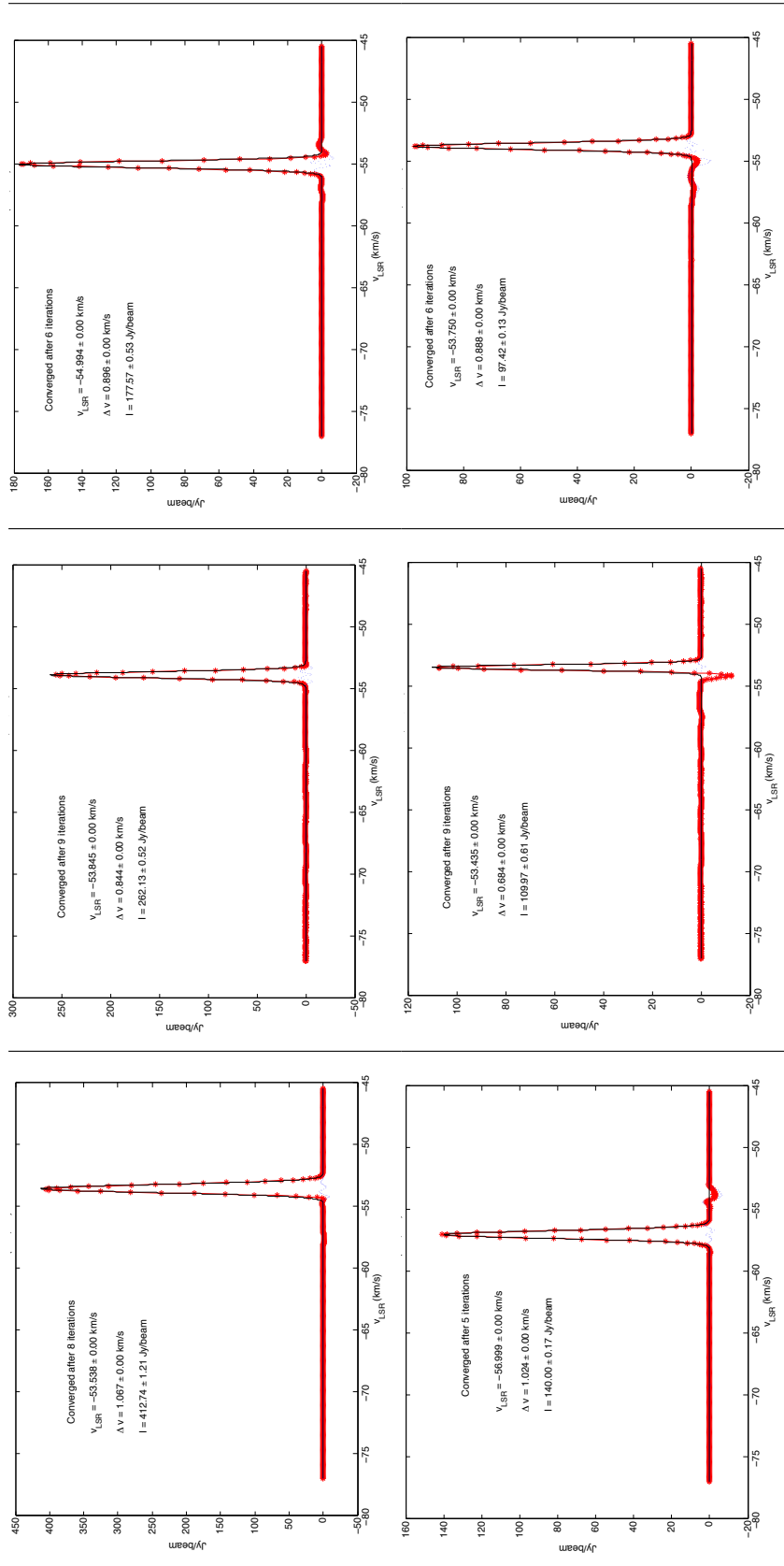


FIGURE B.2: Gaussian fit plot of the Stokes I profile of masers 2-7 from observation BS198B. Top Row: (left) Maser 2, (center) Maser 5, (right) Maser 7. Bottom Row: (left) Maser 6, (center) Maser 5, (right) Maser 7

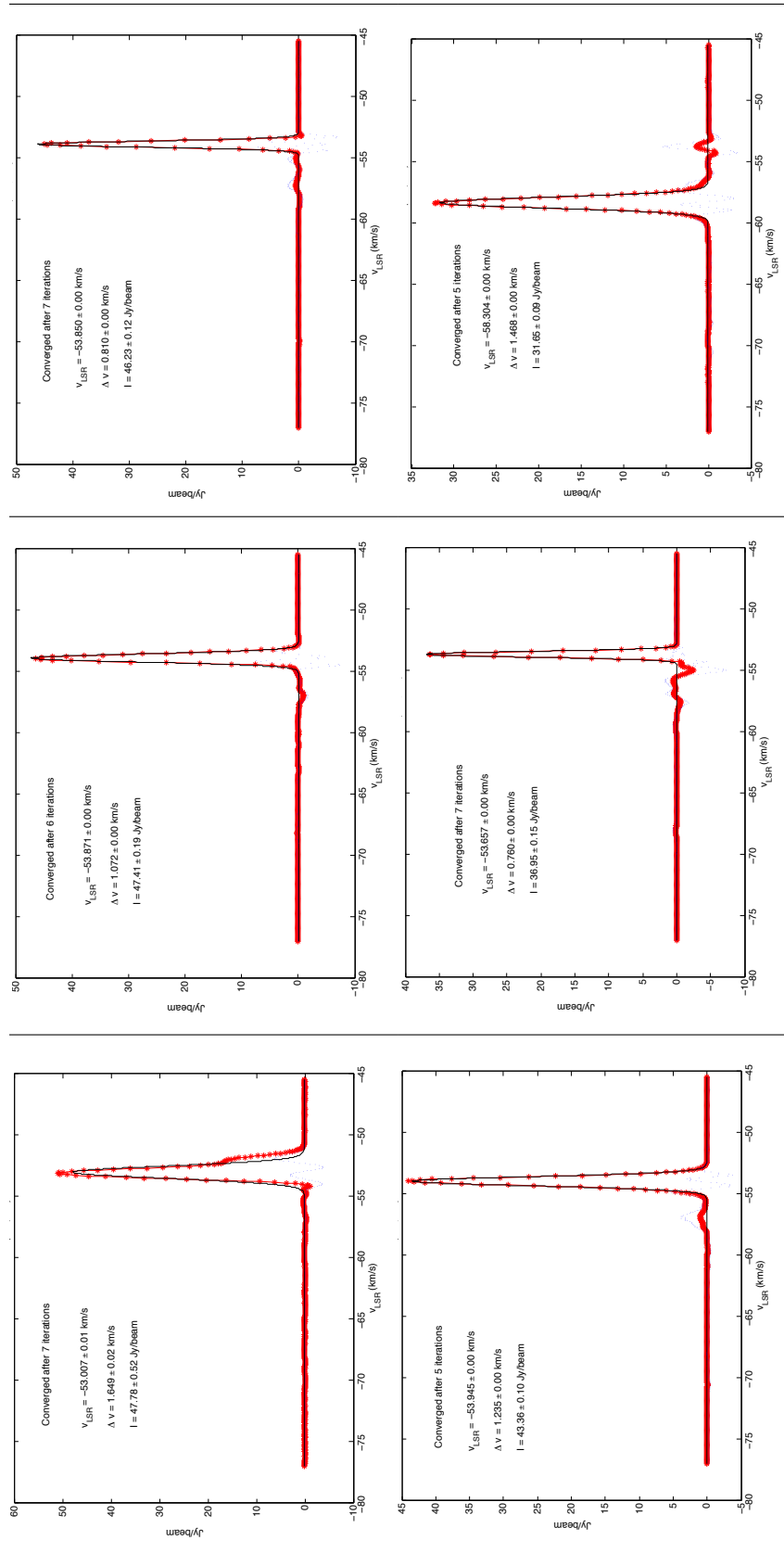


FIGURE B.3: Gaussian fit plot of the Stokes I profile of masers 8-13 from observation BS198B. Top Row: (left) Maser 8, (center) Maser 11, (right) Maser 12. Bottom Row: (left) Maser 9, (center) Maser 10, (right) Maser 13

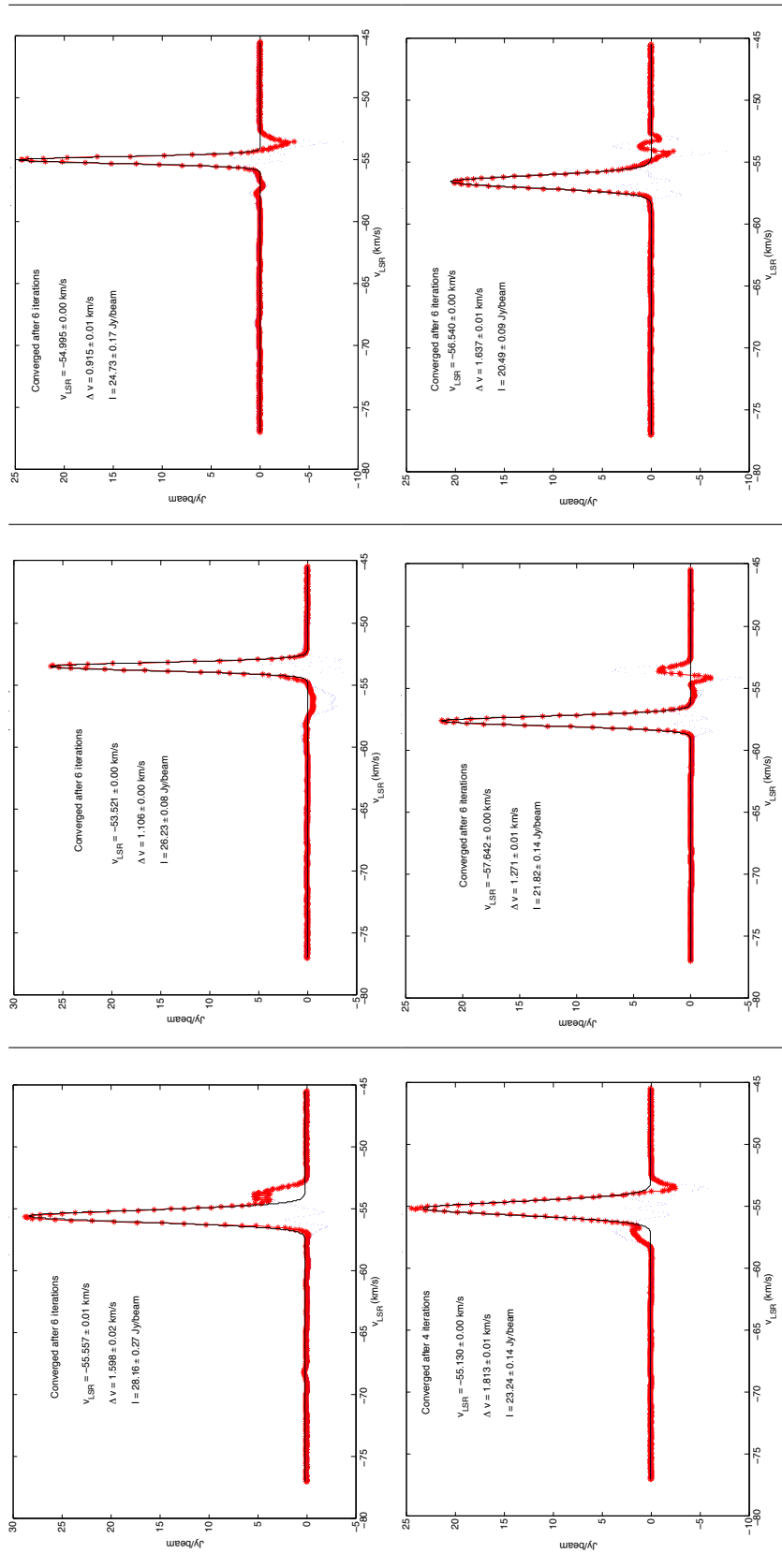


FIGURE B.4: Gaussian fit plot of the Stokes I profile of masers 14-19 from observation BS198B. Top Row: (left) Maser 14, (center) Maser 15, (right) Maser 16. Bottom Row: (left) Maser 17, (center) Maser 18, (right) Maser 19

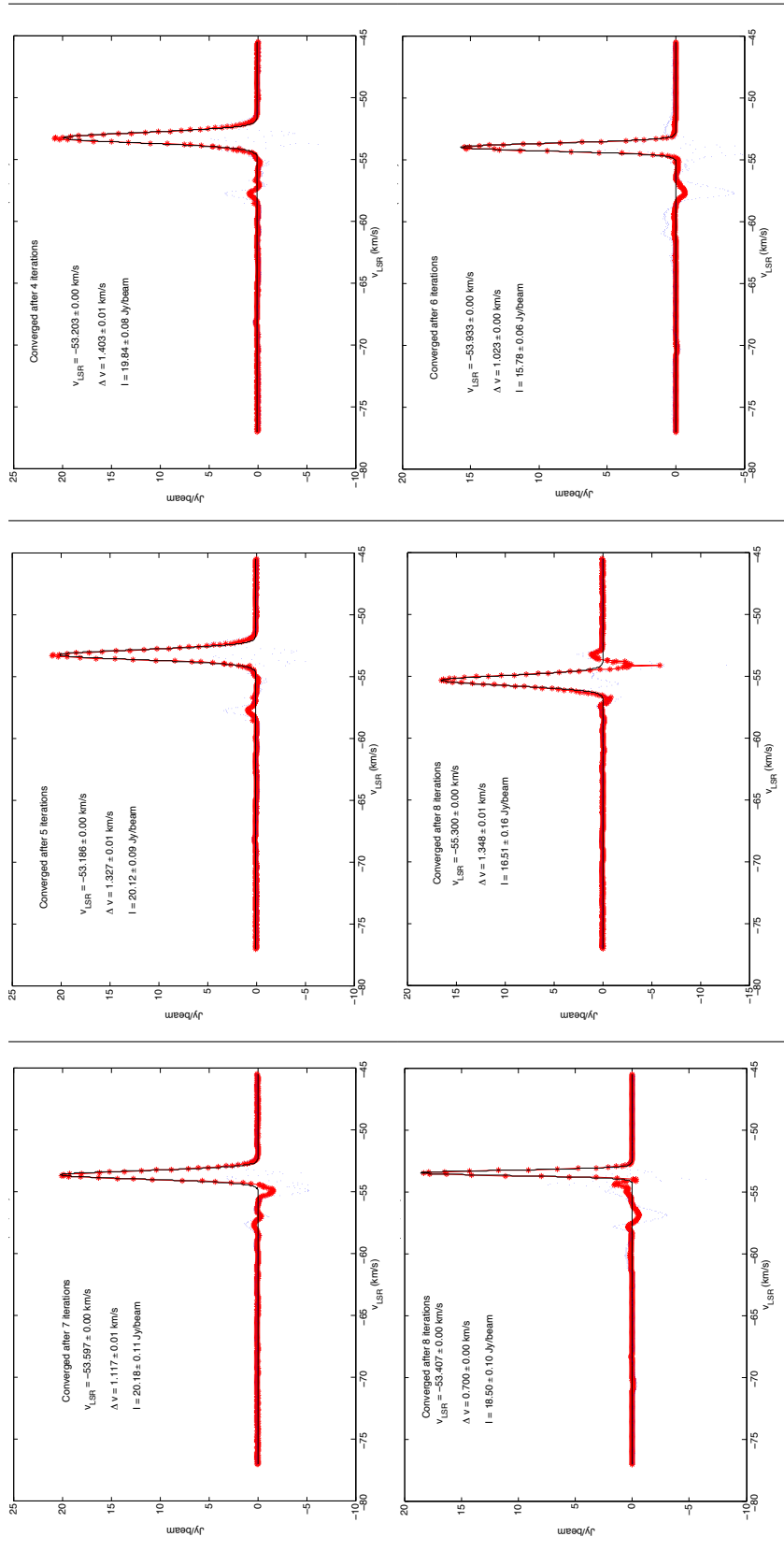


FIGURE B.5: Gaussian fit plot of the Stokes I profile of masers 20-25 from observation BS198B. Top Row: (left) Maser 20, (center) Maser 21, (right) Maser 22. Bottom Row: (left) Maser 23, (center) Maser 24, (right) Maser 25

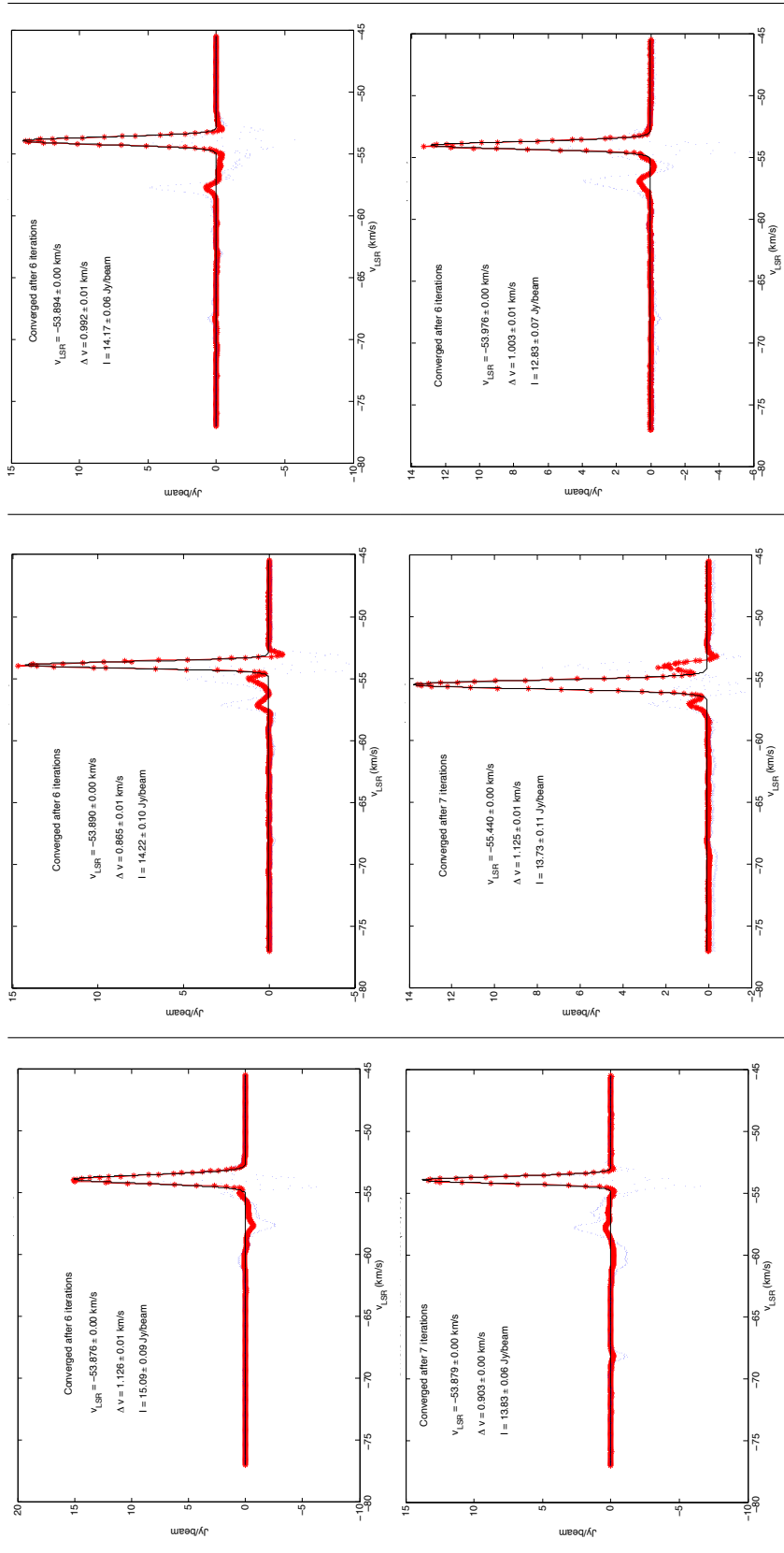


FIGURE B.6: Gaussian fit plot of the Stokes I profile of masers 26-31 from observation BS198B. Top Row: (left) Maser 26, (center) Maser 27, (right) Maser 28. Bottom Row: (left) Maser 29, (center) Maser 30, (right) Maser 31

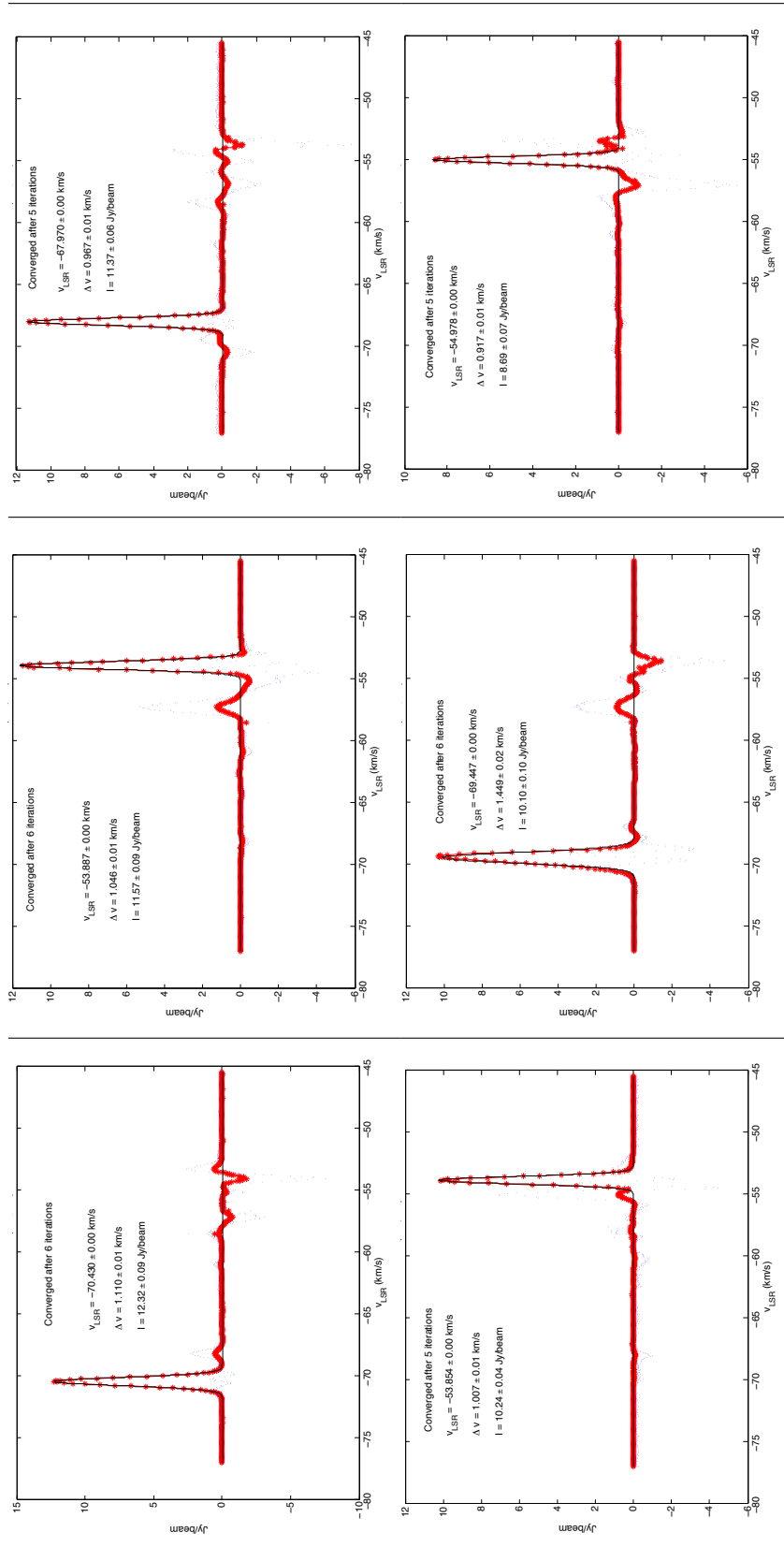


FIGURE B.7: Gaussian fit plot of the Stokes I profile of masers 32-37 from observation BS198B. Top Row: (left) Maser 32, (center) Maser 33, (right) Maser 34. Bottom Row: (left) Maser 35, (center) Maser 36, (right) Maser 37

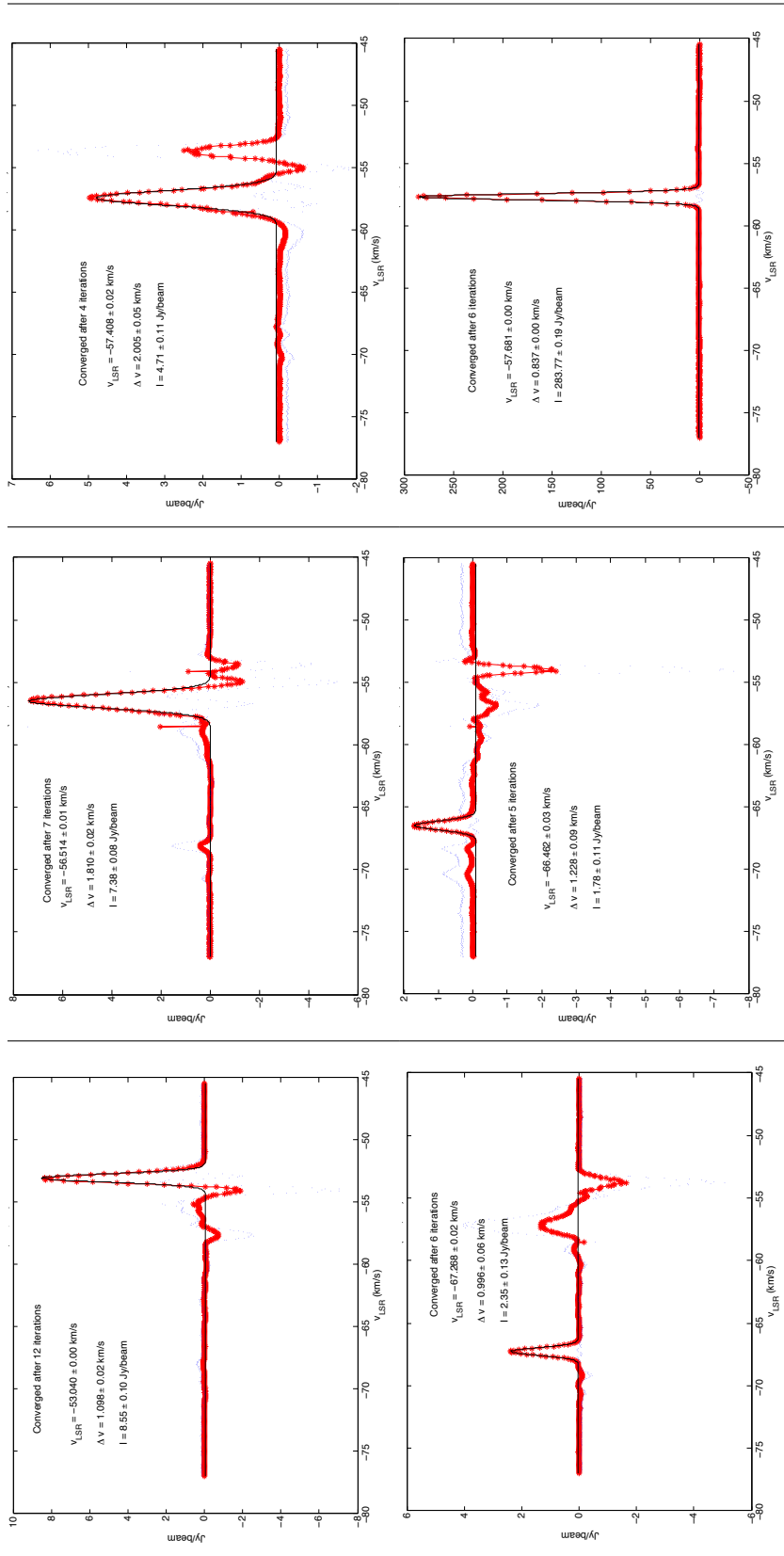


FIGURE B.8: Gaussian fit plot of the Stokes I profile of masers 38-43 from observation BS198B. Top Row: (left) Maser 38, (center) Maser 39, (right) Maser 40. Bottom Row: (left) Maser 41, (center) Maser 42, (right) Maser 43

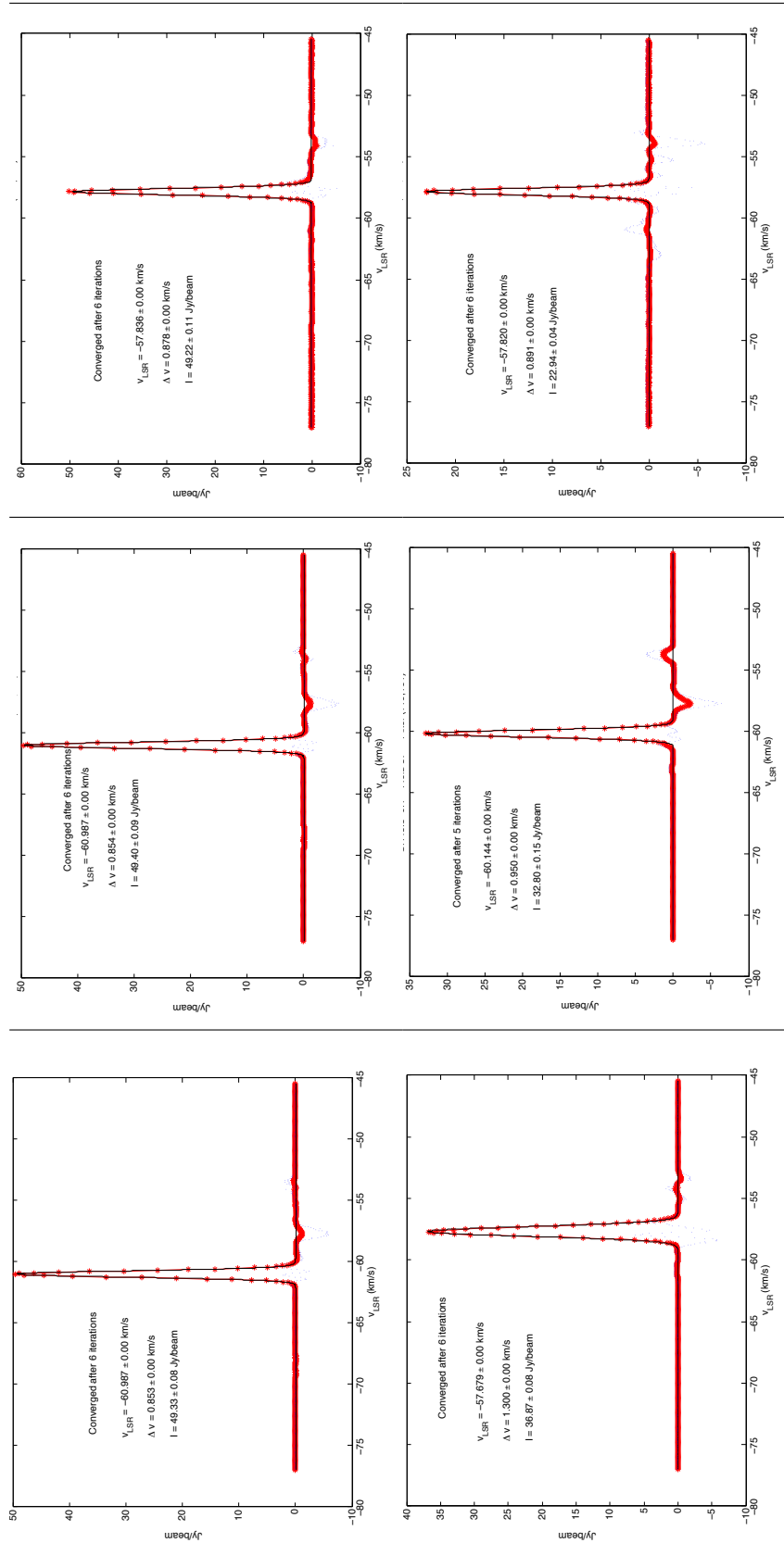


FIGURE B.9: Gaussian fit plot of the Stokes I profile of masers 44-49 from observation BS198B. Top Row: (left) Maser 44, (center) Maser 45, (right) Maser 46. Bottom Row: (left) Maser 47, (center) Maser 48, (right) Maser 49

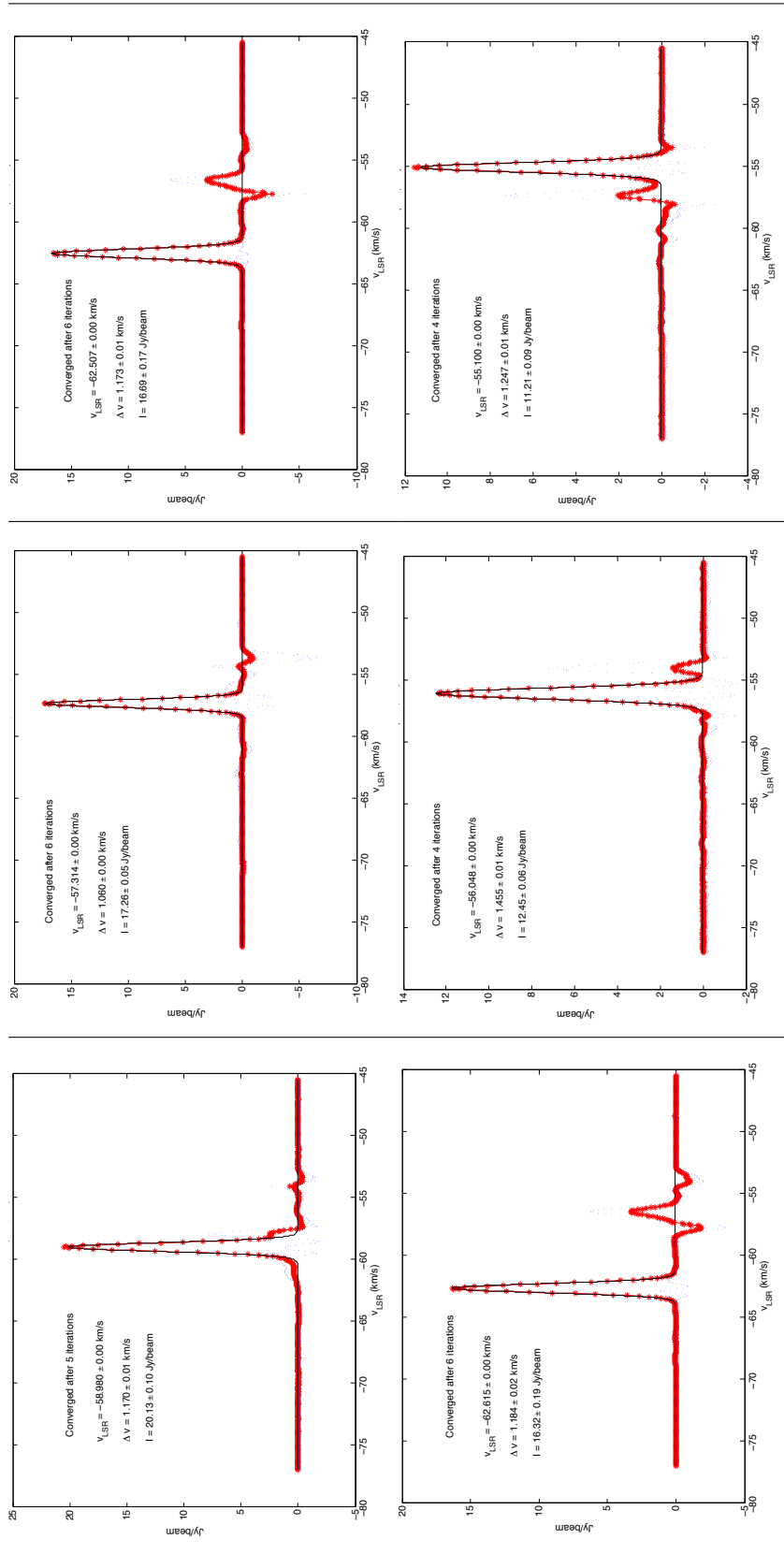


FIGURE B.10: Gaussian fit plot of the Stokes I profile of masers 50-55 from observation BS198B. Top Row: (left) Maser 50, (center) Maser 51, (right) Maser 52. Bottom Row: (left) Maser 53, (center) Maser 54, (right) Maser 55

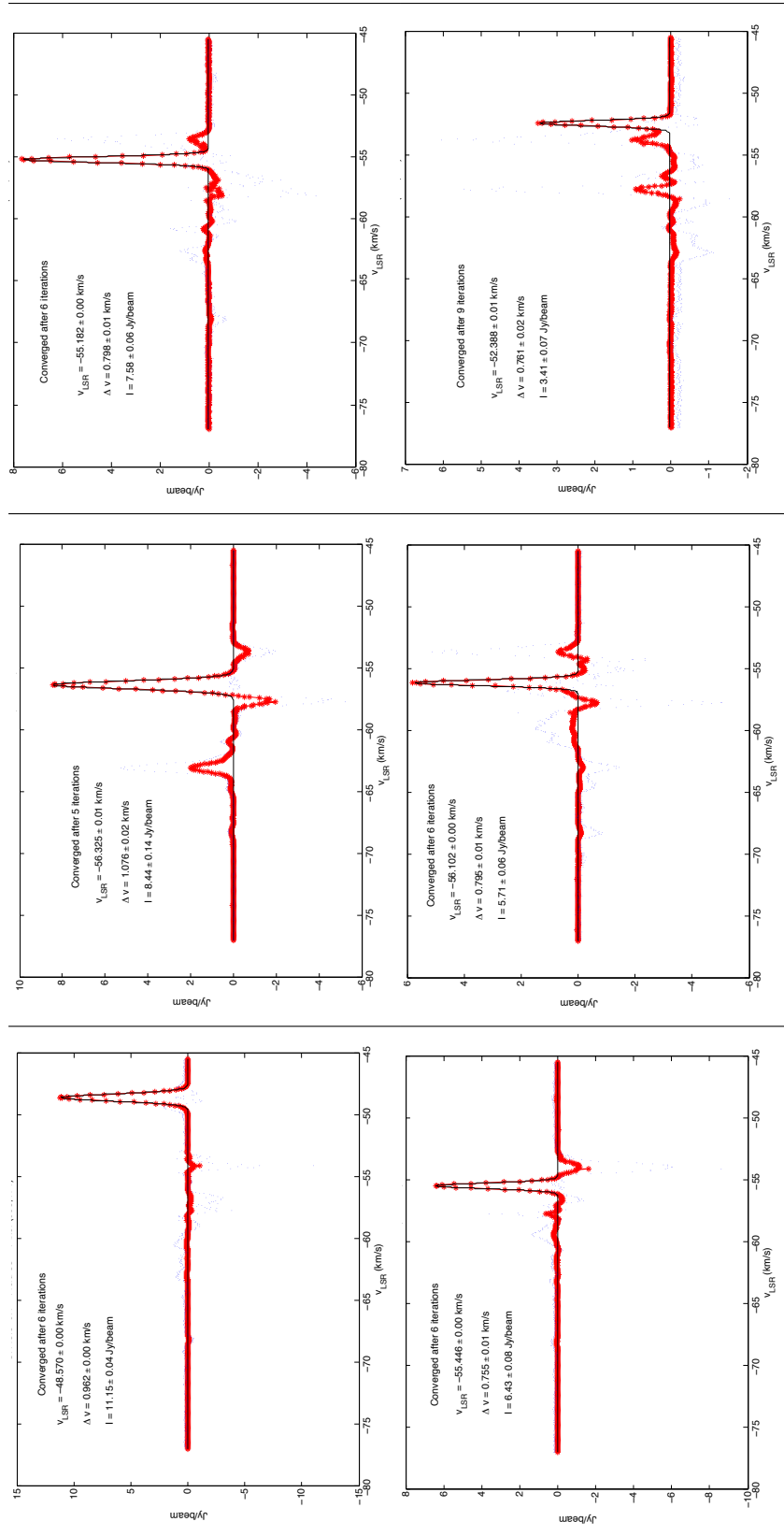


FIGURE B.11: Gaussian fit plot of the Stokes I profile of masers 56-61 from observation BS198B. Top Row: (left) Maser 56, (center) Maser 57, (right) Maser 58. Bottom Row: (left) Maser 59, (center) Maser 60, (right) Maser 61

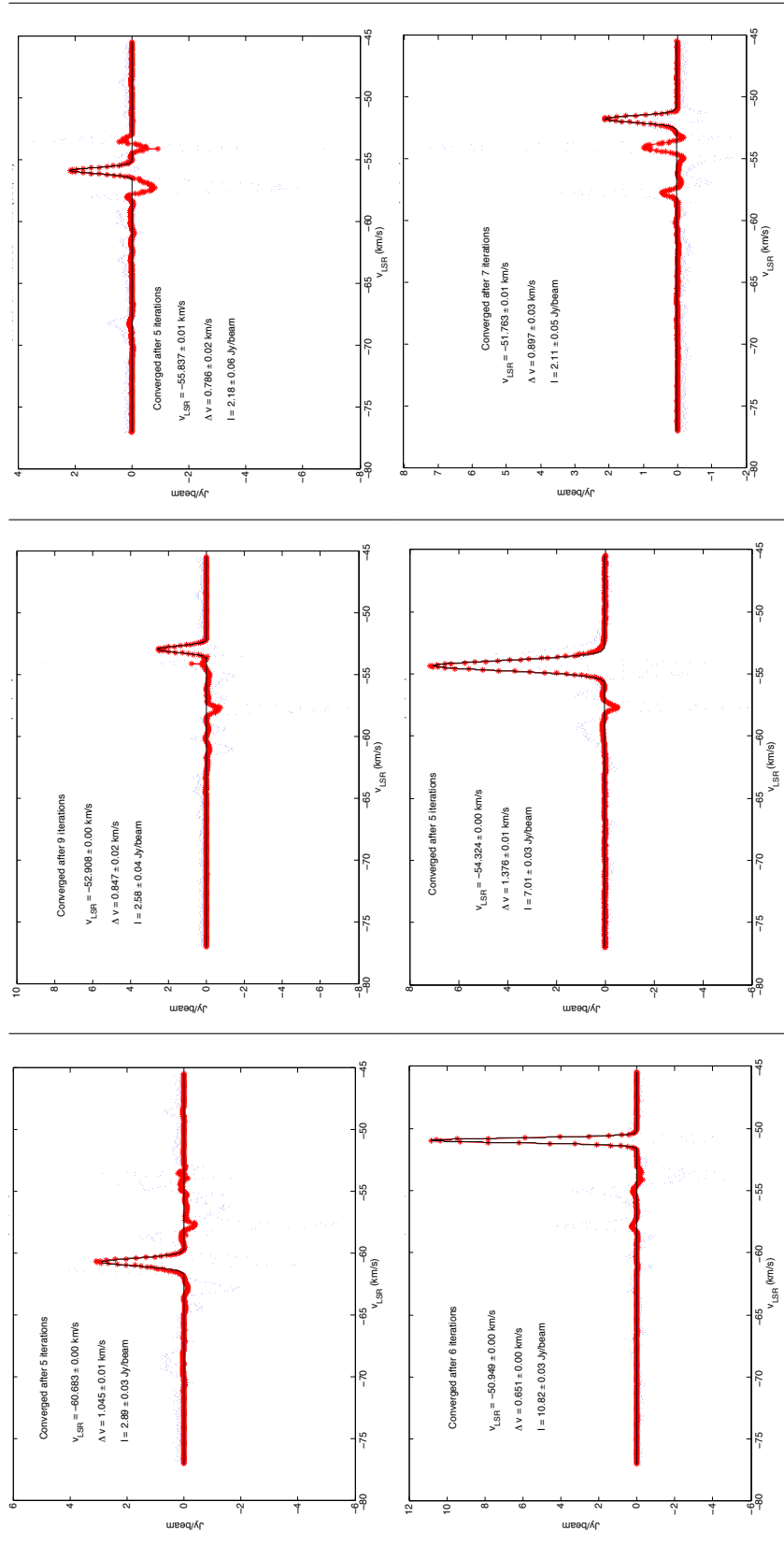


FIGURE B.12: Gaussian fit plot of the Stokes I profile of masers 62-67 from observation BS198B. Top Row: (left) Maser 62, (center) Maser 63, (right) Maser 64. Bottom Row: (left) Maser 65, (center) Maser 66, (right) Maser 67

# Appendix C

## Systemic Velocity of an Astronomical Source

Throughout this work we make reference to the line of sight velocity of the star forming region W3(OH). In this appendix, we will describe what is meant by the line of sight velocity, as well as the systemic velocity of an astronomical source.

For simplicity, astronomers use the assumption that material moving in our galactic disk rotates about an axis perpendicular to the galactic center. Since the matter in the galaxy is centrally concentrated we can approximate the motions of the objects in our galaxy as Keplerian orbits about the center of the galaxy, and so stars and molecular clouds that orbit closer to the galactic center have a greater angular velocity (see figure C.1). This means that objects closer to the center of the galaxy will have shorter orbital periods than those that orbit further from the Galactic Center. This is known as differential rotation.

Let us now consider the radial velocities of stars in the galaxy relative to the sun. Looking at figure (C.1), we can decipher that if we look toward  $l = 0^\circ$  or  $l = 180^\circ$  we would not see any motion along the line of sight due to galactic rotation because all objects in these directions are moving perpendicular to the line of sight. Similarly, we will not observe angular velocities for nearby stars toward the directions  $l = 90^\circ$  or  $l = 270^\circ$  because they will be traveling with the same orbital velocity as the sun as they share a common radius from the galactic center. In all of the stated cases  $v_{lsr}=0$ , where the subscript "lsr" refers to the local standard of rest, an inertial frame defined with respect to distant stars, which appear motionless.

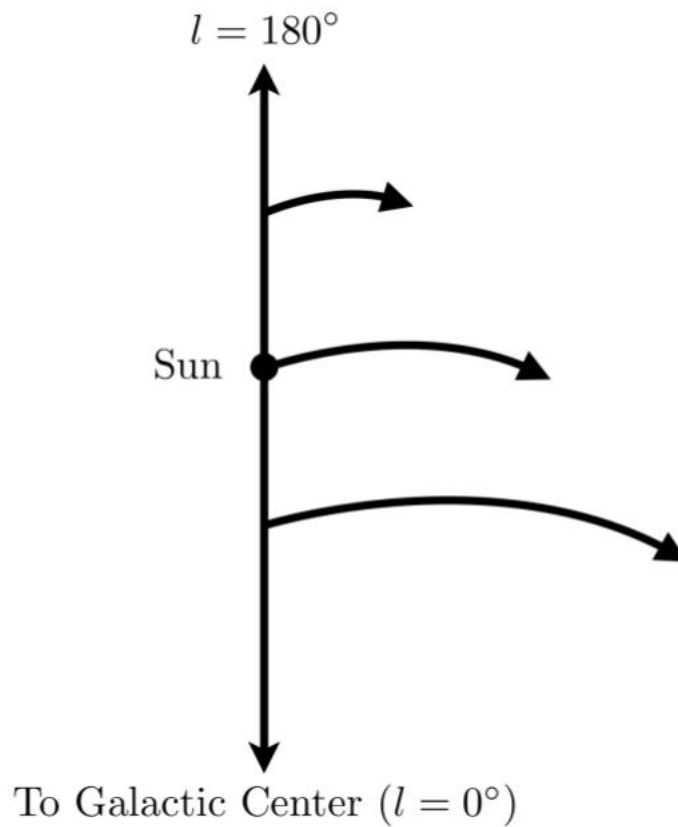


FIGURE C.1: Figure showing the rotational velocities in a differentially rotating galaxy. This figure shows approximately Keplerian orbits around the Galactic Center. Figure courtesy of “Galactic Astronomy-Structure and Kinematics” by Mihalas and Binney.

Figure (C.2) will be used to define the line of sight velocities at other longitudinal coordinates. To do so, we must first define some quantities:

- $R \equiv$  The radial distance to the star or molecular cloud from the galactic center.
- $R_o \equiv$  The radial distance from the sun to the galactic center.
- $V \equiv$  The linear velocity of the Galaxy at radius  $R$ , with direction perpendicular to  $R$ .
- $V_o \equiv$  The linear velocity our Galaxy at radius  $R_o$ , with direction perpendicular to  $R_o$ .
- $\omega = V/R \equiv$  The angular velocity of the Galaxy at radius  $R$ .
- $\omega_o = V_o/R_o \equiv$  The angular velocity of the Galaxy at radius  $R_o$ .

- $v_{lsr} \equiv$  The observed line of sight (radial) velocity of a star or molecular cloud.
- $l \equiv$  The galactic longitude of the observed object.

Using these quantities, we can begin to understand figure (C.2).

$$v_{lsr} = V \cos \alpha - V_o \sin l \quad (\text{C.1})$$

Using the law of sines

$$\frac{\sin l}{R} = \frac{\sin(\pi + \alpha)}{R_o} = \frac{\cos \alpha}{R_o}. \quad (\text{C.2})$$

Combining equation (C.2) with (C.1)

$$v_{lsr} = V \left( \frac{R_o \sin l}{R} \right) - V_o \sin l. \quad (\text{C.3})$$

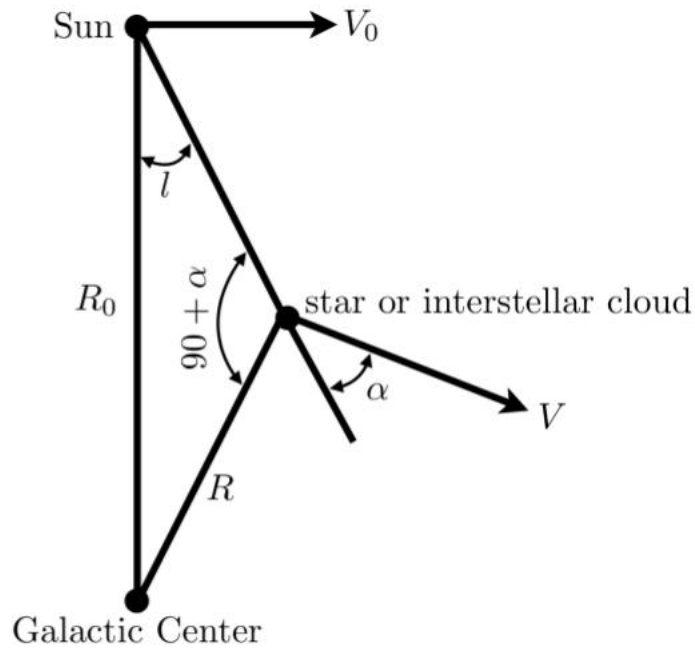


FIGURE C.2: Figure showing the geometric relationship between the quantities used in the derivation. Figure courtesy of "Galactic Astronomy-Structure and Kinematics" by Mihalas and Binney.

Using the radial velocity relations

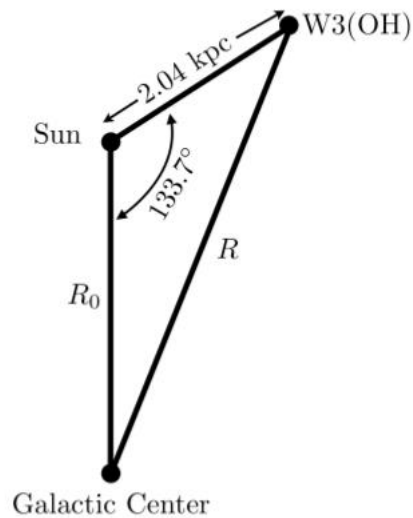


FIGURE C.3: Figure showing the location of W3(OH) within the galaxy. The galactic longitude of W3(OH) is  $l = 133.7^\circ$ , it lies further away from the galactic center than the sun, and therefore has a longer orbital period, and a smaller angular velocity than the sun. Figure courtesy of Weiler et al.(2009).

$$V = \omega R V_o = \omega_o R_o \quad (\text{C.4})$$

and substituting into equation (C.3)

$$v_{lsr} = \omega R_o \sin l - \omega_o R_o \sin l = (\omega - \omega_o) R_o \sin l \quad (\text{C.5})$$

we arrive at a relation between radial velocity, the angular velocity of an object in our galaxy as well as our Sun, and the distance from the galactic center to the Sun.

W3(OH) is observed at a longitude of  $l = 133.7^\circ$ , and is farther away from the galactic center than the Sun ( $\omega < \omega_o$ ). Therefore,

$$v_{lsr} = (\omega - \omega_o) R_o \sin(133.7^\circ) < 0. \quad (\text{C.6})$$

And so the line of sight velocity of W3(OH) is negative, and so, along the line of sight, appears to be moving toward us. This is known as a blueshift. This prediction is confirmed by observations of molecular lines which put the line of

sight velocity of W3(OH) at  $-49.1 \text{ km s}^{-1}$ , also known as the systemic velocity of the molecular cloud.

For the H<sub>2</sub>O masers observed in W3(OH), velocities greater than the systemic velocity are considered to be red shifted (moving away from the sun along the line of sight), while masers with velocities less than the systemic velocity of W3(OH) are considered to be blue shifted (moving toward the sun along the line of sight).

# Appendix D

## BS198A IVD Plots

Appendix D contains plots of the Stokes I and V profiles, along with the derivative of I scaled by the fitted value of  $B_{los}$  for all masers found during observation BS198A which showed Zeeman detection. The list of Zeeman detections for BS198A is given in Table (3.3).

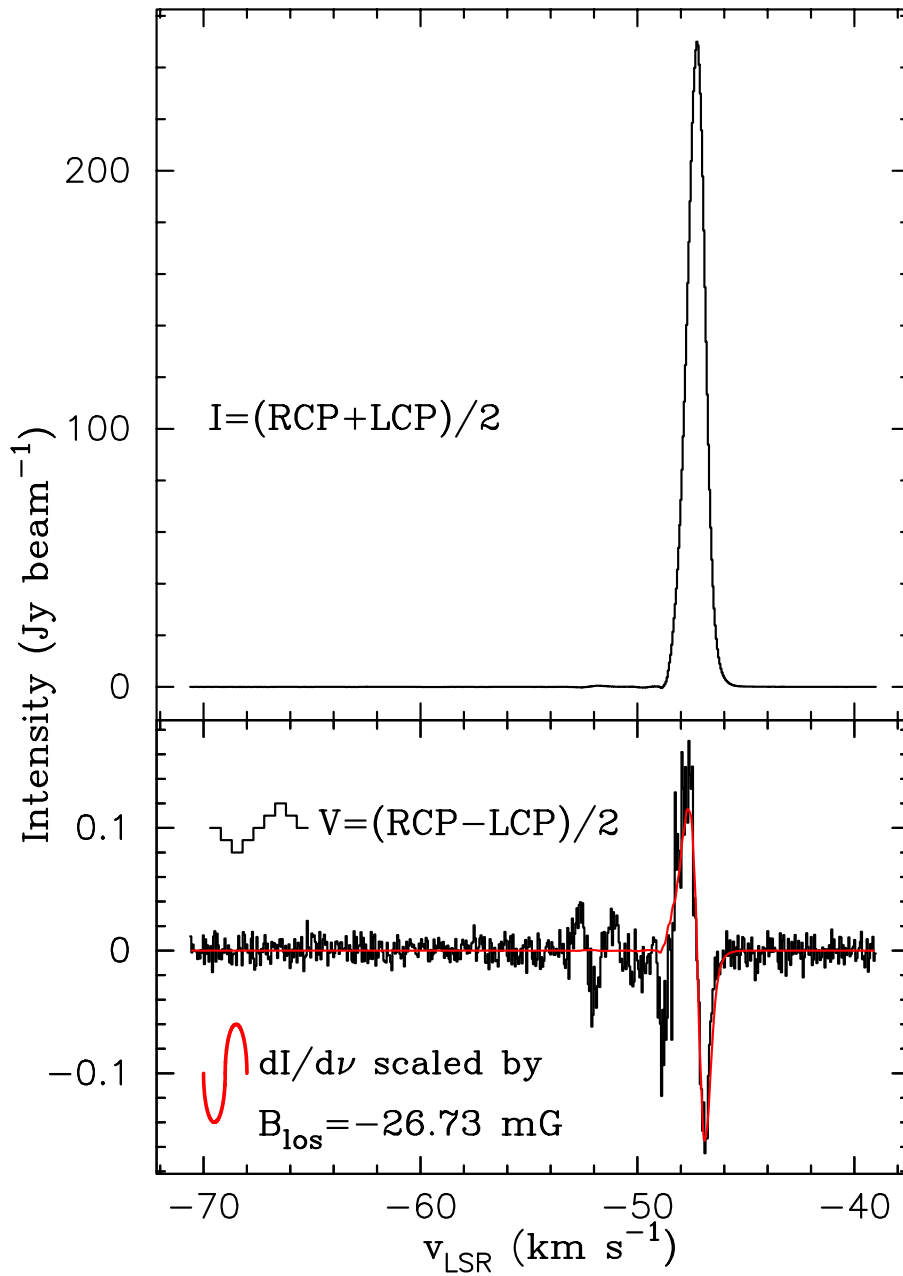


FIGURE D.1: Stokes I (top) and V (bottom) profiles of maser 2 from observation BS198A (as numbered in Table 3.1). The curve superposed on V in the lower frame is the derivative of I scaled by the fitted value of  $B_{\text{los}}$  given in Table (3.3)

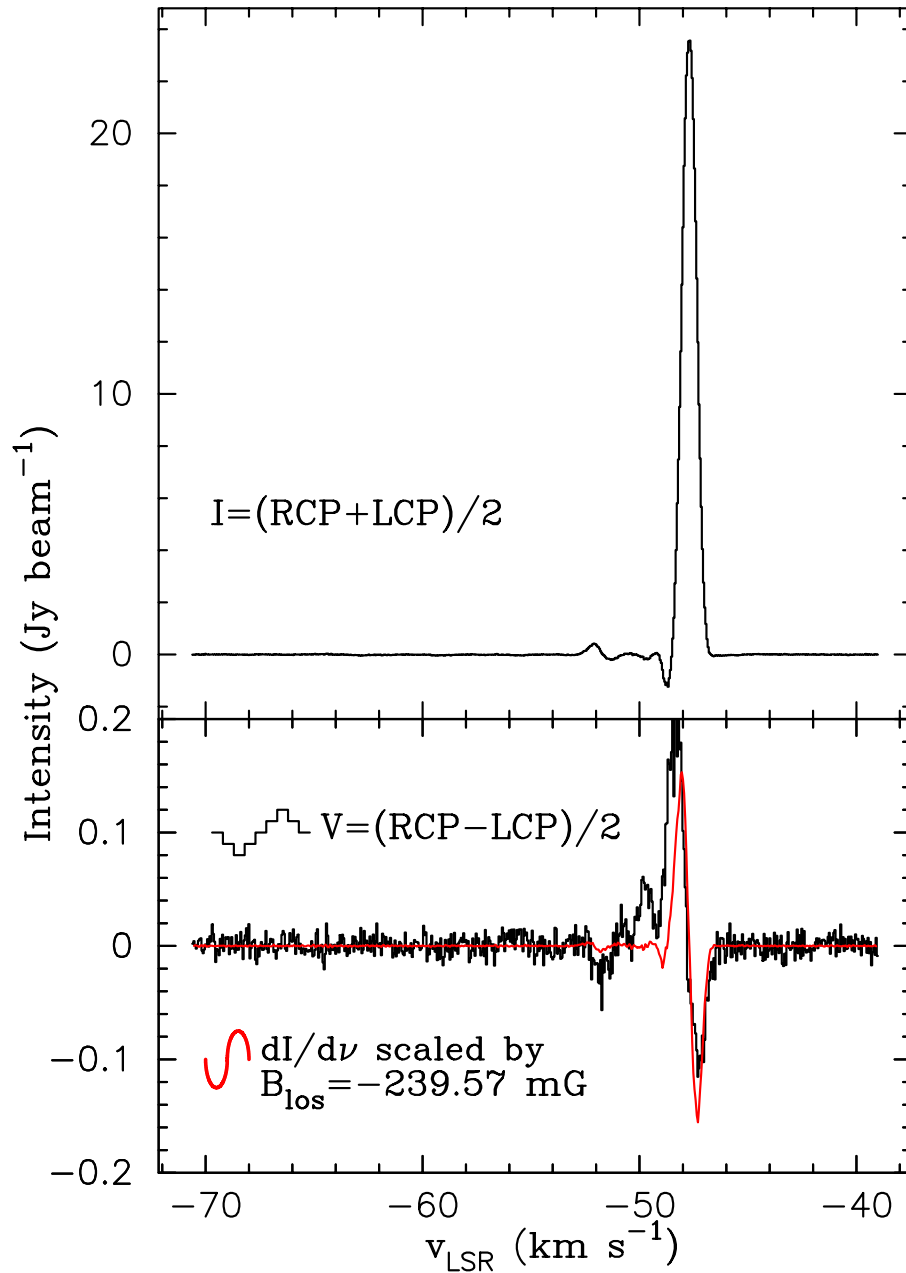


FIGURE D.2: Stokes I (top) and V (bottom) profiles of maser 13 from observation BS198A (as numbered in Table 3.1). The curve superposed on V in the lower frame is the derivative of I scaled by the fitted value of  $B_{\text{los}}$  given in Table (3.3)

# Appendix E

## BS198B IVD Plots

Appendix D contains plots of the Stokes I and V profiles, along with the derivative of I scaled by the fitted value of  $B_{los}$  for all masers found during observation BS198B which showed Zeeman detection. The list of Zeeman detections for BS198B is given in Table (3.3).

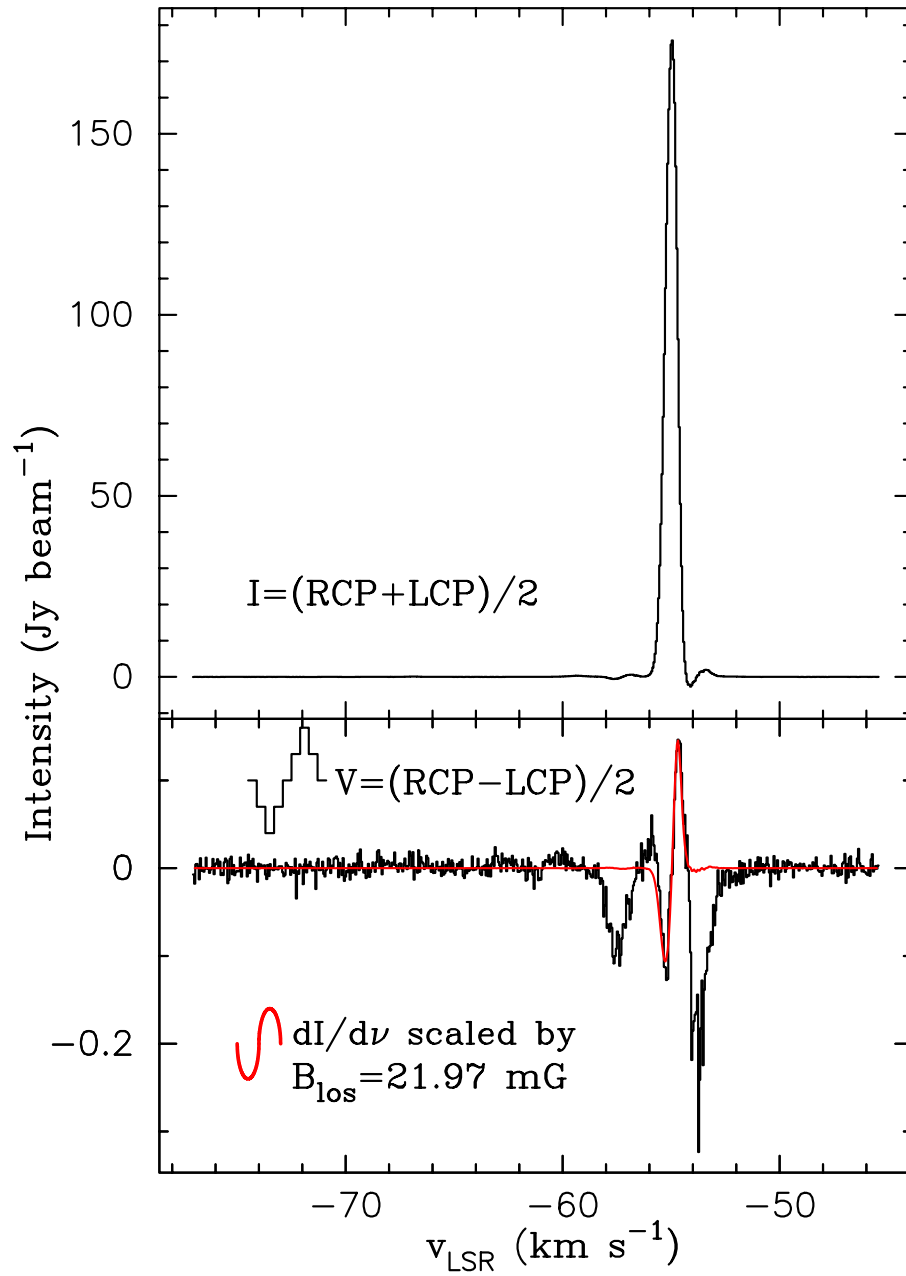


FIGURE E.1: Stokes I (top) and V (bottom) profiles of maser 4 from observation BS198B (as numbered in Table 3.2). The curve superposed on V in the lower frame is the derivative of I scaled by the fitted value of  $B_{\text{los}}$  given in Table (3.3)

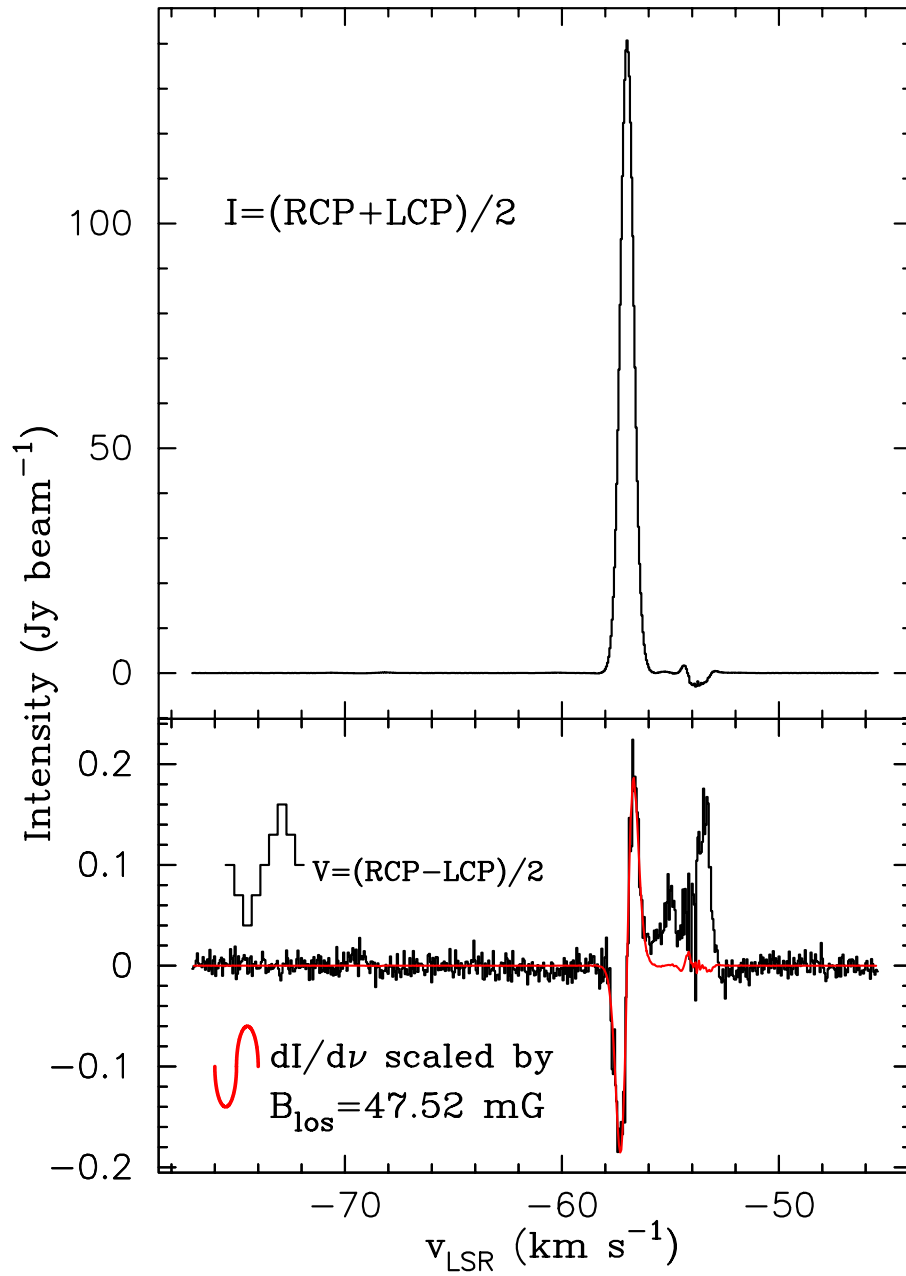


FIGURE E.2: Stokes I (top) and V (bottom) profiles of maser 5 from observation BS198B (as numbered in Table 3.2). The curve superposed on V in the lower frame is the derivative of I scaled by the fitted value of  $B_{\text{los}}$  given in Table (3.3)

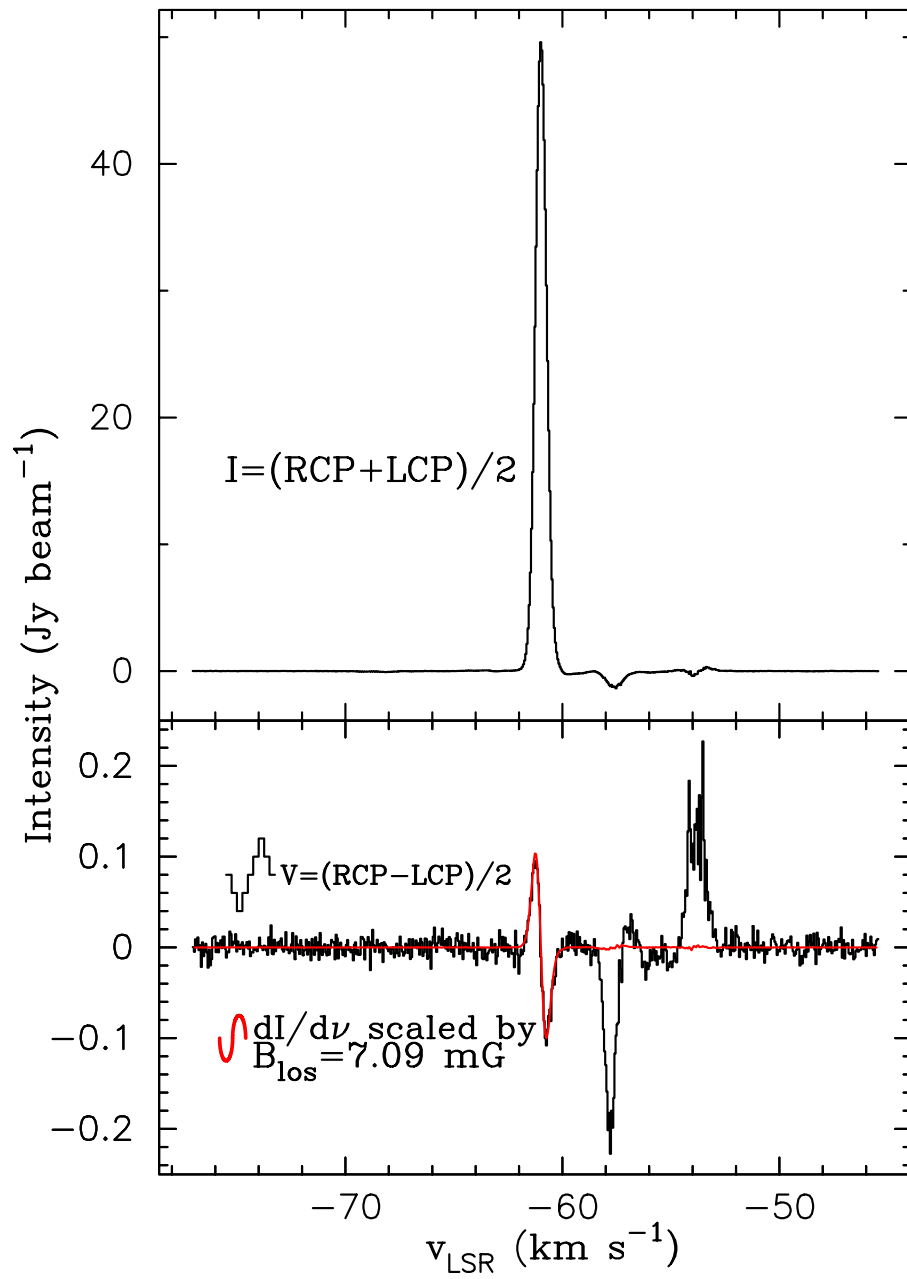


FIGURE E.3: Stokes I (top) and V (bottom) profiles of maser 9 from observation BS198B (as numbered in Table 3.2). The curve superposed on V in the lower frame is the derivative of I scaled by the fitted value of  $B_{\text{los}}$  given in Table (3.3)

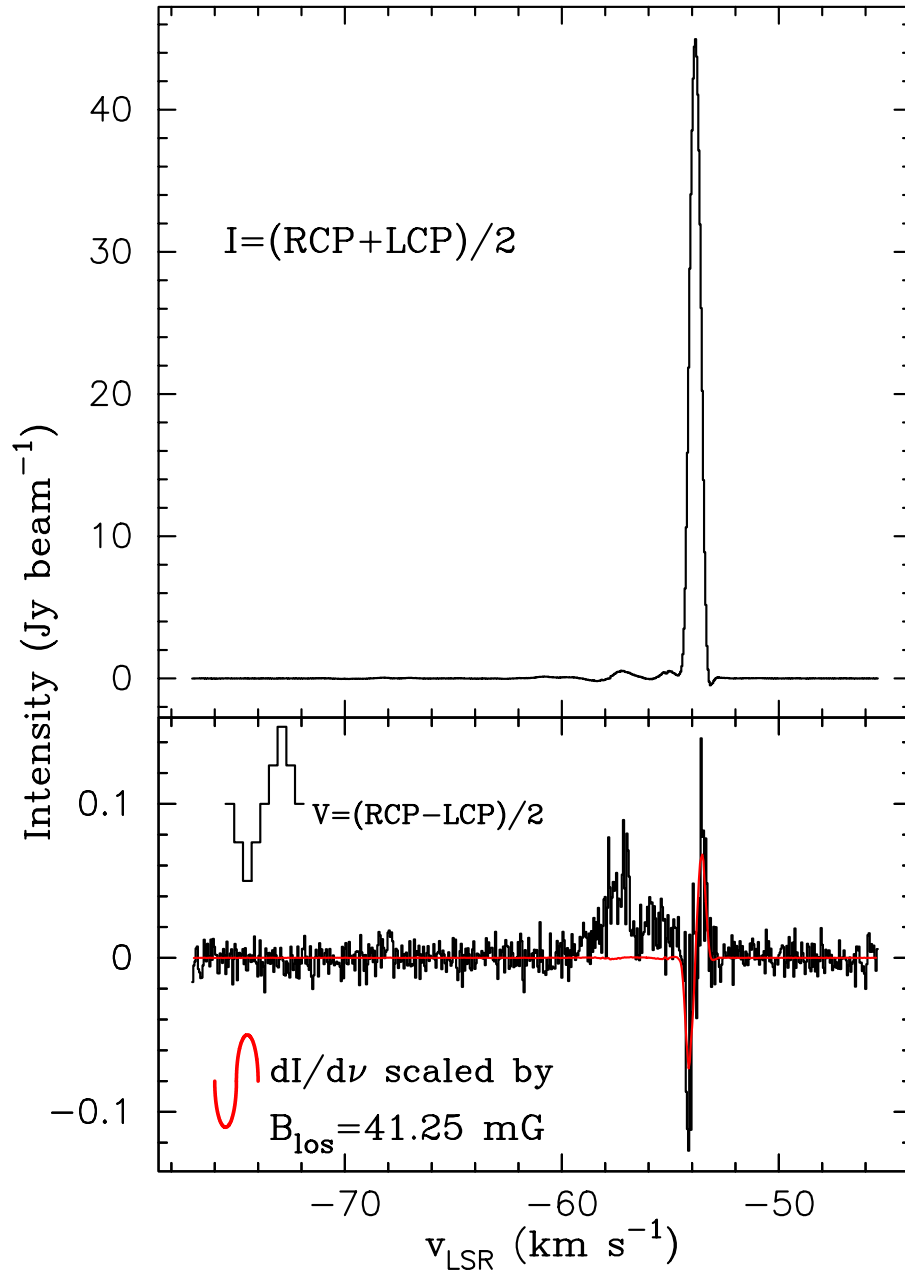


FIGURE E.4: Stokes I (top) and V (bottom) profiles of maser 10 from observation BS198B (as numbered in Table 3.2). The curve superposed on V in the lower frame is the derivative of I scaled by the fitted value of  $B_{\text{los}}$  given in Table (3.3)

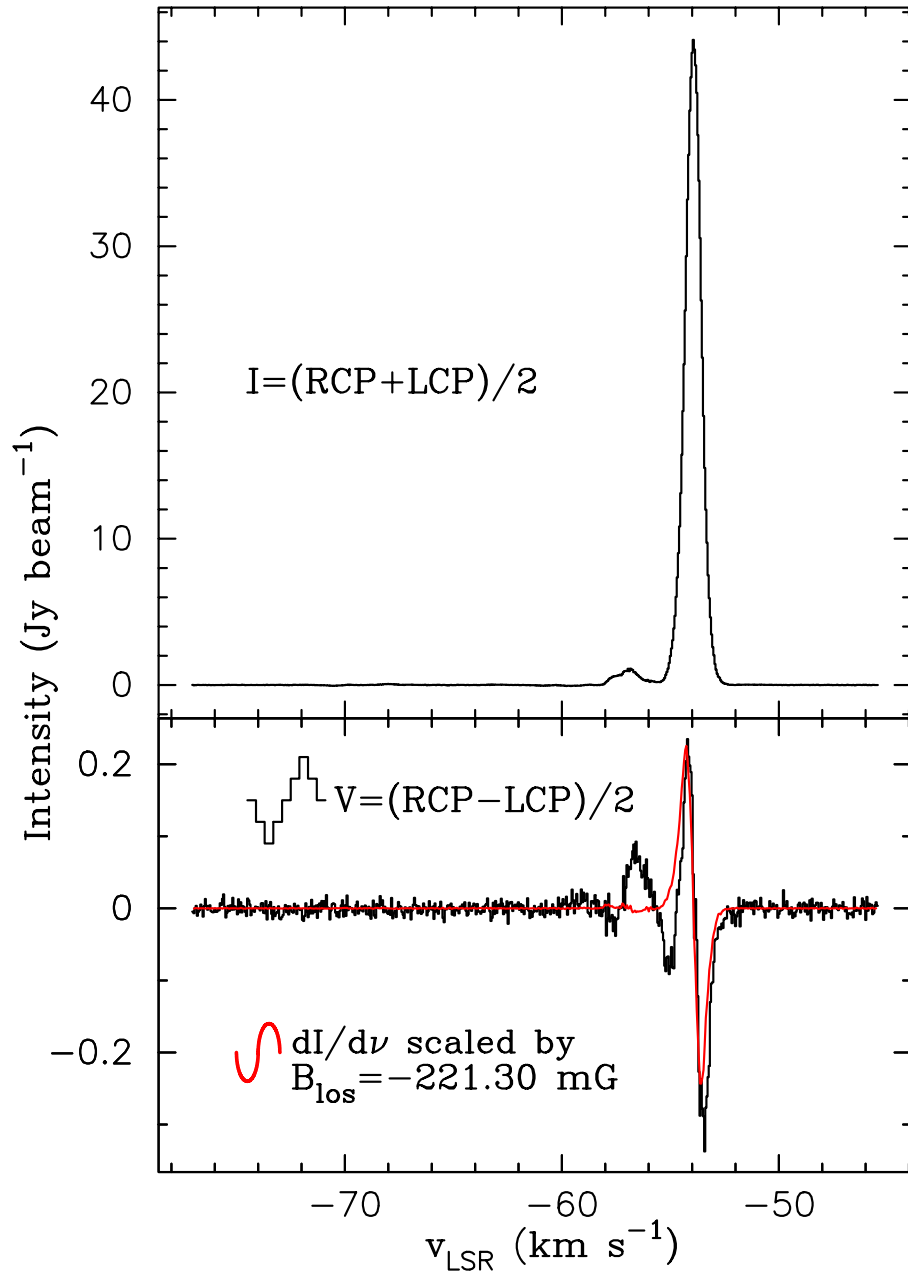


FIGURE E.5: Stokes I (top) and V (bottom) profiles of maser 11 from observation BS198B (as numbered in Table 3.2). The curve superposed on V in the lower frame is the derivative of I scaled by the fitted value of  $B_{\text{los}}$  given in Table (3.3)

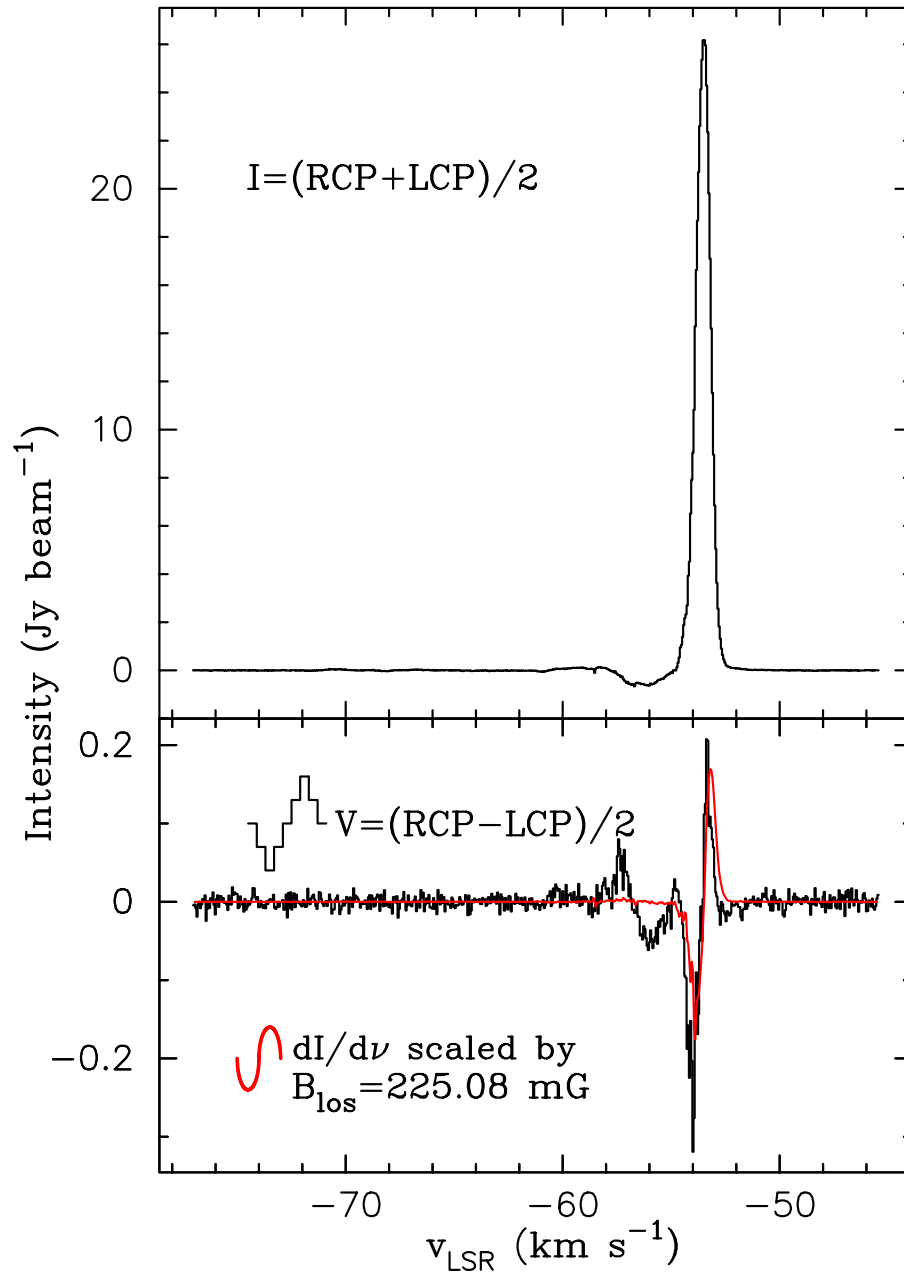


FIGURE E.6: Stokes I (top) and V (bottom) profiles of maser 15 from observation BS198B (as numbered in Table 3.2). The curve superposed on V in the lower frame is the derivative of I scaled by the fitted value of  $B_{\text{los}}$  given in Table (3.3)

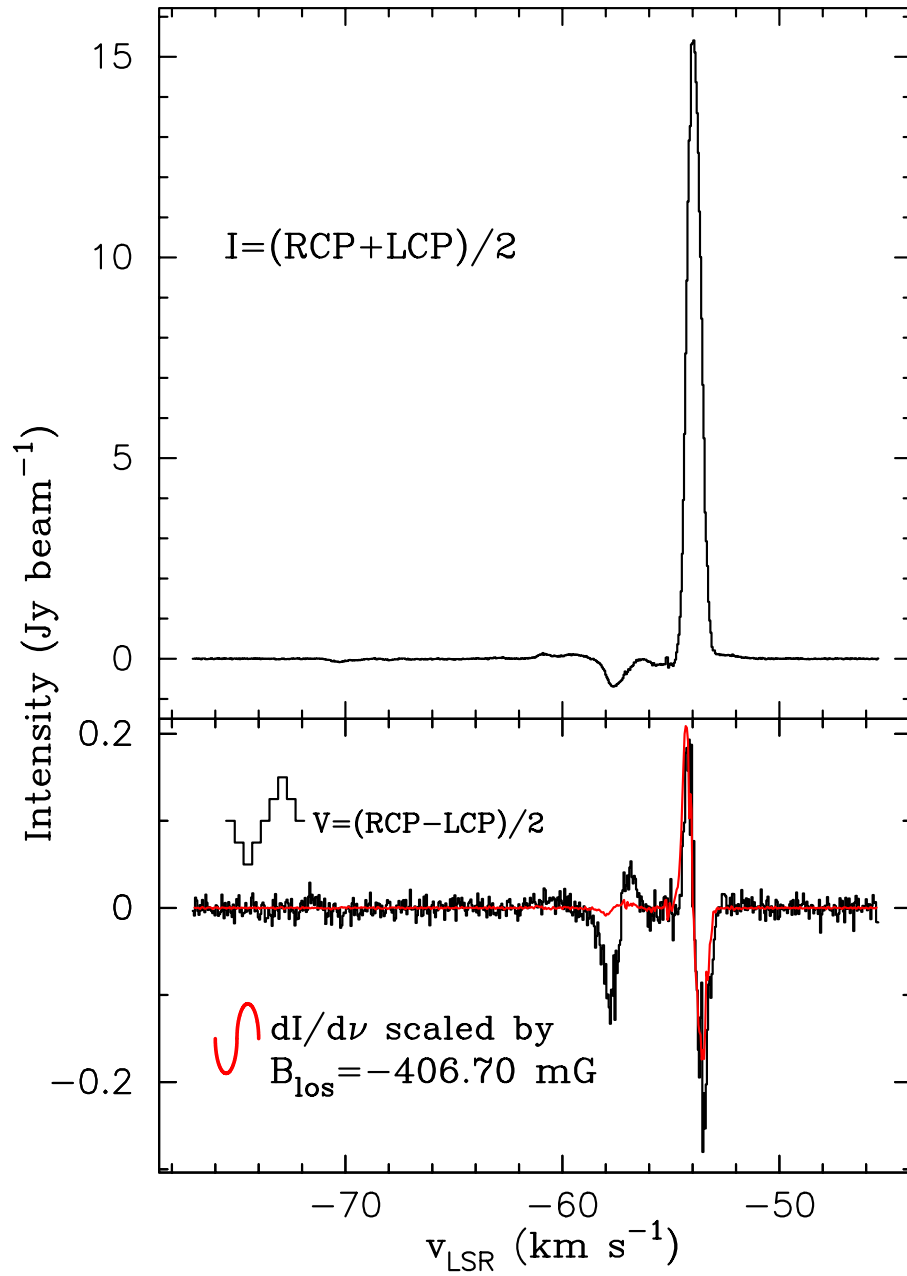


FIGURE E.7: Stokes I (top) and V (bottom) profiles of maser 25 from observation BS198B (as numbered in Table 3.2). The curve superposed on V in the lower frame is the derivative of I scaled by the fitted value of  $B_{\text{los}}$  given in Table (3.3)

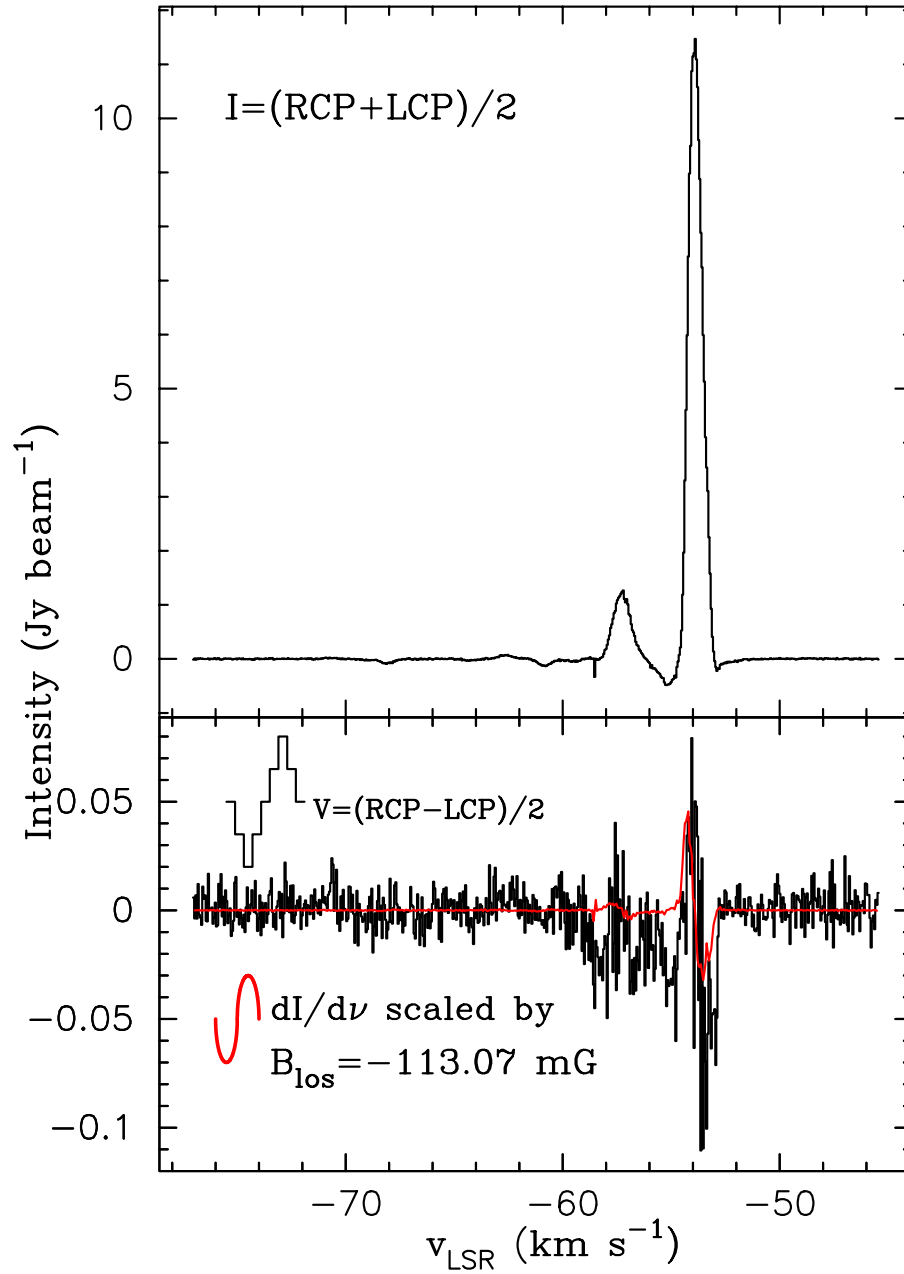


FIGURE E.8: Stokes I (top) and V (bottom) profiles of maser 33 from observation BS198B (as numbered in Table 3.2). The curve superposed on V in the lower frame is the derivative of I scaled by the fitted value of  $B_{\text{los}}$  given in Table (3.3)

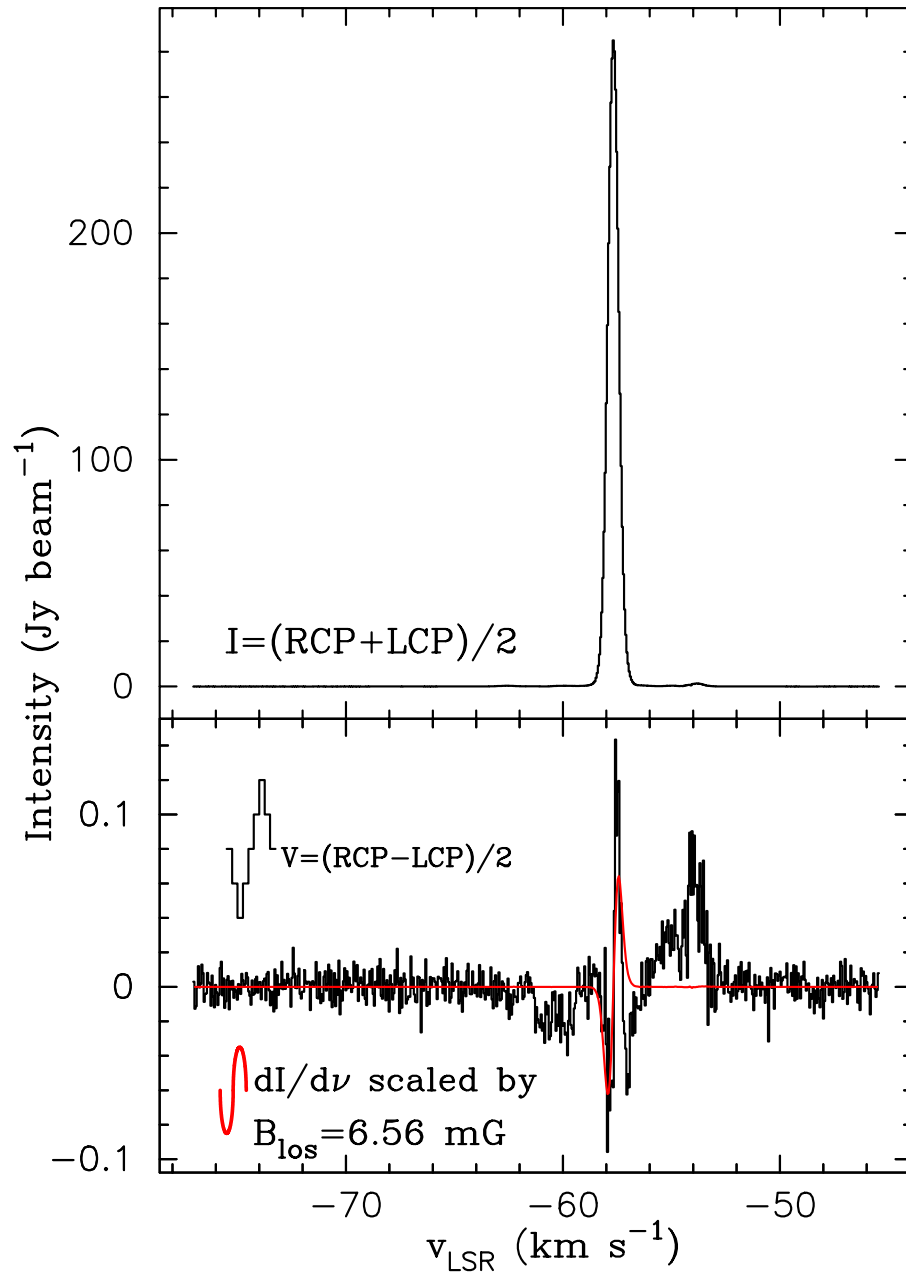


FIGURE E.9: Stokes I (top) and V (bottom) profiles of maser 43 from observation BS198B (as numbered in Table 3.2). The curve superposed on V in the lower frame is the derivative of I scaled by the fitted value of  $B_{los}$  given in Table (3.3)

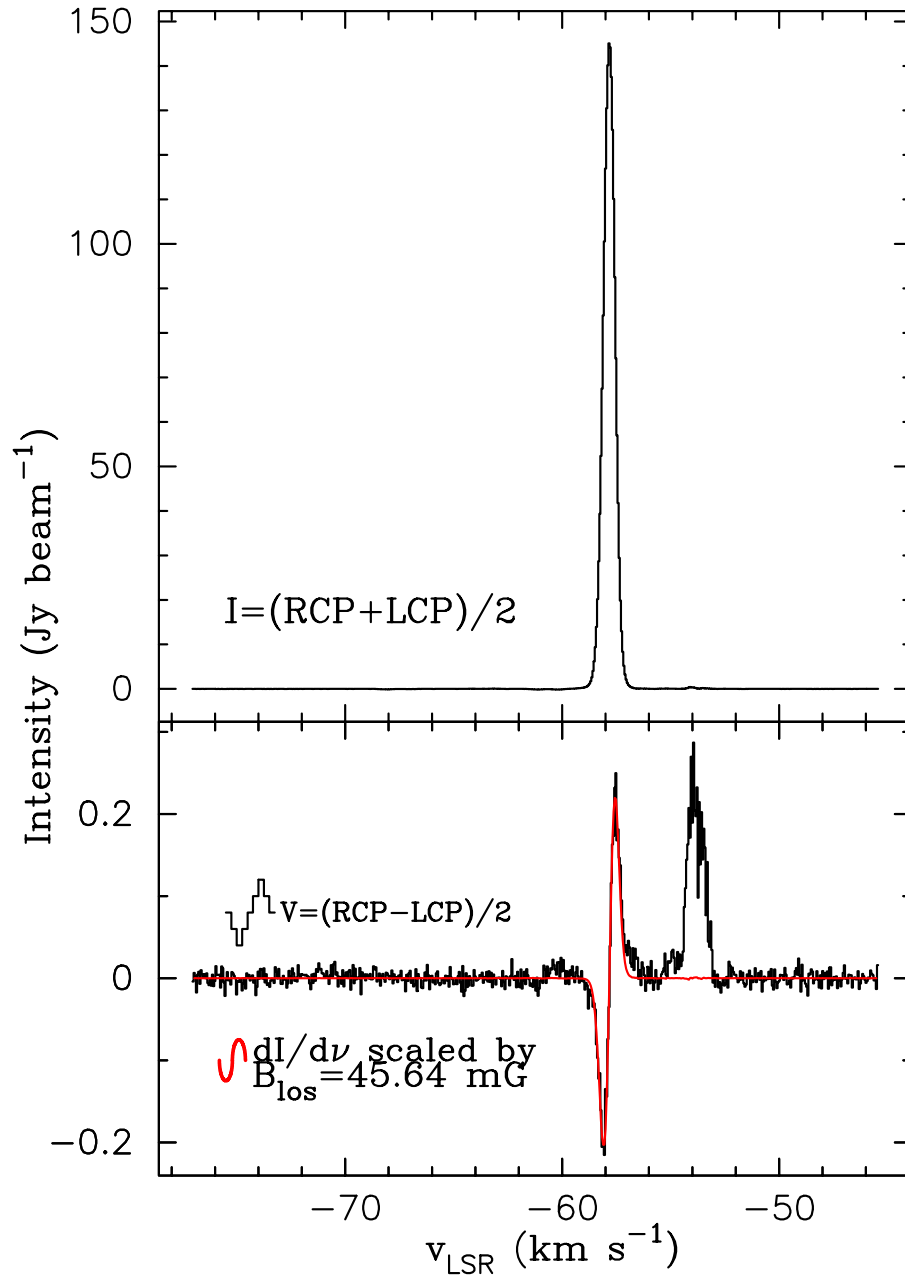


FIGURE E.10: Stokes I (top) and V (bottom) profiles of maser 44 from observation BS198B (as numbered in Table 3.2). The curve superposed on V in the lower frame is the derivative of I scaled by the fitted value of  $B_{\text{los}}$  given in Table (3.3)

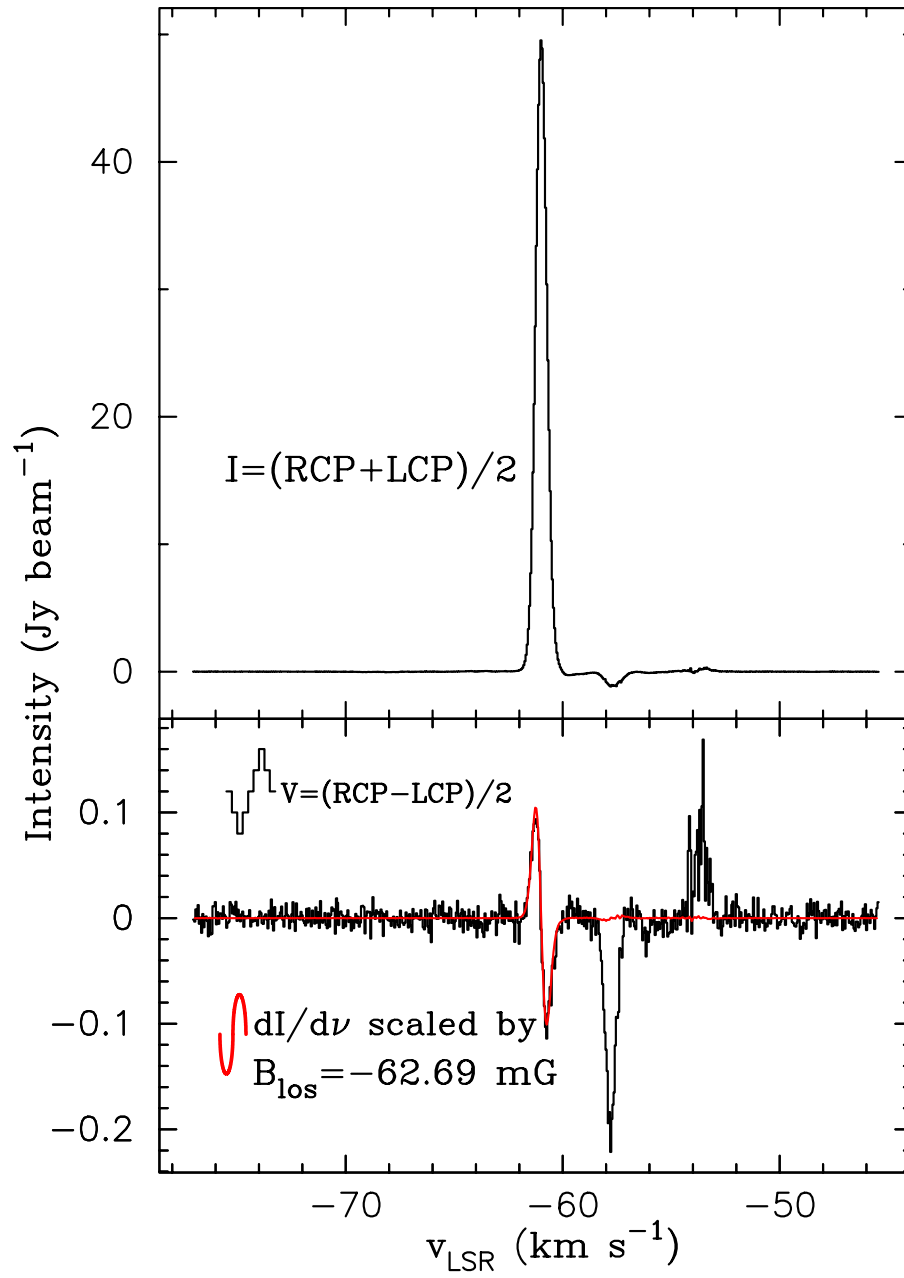


FIGURE E.11: Stokes I (top) and V (bottom) profiles of maser 45 from observation BS198B (as numbered in Table 3.2). The curve superposed on V in the lower frame is the derivative of I scaled by the fitted value of  $B_{\text{los}}$  given in Table (3.3)

# Bibliography

- [1] H. Beuther, E.B. Churchwell, C.F. McKee, and J.C. Tan. The formation of massive stars. *arXiv:astro-ph/0602012v2*, 2:1–15, February 2006.
- [2] H.R. Chen, R. Rao, D.J. Wilner, and S.Y. Liu. The magnetized environment of the w3(h<sub>2</sub>o) protostars. *arXiv:1204.3849v1*, 1:1–16, April 2012.
- [3] B.G. Clark. Synthesis imaging in radio astronomy ii. June 1999.
- [4] M. Clausen. Advanced calibration techniques. *NRAO 12<sup>th</sup> Synthesis Imaging Workshop Presentation*, June 2010.
- [5] B. Cooke and M. Elitzur. Water masers in late type stars. *The Astrophysical Journal*, 295:175–182, August 1985.
- [6] R.M. Crutcher. Magnetic fields in molecular clouds: Observations confront theory. *The Astrophysical Journal*, 520:706–713, August 1991.
- [7] M. Elitzur. Astronomical masers. *Kluwer Academic Publishers*, ISBN 0-7923-1216-3 (HB):48–49,221–222,262–278, 1992.
- [8] D. Fiebig and R. Güsten. Strong magnetic fields in interstellar h<sub>2</sub>o maser clumps. *Astronomy & Astrophysics*, 214:333–338, 1989.
- [9] G.Y. Golubiatnikov, V.N. Markov, A. Guarnieri, and R. Knöchel. Hyperfine structure of h<sub>2</sub><sup>16</sup>o and h<sub>2</sub><sup>18</sup>o measured by lamb-dip technique in the 180-560 ghz frequency range. *The Journal of Molecular Spectroscopy*, 240:251–254, September 2006.
- [10] E. Greisen. The aips cookbook. *NRAO*, December 2011.
- [11] R. Güsten, D. Fiebig, and K.I. Uchida. The magnetic field of a dense gas bordering w3(oh). *Astronomy & Astrophysics*, 286:L51–L54, April 1994.

- [12] K. Hachisuka, A. Brunthaler, K.M.Menten, M.J.Reid, H.Imai, Y.Hagiwara, M.Miyoshi, S.Horiuchi, and T.Sasao. The magnetic field of a dense gas bordering w3(oh). *The Astrophysical Journal*, 645:337–344, July 2006.
- [13] N.S. Hakobian and R.M. Crutcher. Structure and composition of molecular clouds with cn zeeman detections i: W3(oh). *arXiv:1103.3082v1*, pages 1–33, March 2011.
- [14] L. Harvey-Smith. Astrophysical masers. *Institute of Astronomy, University of Sydney*, Presentation, April 2008. URL <http://www.physics.usyd.edu.au/pdfs/current/tsp/tsp2008/LisaHarveySmith.pdf>.
- [15] J.A. Högbom. Aperature synthesis with a non-regular distribution of interferometer baselines. *Astronomy & Astrophysics Suppl.*, 15:417–426, 1974.
- [16] J. Holzman. Vlba observations of the high mass star forming region 22506+5944. *Depaul University Master's Thesis*, 2008.
- [17] K.M. Menton. Masers as chemical probes of star-forming rigions. *Molecules in Astrophysics: Probes and Processes*, pages 163–172, 1997.
- [18] L. Moscadelli, L. Testi, R.S. Furuya, C. Goddi, M. Claussen, Y. Kitamura, and A. Wootten. First results from a vlba proper motion survey of h<sub>2</sub>o masers in low mass yso's: the serpens core and rno 15-fir. *Astronomy & Astrophysics*, 446:985–999, June 2006.
- [19] G.E. Nedoluha and W.D. Watson. The zeeman effect in astrophysical water masers and the observation of strong magnetic fields in regions of star formation. *The Astrophysical Journal*, 384:185–196, January 1992.
- [20] The NRAO Website. What is aips? <http://www.aips.nrao.edu/whatisaips.html>, 1:1, 02 2012. URL <http://www.aips.nrao.edu/whatisaips.html>.
- [21] P. Padoan and A. Nordlund. The stellar initial mass function from turbulent fragmentation. *The Astrophysical Journal*, 576:870–879, September 2002.
- [22] R. Perley. Fundamentals of radio interferometry i & ii. *NRAO 13<sup>th</sup> Synthesis Imaging Workshop Presentation*, 554, May 2012.

- [23] A.P. Sarma, T.H. Troland, and J.D. Romney. Very long baseline array observations of the zeeman effect in h<sub>2</sub>o masers in w3 irs 5. *The Astrophysical Journal*, 554:L217–L220, June 2001.
- [24] A.P. Sarma, T.H. Troland, R.M. Crutcher, and D.A. Roberts. Magnetic fields in shocked regions: Very large array observations of h<sub>2</sub>o masers. *The Astrophysical Journal*, 580:928–937, December 2002.
- [25] A.P. Sarma, T.H. Troland, J.D. Romney, and T.H. Huynh. Vlba observations of the zeeman effect in h<sub>2</sub>o masers in oh 43.8-0.1. *The Astrophysical Journal*, 674:295–303, February 2008.
- [26] A.P. Sarma and E.Momjian. Detection of the zeeman effect in the 36 ghz class i ch<sub>3</sub>oh maser line with the evla. *The Astrophysical Journal*, 705:L176–L179, February 2009.
- [27] S. Lizano F.H. Shu, F.C. Adams. Star formation in molecular clouds: Observation and theory. *Annual Revue Astronomy & Astrophysics*, 25:23–81, 1987.
- [28] T.H. Troland. Aperature synthesis studies of the magnetic field in star-forming regions. *The Physics and Chemistry of the Interstellar Medium*, pages 253–256, 1999.
- [29] B.E. Turner. Magnetic fields in shocked regions: Very large array observations of h<sub>2</sub>o masers. *The Royal Astronomical Society of Canada Journal*, 64(4):221–237, December 1970.
- [30] B.E Turner. Masers in space. *Astronomical Society of the Pacific*, pages 996–1021, June 1970.
- [31] J.L. Turner and W.J. Welch. Discovery of a young stellar object near the water masers in w3(oh). *The Astrophysical Journal*, 287:L81–L84, December 1984.
- [32] D.A. Varshalovich, A.V. Ivanchik, and N.S. Babkovskaya. The  $\lambda_o = 1.35\text{cm}$  h<sub>2</sub>o maser line: The hyperfine structure and profile asymmetry. *Astronomy Letters*, 32(1):29–38, 2006.
- [33] W.D. Watson and H.W. Wyld. The relationship between the circular polarization and the magnetic field for astrophysical masers with weak zeeman splitting. *The Astrophysical Journal*, 558:L55–L58, September 2001.

- 
- [34] K.P. Welier. Observations of magnetic fields via the zeeman effect in h<sub>2</sub>o masers in the star forming region w3(oh). *Depaul University Master's Thesis*, 2009.
- [35] F. Wyrowski, P. Hofner, P. Schilke, C.M. Walmsley, D.J. Wilner, and J.E. Wink. Millimeter interferometry towards the ultra-compact hii region w3(oh). *Astronomy & Astrophysics*, 320:L17–L20, February 1997.
- [36] Y. Xu, X.W. Zheng, F.J. Zhang, Z.Y. Yu, P. Han, E. Scalise Jr., and Y.J. Chen. Rapid time variations of water maser emission in w3(oh) and ngc 6334c. *Astronomy & Astrophysics*, 364:232–236, July 2000.
- [37] L.A. Zapata, C. Rodriguez-Garza, L.F. Rodriguez, J.M. Girart, and H.R. Chen. Disks and outflows in the massive protobinary system w3(oh)tw. *The Astrophysical Journal Letters*, 740:1–8, September 2011.
- [38] H. Zinnecker and H.W. Yorke. Toward understanding massive star formation. *Annual Review of Astronomy & Astrophysics*, 45:481–563, February 2007.